UNIVERSIDADE DE SANTIAGO DE COMPOSTELA

FACULTADE DE FÍSICA

DEPARTAMENTO DE FÍSICA DA MATERIA CONDENSADA

GRUPO DE FÍSICA NON LINEAL

Patterns on Active Media

under the Effect of

Periodical and Fluctuating Fields

Memoria presentada por Irene Sendiña Nadal para optar ao grao de Doutora en Ciencias Físicas pola Universidade de Santiago de Compostela.

Xullo, 2001
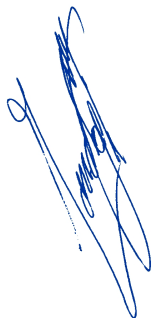
Moncho Gómez Gesteira e Vicente Pérez Muñuzuri, profesores titulares das Universidades de Vigo e Santiago de Compostela respectivamente,

CERTIFICAN

que a presente memoria, titulada *"Patterns on Active Media under the Effect of Periodical and Fluctuating Fields"*, foi realizada por **Irene Sendiña Nadal** baixo a súa dirección, e que conclúe a Tese que presenta para optar ao grao de Doutora en Ciencias Físicas.

E, para que así conste, firman a presente en Santiago de Compostela a 5 de Xullo de 2001.

V°. e prace
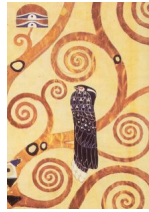Moncho Gómez Gesteira

V°. e prace
Vicente Pérez Muñuzuri

Irene Sendiña Nadal

A Jorge.
Á miña pequena grande familia.

Agradecementos
Agraïments
Agradecimientos
Acknowledgments

—Cuéntame un cuento —te digo.
—¿Cómo lo quieres?.
—Cuéntame un cuento que no le hayas contado a nadie.

Rolf Carle
en *Cuentos de Eva Luna* de Isabel Allende.

Contents

List of Figures

Resumo

Contexto do traballo

As fluctuacións espaciais e temporais permiten que os sistemas exploren novas rexións de estabilidade, presentes ou non no escenario determinista correspondiente. Son inherentes a calquera situación real e é natural que os seus efectos sobre a propagación e formación de estructuras fose tratada en multitude de artigos científicos nos últimos anos (consultar [1] and [2]).

Áreas de investigación completamente diferentes incluiron o ruido nos seus traballos analizando a influencia non trivial sobre sistemas espacialmente extendidos como os procesos bioquímicos na célula [3], transmisión de sinais en conxuntos de células [4], redes neuronais [5, 6], cadeas de circuitos electrónicos [7, 8], a meteoroloxía [9], reaccións químicas [10, 11]. Entre os fenómenos observados atópanse a rectificación na propagación inducida por ruido (recuperación de fallos de propagación), resonancia estocástica espacial, e dinámica de interfases e formación de estructuras inducidas por ruido.

No momento actual, o comportamento dinámico de sistemas excitables inhomoxéneos está a despertar moito interese. Redes neuronais ou o músculo cardíaco están entre os exemplos máis interesantes nas ciencias da vida. Resultados recentes [12] demostran que a estructura do miocardio está producindo constantemente inhomoxeneidades na concentración da carga eléctrica a nivel microscópico facendo estocástica a propagación no corazón. Isto implica que os eventos de excitación están continuamente cambiando e de forma desordenada durante a propagación eléctrica. A implicación máis importante disto é a posibilidade de formación de fluctuacións de maior intensidade e que se extendan a máis dunha célula. Cando isto sucede, a propagación das ondas eléctricas no corazón pode verse deteriorada pola presencia destas irregularidades e dar lugar a procesos de fibrilación e outras patoloxías do corazón. Por outra banda, tamén se cre

que o ruido xoga un papel fundamental no inicio e propagación das ondas no tecido neuronal [4, 5], onde a actividade de fondo aleatoria da rede depende da concentración dos neurotransmisores.

Un sistema experimental paradigmático dentro dos sistemas inertes que está sendo utilizado para estudiar o efecto de modulacións espaciotemporais na dinámica de estructuras é a ben coñecida reacción de Belousov-Zhabotinsky (BZ) co rutenio como catalizador [13]. Esta reacción é sensible á luz polo que a súa cinética pode ser controlada localmente proxectando distribucións específicas de luz. Neste contexto, estudios recentes utilizaron esta versión fotosensible da reacción de BZ para investigar a propagación de frentes de onda e a súa xeración en medios subexcitable desordenados espacialmente [11, 10]. Dentro deste marco de traballo, pódese esperar fenómenos interesantes na dinámica de propagación e formación de estructuras na presencia de ruido espaciotemporal.

Escenarios estocásticos diferentes son creados por fontes de ruido diferentes que están forzando un sistema espacialmente extendido. Para modelizar estas situacións, un ten que analizar as propiedades estadísticas das fluctuacións que actúan sobre o sistema e ver que tipo de fluctuación domina. Cando a aleatoriedade é controlada dende o exterior un pode introducir diferentes clases de fluctuacións e estudiar os seus efectos. Frentes propagándose en medios desordenados, liñas de lume en gases turbulentos e procesos de crecemento por medio da deposición aleatoria de partículas nun substrato son modelizados mediante ruidos tipo "quenched" (tamén chamados estáticos ou conxelados), porque a frente de onda pasa sobre as fluctuacións máis rapidamente que o tempo característico de evolución das fluctuacións [14, 15]. Esta situación estúdiase nesta tese utilizando frentes chímicos na reacción de BZ. A través dunha distribución espacial aleatoria da excitabilidade, a velocidade dunha frente inicialmente plana ven caracterizada por unha lei de potencias na amplitude do ruido de $\frac{2}{3}$. Outro comportamento crítico como son os fenómenos de percolación, pódense dar en frentes químicos utilizando a mesma configuración espacial desordenada pero permitindo que varíe a proporción p de sitios excitables ao longo da rede e asignando un valor non excitable ao resto dos sitios non ocupados.

Situacións nas cales o ruido varía tanto espacial como temporalmente tamén foron consideradas. Con respecto á dependencia espacial, as fluctuacións foron de tipo estructurado, é dicir, de tipo triangular e sen correlación espacial. A dependencia temporal foi escollida tanto de correlación blanca (descorrelacionada) e coloreada de frecuencia finita.
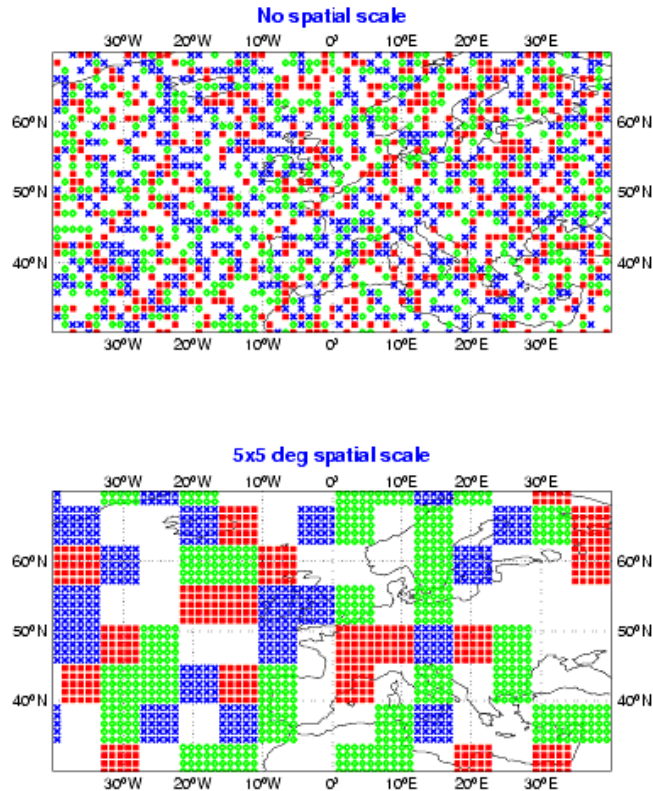
Figura 1: Random numbers used to perturb the tendencies due to parameterised physical processes. The top panel shows the case of no spatial scale, in other words when different random numbers are used at each grid-point. The bottom panel shows the case when the same random number was used for grid-points inside 5-degree boxes. The colors indicate random numbers distributed in three different intervals. Results indicated that even perturbations without any spatial structure had a major impact on 10-day model integrations. From [9].

A utilización de ruidos espacialmente estructurados e temporalmente correlacionados está xustificada cando o sistema posúe escalas espaciais e temporais características. Unha aplicación sorprendente é o uso recente de fluctuacións espaciotemporais na predicción do tempo por conxuntos introducindo un simple esquema estocástico para simular os erros aleatorios no modelo de predicción debido ás parametrizacións dos procesos físicos [9]. A contribución ás ecuacións do modelo meteorolóxico dos procesos físicos que son parametrizados, pertúrbase engadindo números aleatorios uniformes proporcionalmente á contribución parametrizada. Despois de

moitos ensaios, atoparon que a lonxitude de correlación óptima era de 10 graos e o tempo de correlación óptimo de 6 horas, mellorando a predicción meteorolóxica a moitos días.

Polo tanto, ruidos correlacionados con correlación temporal e/ou espacial, poden chegar a ser relevantes en sistemas que presentan escalas de tempo e espacio características. Nesta tese investigouse o efecto da correlación espacial e temporal tanto en trens de onda nun medio non excitable como en ondas espirais en condicións excitables. Cada unha destas estructuras posúe unha escala de tempo propia, a saber, o periodo do tren e a frecuencia de rotación respectivamente. Con respecto á correlación espacial do ruido, atopouse que é crítica cando é maior ou da orde do ancho da frente de onda ou do tamaño do centro da espiral. Para valores máis pequenos que estas lonxitudes típicas, non teñen lugar fenómenos interesantes probablemente debido a un promedio espacial do ruido que fai que o medio apareza efectivamente homoxéneo. Os resultados de forzar o sistema con este tipo de fluctuacións son unha mellora na propagación do tren no sentido de que avanza máis lonxe cando as correlacións espacial e temporal son próximas ás escalas espacial e temporal do tren, e un movemento tipo Browniano da espiral caracterizado por un coeficiente de difusión que depende non linealmente do tempo de correlación.

O caso oposto ao anterior, é ruido totalmente descorrelacionado, tanto espacial como temporalmente, normalmente identificado con fluctuacións térmicas. Especificamente, consideramos o papel deste tipo de fluctuacións na dinámica de formación de estructuras. Varios sistemas que presentan estructuras son susceptibles de sufrir transicións a un estado ordenado cando son sometidos a fluctuacións espaciotemporais como o caso da convección de Rayleigh-Bénard. O ruido pode inducir un desplazamento na transición dende un estado de conducción (sen estructuras) a un estado convectivo no que aparecerían as típicas estructuras de convección que non existirían sen a presencia desas fluctuacións. O noso obxectivo foi estudiar este mesmo escenario na reacción de BZ. Cando a luz fluctúa temporal e espacialmente ao redor dun valor medio próximo á transición excitable/oscilante na reacción de BZ, ondas circulares inducidas polo ruido son mantidas periodicamente nun medio efectivo excitable. A pesar de que o sistema en promedio localmente está por debaixo do umbral de formación autónoma de estructuras, as fluctuacións excitan a periodicidade subxacente no sistema. Ademáis, este resultado experimental de creación de ondas circulares por ruido comparte un marco teórico común con outro experimento recente de ondas que se propagan nun medio subexcitable

mantidas polo ruido.

E indo cara escenarios determinísticos, sistemas extensos forzados periodicamente tamén presentan un grande número de fenómenos de estructuras [16, 17], relacionados con resonancias de sistemas oscilantes a estímulos periódicos. Nesta tese adícase un capítulo ao estudio de forzamentos periódicos homoxéneos espacialmente, pois deron lugar a comportamentos interesantes como cuasiperiodicidade e propagación mantida en medios subexcitables. As modulacións son introducidas a través de fronteiras sinusoidalmente onduladas no primeiro caso, e mediante variacións periódicas na intensidade da luz en torno a un estado de referencia subexcitable no outro.

Esta tese pretende contribuir a aumentar o coñecemento actual sobre propagación de ondas, formación de estructuras e dinámica de ondas espirais en medios excitables extensos sometidos a fluctuacións espaciotemporais usando como ferramenta experimental a reacción fotosensible de BZ na maior parte dos casos estudiados. Simulacións numéricas foron realizadas en paralelo co modelo Oregonator e sempre que foi posible fíxose unha interpretación analítica do proceso.

Resumo da memoria

No Capítulo 1 dáse unha breve introducción ao mundo dos medios activos extensos en termos da ampla clase de sistemas de reacción-difusión. Os diferentes réximes de estabilidade e procesos de formación de estructuras explícanse nunha e dúas dimensións ao longo deste capítulo.

No Capítulo 2 preséntase a montaxe experimental, coa reacción de Belousov-Zhabotinsky fotosensible como parte principal, e o modelo Oregonator derivado das ecuacións de balance propostas ata o momento, o cal foi utilizado para realizar a simulación numérica dos experimentos. A construcción e caracterización dos diferentes patróns de iluminación usados para perturbar a reacción son explicados neste capítulo, así como o esquema de integración numérico do modelo Oregonator e os algoritmos utilizados para simular os procesos estocásticos.

A parte determinística desta tese é o Capítulo 3 onde os efectos de simples modulacións periódicas espacialmente homoxéneas son investigados en dous escenarios diferentes. No primeiro, desenvolvido na Sección 3.2, as modulacións periódicas son introducidas a través das fronteiras no modelo numérico. Un tren de ondas é forzado a propagarse ao longo dun canal de paredes sinusoidais. A variación da frecuencia espacial así como a amplitude

da fronteira modulada produce configuracións espaciais cuasiperiódicas, inconmesurables coas fronteiras pero periódicas no tempo e sincronizadas co estímulo. Estas estructuras foron descritas en termos de mapas de retorno espaciais que son moi similares ao mapa do círculo onde, neste caso, a iteración do mapa describe a dinámica temporal de osciladores forzados. Por outra banda, a segunda situación de forzamento mostrada na Sección 3.3 considera modulacións periódicas da excitabilidade nun medio subexcitable, isto é, un medio incapaz de manter a propagación de frentes acotados. Dentro do espacio de fases dos parámetros de forzamento, hai unha rexión onde o carácter subexcitable é invertido e a propagación é posible. Esta parte fíxose tanto experimental como numericamente.

No Capítulo 4 elixíronse distribucións dicotómicas estáticas da intensidade de luz para forzar aleatoriamente a reacción de BZ de forma simple. Resultaron velocidades de propagación máis pequenas ou máis grandes que a correspondente a unha situación homoxénea dependendo da dimensionalidade do medio. Estudios analíticos e experimentos deron lugar a leis de potencia entre a velocidade relativa da frente no medio inhomoxéneo e a amplitude do ruido. Para distribucións dicotómicas especiais onde o número de sitios excitables era variable co resto de sitios vacíos, observáronse fenómenos de percolación que estaban caracterizados por umbrais críticos percolativos dunha rede cadrada bidimensional. Na derradeira sección deste capítulo, tamén se considera o efecto de fluctuacións na propagación de frentes pero esta vez variando no tempo. Estudiamos a propagación dun tren de frentes de onda unidimensional nun medio non excitable con ruido espaciotemporal correlacionado temporalmente. As tasas de propagación en número de frentes que acadan unha posición de control, dependeron tanto do periodo do tren de ondas como dos parámetros do ruido. Estudios previos a este mostraban que existía un tipo de resonancia estocástica relacionada coa intensidade do ruido que favorecía a propagación nun medio subexcitable. Aquí, obtivemos dende un punto de vista numérico, unha mellora global da propagación non só para unha intensidade óptima do ruido senón que tamén para un tempo e lonxitude de correlacións próximas ao tempo e lonxitude característicos da estructura periódica.

No Capítulo 5 considéranse os efectos dun ruido espacialmente estructurado e correlacionado temporalmente no movemento dunha espiral na reacción de BZ e no modelo Oregonator. O principal efecto nos dous sistemas é inducir un movemento Browniano na punta da espiral caracterizado por un coeficiente de difusión que presenta unha dependencia

complexa nas escalas temporal e espacial do ruido respecto ás da espiral. En particular, un efecto tipo resonancia aparece co tempo de correlación mantendo fixa a intensidade de ruido. Un modelo cinemático foi proposto para interpretar este movemento obténdose un acordo bastante bo entre teoría, experimentos e cálculo numérico.

No Capítulo 6, un marcapasos que emite regularmente ondas, surxe do ruido cando a reacción de BZ en réxime excitable, que estrictamente é incapaz de crear ondas de forma autónoma, é forzada cun campo de luz aleatorio descorrelacionado espacial e temporalmente. Estas observacións experimentais foron tamén reproducidas numéricamente, e interpretado analiticamente en termos de efectos de acoplamento xenuinos que saen das fluctuacións paramétricas. Dentro deste mesmo marco analítico tamén se poden explicar outras transicións como a propagación nun medio subexcitable cando é forzado con fluctuacións espaciotemporais blancas.

E finalmente, as principais conclusións desta tese están recollidas no Capítulo 7.

Summary

Context of the work

Spatiotemporal fluctuations allow systems to explore new regions around those present in the deterministic scenario. Noise is ubiquitous in any realistic situation and it is natural that its effects on wave front propagation had been addressed in many papers during the last years (see [1] and [2]).

Completely different research areas have included noise in their investigations analyzing the nontrivial influence of external fluctuations in spatially distributed systems such as biochemical processes in the cell [3], signaling in cellular assemblies [4], neuronal networks [5, 6], arrays of electronic circuits [7, 8], weather forecasts [9], chemical reactions [10, 11], etc. Among the observed phenomena are noise-induced rectified motion (remedy propagation failure), spatial stochastic resonance, noise induced interface dynamics, and noise-induced patterns.

At present, the dynamical behavior of inhomogeneous excitable media has aroused so much interest. Neuronal networks or cardiac muscle are among the most interesting examples in life sciences. Recent results [12] show that the myocardial structure is creating inhomogeneities of electrical load at the microscopic level that makes cardiac propagation to be stochastic. This means that excitation events are constantly changing and in a disordered manner during electrical propagation. The major implication of this is the possibility of formation of larger fluctuations of load extending to more than one cell. When this occurs, electrical waves may be disrupted by these irregularities giving rise to the onset of cardiac fibrillation and other pathological diseases. On the other hand, noise is thought to play a fundamental role in initiation and propagation of waves in neural tissue [4, 5], where background random activity of the network is controlled by the neurotransmitter concentrations.

A paradigmatic experimental non living system that has been used

to study the effect of spatiotemporal modulations on pattern dynamics is the well-known ruthenium-catalyzed Belousov- Zhabotinsky (BZ) reaction [13]. This reaction is light-sensitive and thus projection of patterns of illumination can be used to locally control its kinetics. In this context, recent studies have used the light-sensitive BZ reaction to investigate wave front propagation and generation in spatially disordered subexcitable media [11, 10]. Within this framework it may be expected interesting phenomena in the motion of wave fronts and pattern formation under the presence of spatiotemporal noise.

Different stochastic scenarios are created by completely different sources of noise which can be considered to drive a spatially extended system. In modeling such situations, one has to analyze the statistical properties of the fluctuations acting in the system and see which kind of fluctuation dominates. When the randomness is controlled from outside one can introduce different sort of fluctuations and study their effects on the system. Propagating fronts in disordered media, flames propagating through turbulent gases, and growth phenomena by means of the random deposition of particles on a substrate are modeled with quenched noises (frozen, or static noises), because the front sweeps through fluctuations faster than the characteristic time for the fluctuations to evolve [14, 15]. This situation is investigated in this thesis using chemical fronts in the BZ reaction. Through a static disordered spatial distribution of the excitability properties of the reaction, the velocity of an initially planar wave front is characterized as a $\frac{2}{3}$ power law of the disorder amplitude. Other critical behaviors such as percolation phenomena can arise using the same disordered spatial configuration but allowing to vary the proportion p of excitable sites through the lattice and assigning a nonexcitable value to the proportion $1 - p$.

Situations where noise varies both in time and space are also considered. With respect to the spatial dependence, fluctuations are of the structured type, that is, of the triangularlike form and decorrelated. Time dependence is taking to be both white of zero correlation time and colored of a finite frequency. The use of spatially structured and temporally correlated noise is justified when the system has some intrinsic space and time scales. A surprising application is the recent use of spatiotemporal noise in ensemble weather forecasting by introducing a simple stochastic scheme for simulating random model errors due to parameterized physical processes [9]. The contribution to the model equations of the weather of the parameterized physical processes are perturbed by adding uniform

random numbers proportionally to the parameterized contribution. After experimentation, they found an optimal correlation length of 10 degrees box size and an optimal correlation time of 6 hours time interval of consecutive updates, which improved large-range weather forecasts (see Fig. 1).

Thus correlated noises with temporal and/or spatial correlation, can be expected to be of relevance in systems exhibiting characteristic space and time scales. We have investigated the effect of spatial and time correlation both on a train of wave fronts in an unexcitable medium and on a spiral wave in excitable conditions. Each of these structures have a characteristic time scale, namely, the period of the train and the frequency of rotation respectively. Concerning the spatial correlation of the noise, it has been found to be critical when it is larger or of the order of the front width and of the core of the spiral wave. For shorter values than the typical lengths of these structures, no interesting phenomena occur probably due to a spatial average of the noise which makes the medium appears effectively homogeneous. The results of applying this type of spatiotemporal fluctuations are some kind of enhanced propagation when the spatial and temporal correlations meet the characteristic spatial/time scales of the wave train and a Brownian-like motion of the spiral wave characterized by a diffusion coefficient which depends nonlinearly of the correlation time.

The opposite case to the previous one, are noise totally uncorrelated, both in time and space, usually considered as thermal fluctuations. Specifically, we consider the role of spatiotemporal fluctuations on the dynamics of pattern formation. Several pattern-forming systems are susceptible to undergo a transition to an ordered state when subjected to spatiotemporal fluctuations as in the Rayleigh-Bénard convection. Noise may induce a shift in the transition from a conducting state (no pattern) to a convective state emerging the typical convective patterns which would no exist in the absence of noise. Our purpose was to study such scenario in the BZ reaction. When light fluctuates in time and space around an average value close to the transition from excitable to oscillatory behavior in the BZ dynamics, noise-induced targets are periodically sustained in the effective excitable medium. Even below the threshold for the autonomous onset of patterns, fluctuations excite the underlying periodicity of the system. Moreover, this experimental finding of created targets out of noise shares a common theoretical framework with another recent experiment of noise-supported waves in subexcitable media.

Going to deterministic scenarios, periodically forced extended systems

have also been investigated exhibiting a number of interesting pattern phenomena [16, 17] related to entrainment of oscillating systems to external periodic stimuli. In this thesis, a chapter is devoted to the study of spatially homogeneous periodical forcings, as they give rise to some interesting phenomena such as quasiperiodicity and sustained- propagation in subexcitable media. The modulations are introduced through sinusoidally varying boundaries in one situation, and by periodically varying in time the light intensity around a reference state of subexcitability in the other.

This thesis intends to contribute to the increase of the present knowledge on wave propagation, pattern formation and spiral wave dynamics in excitable extended media subjected to spatiotemporal fluctuations using as an experimental tool the photosensitive BZ reaction in most of the cases. Numerical simulations have been performed in parallel with the Oregonator model and whenever was possible an analytical interpretation was provided.

Summary of the thesis

In Chapter 1 a brief introduction to the world of extended active media is given in terms of the large class of reaction-diffusion systems. The different regimes of stability and the process of pattern formation in one and two dimensions are explained through out this chapter.

Chapter 2 is devoted to present our experimental setup, with the photosensitive Belousov-Zhabotinsky reaction as the leading part, and the Oregonator model derived from the known balance equations, which has been used to perform the numerical simulations. The construction and characterization of the different spatiotemporal random patterns of illumination used to perturb the reaction are explained, as well as the numerical scheme of integration of the Oregonator model and the algorithms to simulate stochastic processes.

The deterministic part of this thesis is treated in Chapter 3 where the effects of simple spatially homogeneous periodic modulations are investigated in two very different scenarios. In the first one, developed through Section 3.2, periodic modulations are introduced through the boundaries in the numerical model. A wave train is forced to propagate along a narrow excitable channel with its walls sinusoidally varying. The variation of the spatial frequency as well as the amplitude of the modulated boundary produce quasiperiodic spatial configurations, incommensurate with the boundaries but periodic in time and synchronized with the stimuli.

These structures were described in terms of spatial return maps that are very similar to the circle maps whose iteration describe the temporal dynamics of forced oscillators. This similarity allows one to speculate about the existence of even more complex configurations representing the spatial realizations of the chaotic regimes of these maps. On the other hand, the second situation shown in Section 3.3 deals with temporal periodical modulations of the excitability in a subexcitable medium, that is, a medium unable to sustain propagation of bounded fronts. In the forcing parameter phase space there is a region where the subexcitable character is inverted and propagation sustained. This was achieved both experimentally and numerically.

Quenched dichotomic distributions of the light intensity have been chosen for simplicity to randomly force the BZ reaction in Chapter 4. Larger or smaller speeds compared to the one corresponding to the equivalent homogeneous situation have been obtained depending on the dimensionality of the medium. Analytical studies and experiments give rise to power laws relations between the relative velocity of the front in the inhomogeneous medium and the noise amplitude. For special dichotomic distributions where the number of excitable sites was allowed to vary in the lattice with the rest of the sites representing empty sites, percolating phenomena was observed and characterized with the percolation thresholds of a two-dimensional square lattice. The last section of this chapter, also considers the effect of fluctuations in wave propagation but this time allowing them to vary in time. We study the propagation of a one dimensional train of wave fronts in the unexcitable regime under a time correlated spatiotemporal noise. Different rates of supported transmission dependent on the period of the wave train and on the parameters of the noise are found. Previous studies have found stochastic resonance related to the intensity of the noise giving rise to an improvement of the wave front propagation through a subexcitable medium. Here, we obtain from a numerical point of view, an overall enhancement of wave propagation not only for an optimal intensity of the noise but also for a correlation time that matches the characteristic time of the periodic structure.

Chapter 5 considers the effects of a spatially structured and time correlated noise on the motion of a spiral wave for the photosensitive BZ reaction and for the Oregonator model. The major effect is to induce a Brownian motion of the spiral tip characterized by a coefficient diffusion which shows a rather complex dependence on the time and length scales of the noise relative to those of the spiral. In particular, a resonant-like

effect was observed with the time correlation and the noise dispersion fixed. A kinematically based model was proposed to interpret the spiral motion whose results are in good qualitative agreement with experiments and numerics.

In Chapter 6 a pacemaker, regularly emitting chemical waves, is created out of noise when the excitable photosensitive BZ reaction, strictly unable to autonomously initiate autowaves, is forced with a spatiotemporal patterned random illumination. These experimental observations are also reproduced numerically, and further analytically interpreted in terms of genuine coupling effects arising from parametric fluctuations. Within the same framework we also address situations of noise sustained propagation in subexcitable media.

And finally, the main conclusions of this thesis are gathered together in Chapter 7.

Chapter 1

Active Media and Pattern Formation Far from Equilibrium

1.1 Introduction

Since the Belgian Nobel laureate Ilya Prigogine showed in 1944 that macroscopic spatial structures can emerge in systems driven far from equilibrium, the thermodynamics of nonequilibrium [18, 19, 20, 21, 22, 23] has become one of the main branches of modern physics. Pattern formation phenomena occurring in systems of very different nature (physical, chemical, biological and even social) result in a plethora of *Dissipative structures*[1], as baptized by Prigogine himself. A browse of almost any journal in the field reveals the variety of examples of pattern formation, as they occur in galaxies [24], the atmosphere, semiconductors and gas plasma [25, 26], liquid crystals [27], lasers [28, 29], models of morphogenesis and population dynamics [30, 31], fluid convection [32], autocatalytical chemical reactions [33, 34], etc. Figure 1.1 shows the astonishing similarity of nonequilibrium patterns originated in completely different systems: a galaxy on the left and a storm on the right. On a grand scale, patterns in galaxies have much in common with those in interacting chemicals or in the aggregation of microorganisms [35]. The fact that similar phenomena appear in widely different contexts shows that quite different microscopic processes may lead to the same macroscopic patterns. This means that

---

[1]They are called *dissipative structures* because systems organize themselves into ordered structures overcoming dissipation in response to an external stress.
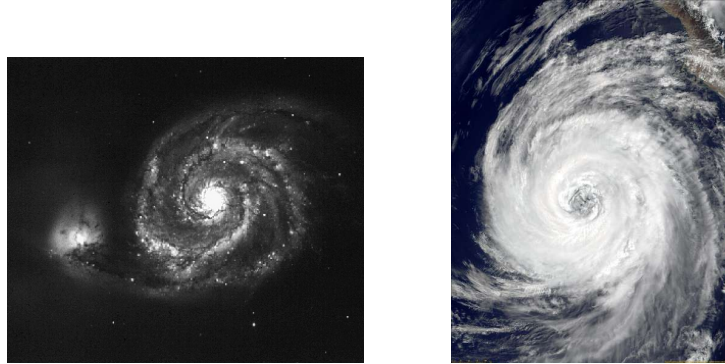
Figure 1.1: Formation of spiral structures in the Rosses's Galaxy (left, http://www.seds.org/messier/m/m051.html) and in a storm (right, http://visibleearth.nasa.gov/Sensors/Terra/). Despite the similarity, the microscopic mechanisms underlying the formation of these structures are completely different.

they are not induced by the microscopic dynamics and we should look not only for their common symmetries but the underlying mechanism that gives rise to self-organization and the onset of a macroscopic structure.

When a system is brought away from thermal equilibrium by applying external constraints, it may go through a series of instabilities that destroy the symmetries of the original state, leading to a new solution. This is the case of the well-known Rayleigh-Bénard instability in fluid convection, where a thin layer of silicone oil heated from below gives way to an array of hexagonal convection cells out of an initial uniform or conducting state [21].

While hydrodynamic instabilities have been studied since the beginning of the twentieth century, the spatial structures that appear in chemical active media were at first considered the result of bad experimentation, impurities, etc., and they aroused little interest compared to the patterns developed in hydrodynamical systems. Nevertheless, chemical patterns have been observed in numerous systems and their relation to various biological phenomena (morphogenesis, cardiac and neural activity...) is now well established. While forces and flows are central to fluid systems, patterns occur in chemical systems because of the interplay of reaction and diffusion processes. This two simple factors could lead to a wide range of pattern forming instabilities, as Alan Turing in 1952 showed in his remarkable paper [30] on the chemical basis of morphogenesis, which opened up new fields to the study of active media.

By an active medium we understand a system of autonomous elements distributed continuously in space, such that each of them possesses

nonlinear dynamical properties and interacts with the surrounding units according to the laws of diffusion. Depending on the nonlinear properties of the local units, each element can transit through different states either under the influence of an external perturbation or spontaneously, and give rise to an excitation pulse that propagates through the system by diffusion coupling. So, an active medium is an assembly of a large number of identical local elements that self-organize as a consequence of cooperation, giving rise to a more complex structure.

Cooperative processes are well documented in diverse chemical and biological systems such as the Belousov-Zhabotinsky (BZ) reaction [13], the propagation of nerve pulses, heart beats and the aggregation of slime molds, to name a few. In the special case of the heart, (for a review see [36]), circular waves of electric impulses initiated at the sinus atrial node spread over the walls of the heart, and they are the responsible of the pumping of the heart. But more complicated spatiotemporal behavior can occur if the heart tissue presents some kind of obstacles (damaged tissue) that favor the formation of a "re-entrant", a repetitive propagation of a wave through the same closed pathways in the tissue (see Fig. 1.2).

These re-entrants may be identified with the theoretical concept of a spiral wave when the circulation pathways are not around any anatomical obstacle in the tissue, but around functionally determined propagation blocks caused by the re-entrant wave itself. It is believed that these abnormal spatiotemporal patterns are associated with some cardiac disorders as cardiac arrhythmia or tachycardia [37, 38]. The medical implications warrant a detailed analysis of the spatiotemporal patterns during the processes of generation and propagation in the heart.

The BZ chemical reaction may serve as an aid to help us to understand the dynamics of the heart as well as other physiological systems. Arthur T. Winfree was the first one who showed the possibilities that chemical reaction-diffusion systems offer for the study of nonlinear waves and pattern formation [39]. The BZ reaction is one of the most convenient chemical reactions to perform experiments of any type and it was used in the studies presented in this thesis. Especially useful is the ruthenium-catalyzed version of the BZ reaction because it is light-sensitive allowing us to control its kinetics by projecting a pattern of illumination onto the reactive medium. We will be interested in those patterns in reaction-diffusion systems where the kinetics is spatiotemporally modulated. They exhibit a variety of behaviors not found in the corresponding homogeneous systems which are induced by the external fields. Many reaction-diffusion

Figure 1.2: Visualization of the development of ventricular fibrillation from a scroll wave in a computational model of the canine heart. From [40].
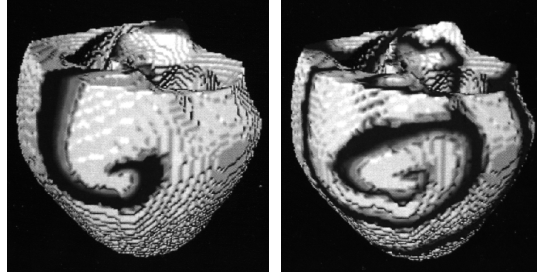
processes in nature take place in nonhomogeneous media or may be coupled to external processes that affect the kinetics in a nonuniform and complex fashion. The research presented in this thesis explores the phenomenology of spatiotemporal structures in active media subjected to both periodical and fluctuating fields of illumination and characterizes some of the phenomena quantitatively using numerical simulations and simple analytical models.

This chapter is organized as follows. In Section 1.2 a short introduction to reaction-diffusion systems is presented. This section is in turn divided in two subsections: in Section 1.2.1 the temporal dynamical behavior of the reacting system is studied, and in Section 1.2.2 some features of the propagation phenomena in the corresponding unstirred system are presented. Finally, in Section 1.3 a comparison between the descriptions of deterministic and stochastic dynamics is made, emphasizing the separation between the systematic motion and fluctuations when it is possible and when fluctuations can produce new phenomena that are absent from the deterministic scenario.

1.2 Reaction-Diffusion Systems

The phenomenology of pattern formation in active media can be represented mathematically in general form as follows:

$$\frac{\partial x_i}{\partial t} = f_i(\nabla x_i, x) + \nabla(D_i \nabla x_i) + g_i(x) F_i(\mathbf{r}, t) \qquad (1.1)$$

where the variables x_i determine the state of the system, f_i may be nonlinear functions of x and ∇x_i, D_i are the diffusion coefficients and $F_i(\mathbf{r}, t)$ are external fields that can be coupled to the dynamics of the system if $g_i(x)$ is not a constant function. In many cases, including the chemical system used in this thesis, f_i do not depend on ∇x_i and the diffusion

coefficients do not depend on the spatial variables. If we also consider the system free of any influences from outside, the generalized mathematical form describing the phenomenology of an active media will be the following:

$$\frac{\partial x_i}{\partial t} = f_i(x) + D_i \nabla^2 x_i \tag{1.2}$$

which corresponds to a reaction-diffusion system. The important feature of this system is the existence of different time scales and spatial ranges of diffusion for the different species which allows to reduce the dynamics of the whole system to that of few variables. Specifically, we are interested in a pair of reaction-diffusion equations of the activator-inhibitor type,

$$\varepsilon_u \frac{\partial u}{\partial t} = f(u, v, \phi) + l_u^2 \nabla^2 u \tag{1.3}$$

$$\varepsilon_v \frac{\partial v}{\partial t} = g(u, v, \phi) + l_v^2 \nabla^2 v \tag{1.4}$$

where u is the *activator* and v the *inhibitor* concentrations. Parameters ε_u and ε_v are the characteristic time scales, and l_u and l_v the characteristic length scales of the activator and the inhibitor, respectively. f and g are certain nonlinear functions and ϕ is the control parameter.

Equations (1.3) and (1.4) have been used to model several problems in physical, biological and chemical systems (see [31]). The rest of variables of the system have faster time scales, and according to the *slaving principle* [19] it is possible to disregard those variables that relax very fast to the stationary state. Pattern formation in activator-inhibitor systems is associated with a positive feedback of the activator u, known as *autocatalysis*, which results in "self-production of the activator substance"; this process of self-production is controlled by the inhibitor v that suppress the growth of the activator.[2] These two competing processes (where $\varepsilon_v \gg \varepsilon_u$) give rise to different kinds of patterns in these systems. The properties of the patterns and pattern formation scenarios in Eqs. (1.3) and (1.4) are mainly determined by the relationship between the length scales l_u and l_v, and between the time scales ε_u and ε_v, together with the shape of the nonlinear function in Eq. (1.3). In these systems we can find static (Turing patterns), pulsating, and traveling patterns.

From Eq. (1.2) two different problems can be isolated:

---

[2]An illustrative example will be the infectious agent as the activator and the immunity level as the inhibitor in the epidemic propagation.

- Analysis of the local dynamics, in the absence of diffusion ("point system").

- Analysis of the propagation phenomena, considering diffusion.

These two problems will be addressed in the next two subsections.

1.2.1 Reacting Chemical Systems. Stirred Systems

In the following we will focus exclusively in the chemical systems phenomenology. The diffusion terms in Eqs. (1.3) and (1.4) can be neglected whenever a careful mixing of the reagents has been performed, or the dimensions of the medium are small compared to the characteristic length ($r \ll \sqrt{D_i \varepsilon_i}$) associated to the state variables of the system. In this case we retrieve what is known as the "point system":

$$\frac{\partial u}{\partial t} = \varepsilon_u^{-1} f(u, v, \phi) \tag{1.5}$$

$$\frac{\partial v}{\partial t} = \varepsilon_v^{-1} g(u, v, \phi) \tag{1.6}$$

The above equations present different types of dynamical behavior depending on how the *nullclines* $f(u, v, \phi) = 0$ and $g(u, v, \phi) = 0$ of the stirred system intersect in the phase space (u, v). The intersections correspond to the stationary solutions of (1.5) and (1.6). The stability of these stationary points will depend on the signs of $\partial_t u$ and $\partial_t v$ around the nullclines. This will give the qualitative behavior of the orbits in the phase space.

In many cases, activator-inhibitor dynamics of the autocatalytic type are well described by cubic models as shown in Fig. 1.3. This figure presents a schematic plot of the *nullclines* for the Oregonator model (which will be introduced in Chapter 2) crossing at the point (u_0, v_0) (known as the rest state) and the signs of the reaction rates f and g for small deviations of the concentrations u and v from the point (u_0, v_0).

The different stability situations are shown in Fig. 1.4, namely: *bistable* (Fig. 1.4a), *excitable* (Fig. 1.4b), and *oscillatory* (Fig. 1.4c) behavior. In Fig. 1.4a the relative position of the *nullclines* (which depends on the parameters of the model) leads to the existence of three stationary points, two of them are stable fixed points, each one having its own basin of attraction (initial condition A belongs to the attraction basin of the rest
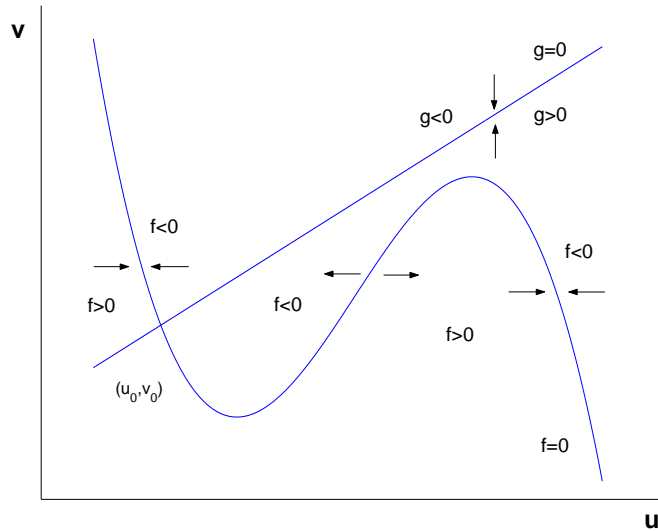
Figure 1.3: Schematic plot of the *nullclines* $f(u, v, \phi) = 0$ and $g(u, v, \phi) = 0$ of the Eqs. (1.5) and (1.6) for the special case of a cubic model like the Oregonator (Chapter 2). The stable and unstable branches are shown by the arrows towards or away from the *nullclines*.

state, whereas B to that of the rightmost fixed point). The system can go to either state depending on the initial conditions. If only a single stable fixed point is present, the system becomes excitable. Here again, certain initial conditions decay rapidly to the stable state (A in Fig. 1.4b), while others lead to large excursions before the system relaxes to the stable state (point B in Fig. 1.4b). In this case, the fixed point is globally attracting and this behavior underlies many phenomena in chemical and biological systems, in which after a burst of activity induced by a superthreshold perturbation the system returns to the rest state.

In the oscillatory case shown in Fig. 1.4c, there is only one unstable fixed point that gives rise to a stable limit cycle in its neighborhood through a Hopf bifurcation. The difference between oscillatory and excitable dynamics is that in the oscillatory regime there is no need of an initial supercritical perturbation to produce an excursion through the phase space.

Another important feature concerning the motion of the phase point through the phase space is how fast are the variations during one oscillation. In general, the motion will be nonharmonic, corresponding to a relaxation oscillator, due to the very different reaction rates ε_u and ε_v. According to this, the phase point goes rapidly from B to the attracting branch of
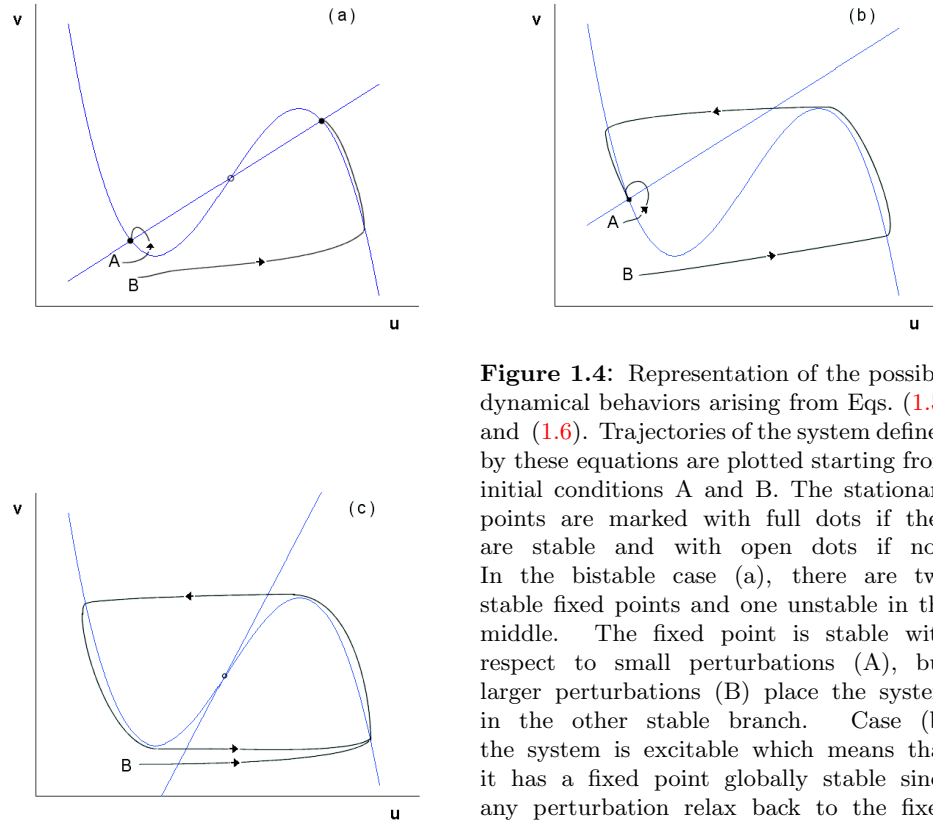
Figure 1.4: Representation of the possible dynamical behaviors arising from Eqs. (1.5) and (1.6). Trajectories of the system defined by these equations are plotted starting from initial conditions A and B. The stationary points are marked with full dots if they are stable and with open dots if not. In the bistable case (a), there are two stable fixed points and one unstable in the middle. The fixed point is stable with respect to small perturbations (A), but larger perturbations (B) place the system in the other stable branch. Case (b) the system is excitable which means that it has a fixed point globally stable since any perturbation relax back to the fixed point, which sometimes may involve a large excursion before relaxation. (c) Oscillatory system exhibiting large amplitude relaxation oscillations approaching a limit cycle associated with the unstable fixed point.

the nullcline $f = 0$, and then moves slowly up this branch until it reaches the top of the nullcline. From this point, the system jumps to the other attracting branch and finally goes down slowly this branch. If the system is excitable, it will end up relaxing to the fixed point. On the other hand, if the system is oscillatory, it will go down to the lowest part of the nullcline $f = 0$ and will jump back the opposite attracting branch and so on. In any case, the system performs a large-amplitude cycle with alternating fast and slow variations. Note that after excitation the system spends a long time along the left branch of the slow manifold where it is not susceptible to small perturbations. During this time the system is in its *refractory period* $t_{refract}$ and the total duration of the excursion through the phase space

after excitation is named *recovery time t_{recov}*.

At this point, we have seen the different dynamical regimes we can find in a stirred system. In what follows we will introduce the possible types of patterns and their behaviors in the systems under consideration, reaction-diffusion systems of the activator-inhibitor type.

1.2.2 Propagation Phenomena. Spatially Extended Systems

What happens with the previous analysis of the Section 1.2.1 if we consider diffusion?. Different scenarios will arise depending on the relationship between the characteristic length scales l_u and l_v. Specifically, when the inhibitor is slower and shorter-ranged than the activator, only traveling or propagating patterns may exist. On the other hand, when the inhibitor is long-range and fast compared to the activator, only static dissipative patterns may form, known as Turing structures. We will focus on traveling patterns and their properties in both one-dimensional and two-dimensional cases.

1.2.2.a 1D Pulse Propagation

The most basic consequence of diffusion is the existence of propagating fronts due to an initial local disturbance in the medium. This perturbation propagates without attenuation, in contrast with a purely diffusive medium with no intrinsic dynamics where the amplitude of the perturbation decreases as it spreads from the initiation point. These structures in dissipative media are referred to in the Soviet literature as "autowaves" [41, 42]. Their character depends on the regime of the system. In a bistable medium, they are trigger fronts connecting the two stable states. In the oscillatory regime there exist phase fronts in the form of different oscillation phases but constant amplitude. In the case of an excitable medium, in contrast to trigger waves, as the front propagates the medium goes back to its initial state of rest, giving rise to a propagating pulse with a leading edge (the jump from the steady state to the attracting branch in Fig. 1.4b) and the trailing edge (the jump from the top of the nullcline to the other attracting branch). This is the most interesting case for us because the excitable regime of the BZ reaction is the most common in the experiments.

The properties of propagating pulses are determined mainly by the interaction between u and v. The variable u is referred to as the trigger variable because the kinetics of u causes the excitability in the system, and
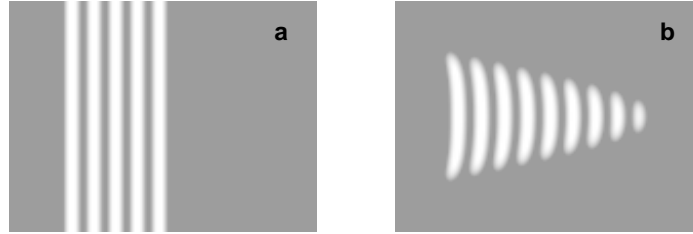
Figure 1.5: (a) 1D propagation in a nonexcitable medium: superposition of a propagating pulse (white lines) at different times (from left to right). Because the medium does not support propagation, the pulse fails to propagate and does not reach the end of the medium. (b) 2D propagation in subexcitable medium: snapshots of a pulse with free ends as it propagates from left to right. Because of the medium conditions, the pulse is not able to grow at its ends but shrinks until it totally disappears.

the variable v is called the recovery variable because together with u it is responsible for bringing the system back to the rest state. A special feature of excitable media is that any wave front is followed by a refractory tail in which the medium is not reexcitable during the refractory period. Almost all the features that autowaves share (namely, they do not penetrate each other and do not reflect in the system boundaries[3]) can be explained in terms of the existence of a refractory tail associated to each trigger front..

An excitable medium can support the propagation of a pulse with constant amplitude. The velocity and height of the pulse will depend on both the diffusion coefficient and the active properties of the medium. Specifically the width of the refractory tail is determined by the refractory period and the front velocity v ($\lambda_{refract} = v\, t_{refract}$) which is given approximately, for the case of chemical waves, by $v \backsim (K_u D_u)^{1/2}$ where K_u and D_u are the effective rate constant and diffusion coefficient of the trigger variable. But sometimes, there exist situations where the magnitude of the available amplification is not large enough to sustain stationary-amplitude autowave propagation. It is the case of a *nonexcitable* medium which is illustrated in Fig. 1.5(a). If a pulse is initiated in such a medium, it propagates through some distance until the amplitude becomes less than some critical value and disappears. The distances traveled by the pulses become larger as the properties of the system approach those of an excitable medium.

The velocity of a propagating pulse does not only depend on the excitability of the medium but also on its previous history. In case of a

---

[3]Similar to what happens when two fronts of fire collide in a fire-break.

pulse train created by periodically stimulating some localized region, the leading pulses condition the medium for the following ones and the train as a whole propagates differently from a solitary pulse. In general, there is a relationship between the wavelength and the velocity of the train that can be considered as a dispersion relation for nonlinear periodic waves. As the period becomes larger, the medium has time to relax back to the rest state and the propagation velocity will approach the velocity of a solitary pulse.

1.2.2.b   2D Propagation

In two spatial dimensions, the wave front is a line and the velocity is not only affected by previous activity but also depends on the shape of this line, that is, on the wave front curvature k. This is defined as positive when the center of curvature is behind the propagating front and negative in the opposite situation. A linear relation between the normal velocity of the front and the curvature k can be derived (see Appendix A and [43, 44, 45]) by considering ε_u small in Eq. (1.3) and using singular perturbation methods.
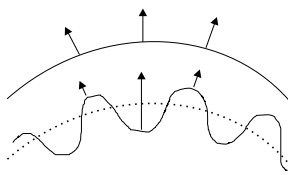
The result is known as the "eikonal" equation and express the proportionality between the normal velocity v_n and the curvature k of the moving wave. When k is positive the velocity of propagation is reduced, and speeds up the front when it is negative, according to the following equation,

$$v_n = v_0 - D\,k \qquad (1.7)$$

where v_0 is the velocity of a plane wave and D is the diffusion coefficient of the activator. This equation shows the stabilizing role of diffusion: the convex geometry defocuses diffusion whereas concave geometry focuses it, increasing the flux into the medium at rest state. This mechanism helps to stabilize the propagating front against short-wavelength perturbations.

This $v_n - k$ dependence has been investigated experimentally in the framework of the BZ reaction in [46, 47, 48] and in the heart tissue [49] and it was found to be valid only for slightly curved fronts. Experiments also confirm the existence of a critical minimal size below which propagation will not take place (from Eq. (1.7) $R_{crit} = D/v_0$). For very large negative curves, experiments show a strong deviation from the linear prediction and a nonlinear expression should be taken in these cases as it is demonstrated in [50].
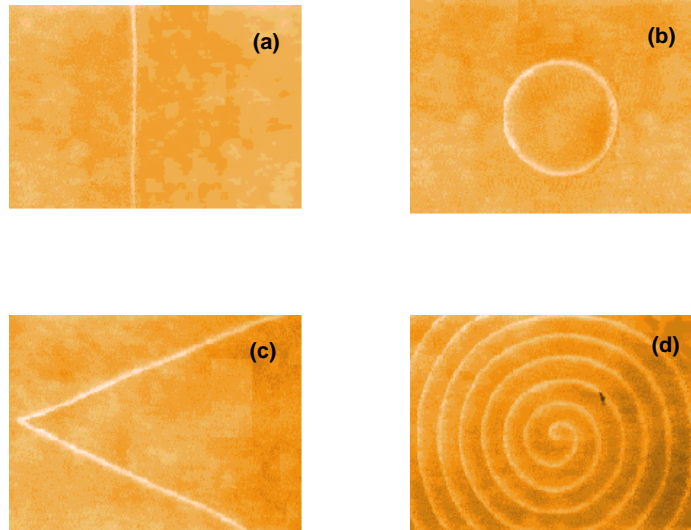
Figure 1.6: Different geometric forms of autowaves (from [51]).

In an spatially extended system it is possible to initiate planar wave (Fig. 1.6(a)) pattern by applying a perturbation along a line, or a circular wave (Fig. 1.6(b)) by means of a local perturbation which grows up keeping the shape constant. After a transient of higher curvature, circular waves approach to plane ones propagating at constant speed. Far away from the center, curvature effects are negligible. Both plane and circular waves have been used to test the eikonal equation by means of the collision of two plane waves or two circular waves to produce a V- shaped front (Fig. 1.6(c)) [48] and cusplike structures [46] respectively, with high negative curvature. But while the V-shaped patterns are stable the cusplike structures are not, so no reliable data can be obtained from them.

If the medium is perturbed periodically, plane and circular wave trains can be obtained. The latter are known as *target patterns* and they are found during Dictyostelium aggregation [35] or in the heart around the sinus atrial node [49]. In these examples target patterns are related to regions called *pacemakers* that present local oscillatory behavior. Sometimes they are nucleated on defects like dust particles or bubbles in the BZ reaction or dead cells in the heart tissue. The frequency at which they are emitted can vary depending on the local characteristics of the medium itself. Moreover, if there exist regions with different emission frequencies, the pacemaker with the higher frequency will survive and consume the lower-frequency

one.

Another common and striking pattern in two-dimensional excitable media is the spiral wave (Fig. 1.6(d)). Its wide occurrence in chemical and biological media makes it a target of intensive study [52]. Its origin is associated with a break in a propagating front that can be caused by nonexcitable heterogeneities in the medium [53, 54, 55, 56, 57] or with a perturbation in the tail of the back front which may originate a discontinuous front due to the vulnerability of the medium [58, 59]. Both mechanisms produce free ends that begin to curl up and become the *tips* of a two oppositely rotating spiral waves. The way the tip starts to curl is described in [43, 60] and depicted in Fig. 1.7. Basically, when the perturbation breaks the propagating front, there exists a point along the interface separating the excited and the recovery regions where the front no longer propagates forward uniformly. This induces a twisting effect on the interface motion that turns to rotate around some center (sprouting) to develop the spiral structure. The region around which the tip of the spiral rotates is the *core* whose size and shape depends on the excitability of the medium: in low excitable media the tip follows a circular trajectory ("rigid rotation") and the size of the core is large compared to the refractory tail $\lambda_{refract}$, while highly excitable media give rise to pointwise cores and the tip often performs a complex motion called "meandering" , with the trajectory often resembling the shape of a flower.

A broken wave front will develop into a spiral wave if the excitability of the medium is high enough to allow the expansion of the wave front at the tip, that is, besides moving in the normal direction, the wave front can sprout or contract at its tip. The velocity G of this tangent motion will depend on the curvature k of the wave front at the free end in a similar manner as given by the eikonal equation (1.7): $G = G_0 - \gamma\, k_0$, being G_0 the tangent velocity of the tip of a plane wave and k_0 the curvature of the wave front close to the tip. Thus, changes in the excitability change the velocity of sprouting G_0. The range of excitabilities at which G_0 is negative, i.e., the broken wave front contracts at its tip, is called *subexcitable* regime. Within this regime a wave front of finite length shrinks and finally disappears as it is shown in Fig. 1.5(b). As opposed to nonexcitable behavior (where the amplitude of the wave front decays, as moves forward, until it disappears), the subexcitable character can only emerge in 2D propagation because involves a contraction of a wave front perpendicular to its normal propagation. This particular regime will be treated in detail in Chapter 3.

Figure 1.7: Schematic representation of the formation mechanism of a spiral wave. An initial continuous propagating pulse is broken by its left side (a). The new created free end has room behind where to move and a new velocity component arises (b). The combination of the normal and the tangent velocities makes the pulse to rotate (c) which will lead to a fully developed spiral. Note that the sense of advance of the initial propagating pulse is downwards.
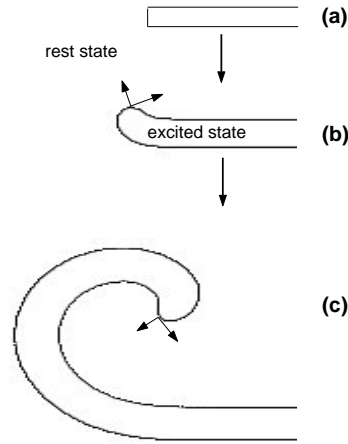
1.3 Deterministic *vs* Stochastic Dynamics

So far we have presented only deterministic equations giving the response of the system to any initial condition. But very often physical systems include noise sources which should be included in the dynamical equations [1]. This can be done by taking the deterministic Eq. (1.2) and introducing random fluctuations in a general way:

$$\frac{\partial x_i}{\partial t} = D_i \nabla^2 x_i + f_i(x, \phi) + g_i(x)\xi_i(\mathbf{r}, t) \tag{1.8}$$

where $\xi_i(\overrightarrow{r}, t)$ represents a stochastic force driving the dynamics of the variable x_i.

The different scenarios described by Eq. (1.8) can range from simple systematic motion that can be isolated from a noisy background (which will appear as an uncertainty in the data) to new phenomenology arising exclusively because of the presence of noise (for instance, new steady states which are absent in a deterministic scenario, or change of stability of a deterministic state).

Equations (1.8) represent a set of stochastic partial differential equations SPDE known under the name of spatiotemporal Langevin equations. The main difference between these equations and Fokker-Planck equations is that the former involve field variables while the latter deal with the probability densities. Depending on the term $g_i(x)$, the way the fluctuations are introduced can be additive or multiplicative. Additive noise ($g_i(x) = 1\,\forall i$) describes an uncontrollable microscopic situation with

unknown degrees of freedom. They are *internal* fluctuations like thermal or statistical that can not be avoided. Multiplicative noise ($g_i(x) \neq constant$) arises in experimental situations where some control parameter of the system fluctuates. In this case the noise is *external* because it is controllable from outside.

This is the case that will be further developed in this thesis, with spatiotemporal fluctuations of light intensity used to generate and perturb chemical waves. In order to obtain insight into the dynamical behavior of Langevin equations one has to resort to numerical simulations because of the impossibility to obtain exact analytical solution in most of the cases involving nonlinear terms. The numerical integration of stochastic differential equations is quite different from that of the ordinary differential equations. The presence of random terms requires averaging over many trajectories, each one corresponding to a particular realization of the stochastic term, or equivalently to a particular sequence of random numbers. The algorithms used in the numerical calculations are summarized in Chapter 2 for the different noise correlations functions considered in this work:

$$\langle \xi(\mathbf{r}, t)\, \xi(\mathbf{r}', t') \rangle = \sigma C \left(\frac{\mathbf{r} - \mathbf{r}'}{\ell}, \frac{|t - t'|}{\tau} \right) \tag{1.9}$$

where σ is the intensity of the noise, ℓ is its correlation length and τ its correlation time. We should note that in an external noise situation the noise parameters can be controlled externally and therefore both correlation parameters can be tuned independently of the noise intensity. In particular, we will address the behavior of our system under both colored and white temporal correlations.

Finally, we should mention that numerical and analytical calculi have been done in the Stratonovich sense whenever the noise terms entered in a multiplicative way. Within the chosen interpretation, besides the fact that considering the gaussian white noise is retrieved as the limit of a real noise when the temporal correlation tends to zero, the procedures of calculation concerning integration and derivation will follow the classical rules of mathematical calculus.

Chapter 2

Experimental Setup and Numerical Model

2.1 Introduction

There are many research groups around the world devoted to the study of complexity and dissipative structures in the field of chemical oscillations, and as an example we can name just a few of them: Kenneth Showalter's group at the West Virginia University [61], Harry Swinney's group at the University of Texas [62], Mario Markus's group at the Max-Planck Institut at Dortmund, Stephan Müller's group at the Magdeburg University [63], T. Yamaguchi at the National Institute of Materials and Chemical Research in Japan, and Vicente Pérez-Villar's group at the University of Santiago de Compostela [64], among others. The oscillating chemical reactions have been chosen as a convenient experimental system because they provide a controllable and relatively easy to model manifestation of complexity. This effort has helped in turn to develop mathematical models of biological processes in single cells and multicellular ensembles that are less accessible to experimental manipulations but share many common features with their chemical counterparts.

An interesting paper about the history of chemical waves and oscillations in a liquid-phase chemistry was published in 1991 by Anatol M. Zhabotinsky [65]. It turns out that the first reaction of the scientific community was that of refusal to accept the possibility of sustained concentration oscillations in a homogeneous reaction. Much effort was indeed devoted in trying to prove that the oscillations were caused by some heterogeneous process or deficiencies in the experimental technique.

Despite the fact that I. Prigogine had shown in 1944 that oscillations could exist in systems far from equilibrium, in 1951 B. P. Belousov was not allowed to publish his amazing discovery of the chemical reaction with color oscillations. It was not until 1960 that the research on self-organizing chemical reactions begun, when A. M. Zhabotinsky (a graduate student) started to investigate the Belousov's recipe and replaced some chemicals to improve the color change in the reaction, thus opening a very rich field of research.

Nowadays, the reaction discovered by Belousov and the different variants developed from the original recipe have come to be known as the Belousov-Zhabotinsky reaction. In Section 2.2 we will describe briefly the chemistry of this reaction and in Section 2.2.1 the photosensitive variant employed for the experiments in this thesis. Next in Section 2.3 we will describe the experimental setup and the calibration process. The different spatiotemporal patterns used to control the excitability of the BZ reaction are introduced in Section 2.3.2. Finally Section 2.4 is devoted to the "Oregonator model", a numerical model capable of describing many respects of the behavior of the real BZ reaction.

2.2 The Reaction of Belousov and Zhabotinsky. The FKN Model

The BZ reaction is called a chemical clock because of the oscillatory cycle involved in the reaction. In 1972, R. Field, E. Körös, and R. Noyes described, in what is known as the **FKN model**, the basic chemistry of the BZ reaction [66]: around thirty different chemical species, including intermediates, take part in the various interlocking cycles of chemical steps comprising the BZ reaction. The kinetic mechanisms involved in the BZ reaction are so complex that even nowadays new steps of the chemical reaction continue to be discovered.

The overall process is the oxidative bromination by acidic bromate of an organic substrate (generally malonic acid) catalyzed by an oxidation-reduction metal ion pair such as Ce^{3+}/Ce^{4+}, Fe^{+2}/Fe^{+3} or Ru^{+2}/Ru^{+3}. The reaction mechanism consists of three main parts schematically represented in Fig. 2.1:

I. The autocatalytic oxidation of the metal ion catalyst by bromate with $HBrO_2$ as the autocatalyst.

II. The reaction between $HBrO_2$ and Br^-.

III. The catalytic reduction of the metal ion by malonic acid connected with bromide ion production.
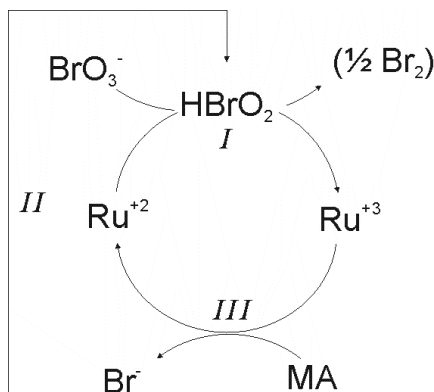
Figure 2.1: Schematic representation of the cycles involved in the BZ reaction. The autocatalytic production of the hypo-bromous acid ($HBrO_2$) induces the metal ion oxidation from oxidation state ($+2$) to oxidation state ($+3$) (I). This changes the color from yellow to white in the ruthenium catalyzed reaction. The oxidation states of ruthenium will change again due to the reduction by malonic acid (III). Because of the reaction between Br^- and $HBrO_2$ the autocatalytic oxidation is completely inhibited (II). The concentration of the Ru^{+3} decreases due to process III. The cycle repeats again when the concentration of the Br^- decreases enough to start the autocatalytic oxidation again and raise the concentration of Ru^{+3}.

When the metal ion oxidizes from the lower oxidation state to the higher one there is a color change in the reaction depending on the catalyst used. In the case of ruthenium, it changes from orange-colored to white, allowing to see concentration waves in an extended system or periodic color changes in a continuously stirred mixture if the reaction is oscillatory, Section (1.2.1). According to the FKN model, the system can be reduced by the method of quasistationary concentrations (based on the slaving principle) and be described by only three species which would lead the total dynamics. These three species are the $HBrO_2$ (which is the autocatalytic species and acts as the trigger variable), the catalyst which can be one of the metal ions mentioned above, and the Br^- an intermediate species which acts as the inhibitor of the reaction.

The BZ reaction's temporal behavior is often studied in a continuously stirred tank reactor (CSTR) where a control parameter (such as a reactant concentration or the inflow rate) is varied producing steady-state, periodic or chaotic behavior [67, 68, 66]. In unstirred thin films of solution or gels (to avoid convection), the BZ reaction displays different types of waves (see Section 1.2.2). Various properties of such waves (amplitude, velocity, front structure, dispersion relations, relation between curvature and velocity...) have been studied in detail (see [33] and references therein).

In this thesis we present two-dimensional studies of wave process in a

thin photosensitive gel. In the next sections, we will describe the chemistry and properties of the photosensitive BZ reaction catalyzed by ruthenium immobilized in a silica gel matrix, as well as the setup used to perform and monitor the experiments.

2.2.1   The Photosensitive Variant of the BZ Reaction

The influence of light on the BZ reaction has been known for some 30 years since V. Vavilin *et al.* [69] studied irradiation of a cerium-catalyzed BZ medium with ultraviolet (UV) light. They found that oscillations could either be altered or suppressed depending on the light intensity and the initial concentrations. Later on, H. Busse and B. Hess observed wave initiation by a spot of UV light in a ferroin-catalyzed BZ reaction [70]. In [71] they studied the effect of the visible light on the BZ reaction catalyzed by different catalysts and found that only the ferroin and ruthenium catalyzed systems were significantly affected.

The interest in systems that can be influenced by light lies in studies of spatiotemporal behavior, since they can be controlled adjusting locally or globally the illumination intensity. Among the light-sensitive BZ reactions, the system catalyzed by the ruthenium complex $Ru(bpy)_3Cl_2$ is a good candidate because light with wavelength around 450 nm changes the underlying chemical reaction affecting the excitability properties [72, 73, 74]. Examples are the photochemical memory device in Kuhnert *et al.* [75, 76], where the image of a mask was reproduced in an oscillatory medium; the control of wave propagation along a stripe of higher excitability in [77]; the modulation of the frequency of a train of autowaves through a moving boundary in [78]; and the control of spiral waves by periodical modulation of the light intensity [79] or by a simple optical feedback loop [80].

The behavior of the BZ reaction with a ruthenium-based catalyst is strongly affected by exposure to visible light. The predominant effect is the reduction of the excitability in proportion to the illumination intensity. Taking the intensity of the light that reaches the reaction as the only control parameter and keeping the initial concentrations of the reactants constant we observe, as shown in Figure 2.2, different regimes of system behavior for gradually increasing light intensity. For low light intensity, phase waves can be observed in oscillatory media. As the light intensity is increased above some value the medium becomes excitable and trigger waves can propagate only if they are initiated somewhere. For higher values of the light intensity the system enters in the subexcitable region, where waves
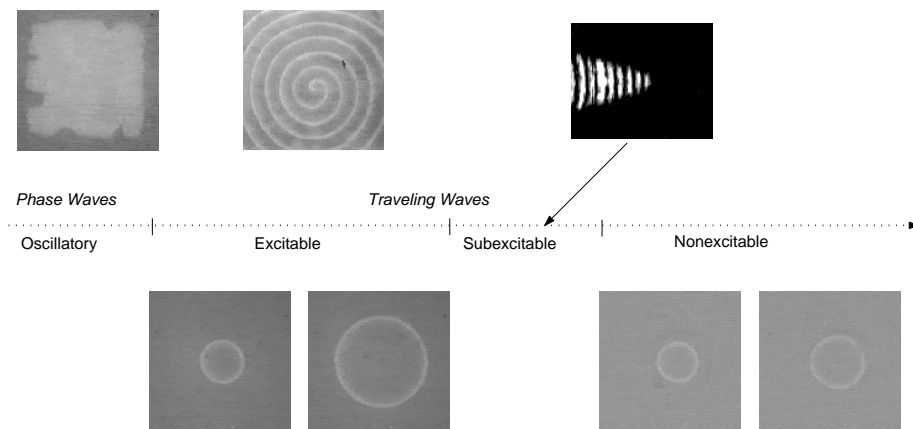
Figure 2.2:   Sequence of images showing the effect of the light intensity on the ruthenium- catalyzed BZ reaction. From left to right, light intensity increases and the reaction changes from oscillatory to nonexcitable, passing through excitable and subexcitable conditions in the middle. Phase waves are characteristic of oscillatory media and trigger waves are present in the rest of excitable levels.

with free ends propagate forward but shrink. Finally, for high enough values, light illumination inhibits wave propagation completely.

Several mechanisms have been proposed to explain the dual effect of light on the BZ reaction, namely, the induction of oscillations for low-intensity illumination and the inhibition of chemical wave activity for high-intensity illumination. These two processes have been explained in [72]. The first photochemical process is the absorption of a photon of wavelength 452 nm by the $Ru(bpy)_3^{+2}$ complex:

$$Ru(II) \rightleftharpoons Ru(II)^* \tag{2.1}$$

After the photoactivation of $Ru(bpy)_3^{+2}$, which is proportional to the light intensity, this can reacts in two separate ways:

I. $Ru(II)^* + BrMA \rightarrow Ru(III) + Br^- + org.\,prod.$

II. $Ru(II)^* + Ru(II) + BrO_3^- + 3H^+ \rightarrow 2Ru(III) + HBrO_2 + H_2O$

The first process involves the reduction of the bromomalonic acid to produce bromide. It also produces Ru(III) which, according to the FKN

mechanism (see Section 2.2) is the primary agent in generating Br^- via its reduction by malonic acid. In the second process, $HBrO_2$ is generated from the reduction of BrO_3^- in low-intensity illumination conditions. These two mechanisms account both for experimentally observed high-intensity inhibition and low-intensity induced oscillations. The former is due to the fact that the generation of Br^- (the inhibitor in this system) is proportional to the light intensity while the latter is due to the production of the autocatalyst $HBrO_2$, the crucial propagator species.

2.3 Experimental Setup

The experiments were performed in the setup depicted in Fig. 2.3. The setup can conceptually be separated into three main parts according to their function: illumination, reaction and acquisition.

A Sony CPJ-D500 video projector (1) was used to illuminate the reaction from below. This device allows to project fields of illumination with eight-bit gray scale between 0 and 255 not only varying in space but also in time [10, 11, 16]. These patterns are dynamically generated by a PC (10). The projected image is focused on the top of a diffuser-glass (3) with the help of a lens (2) and the objective lens of the video projector (1). The diffuser-glass (3) has two purposes: enhance the contrast of the transmitted light monitored through a CCD camera (Sony SSC-M350CE) (7), and equalize the spatial inhomogeneity produced by the bulb in the video projector (80 W).

The BZ reaction was carried out in a spatial closed reactor (4). The reaction consists in a liquid solution and a layer of gel (1 mm) cast on a glass plate. The gel (a silica gel, [81]) serves as a matrix in which the catalyst is immobilized, avoiding in this way hydrodynamic perturbations. The aqueous solution is a mixture of KBr, $NaBrO_3$, malonic acid, and H_2SO_4 that covers the gel[1]. With typically used concentrations the system sustaines waves for somewhat more than 2 h. Thus, to avoid spurious effects due to the aging of the system, we kept observation times as short as possible. The room temperature was kept at $25 \pm 1°C$ with the help of an air-conditioning device. The details of the reaction recipe can be found in the Appendix B.

The quasi-two-dimensional spatiotemporal patterns developed in the BZ reaction are monitored (8) and recorded (9) in transmitted light using a vertically placed CCD camera (7) and a band-pass filter (6) at 450 nm.

---

[1]The used concentrations will be given each time an experiment is described.
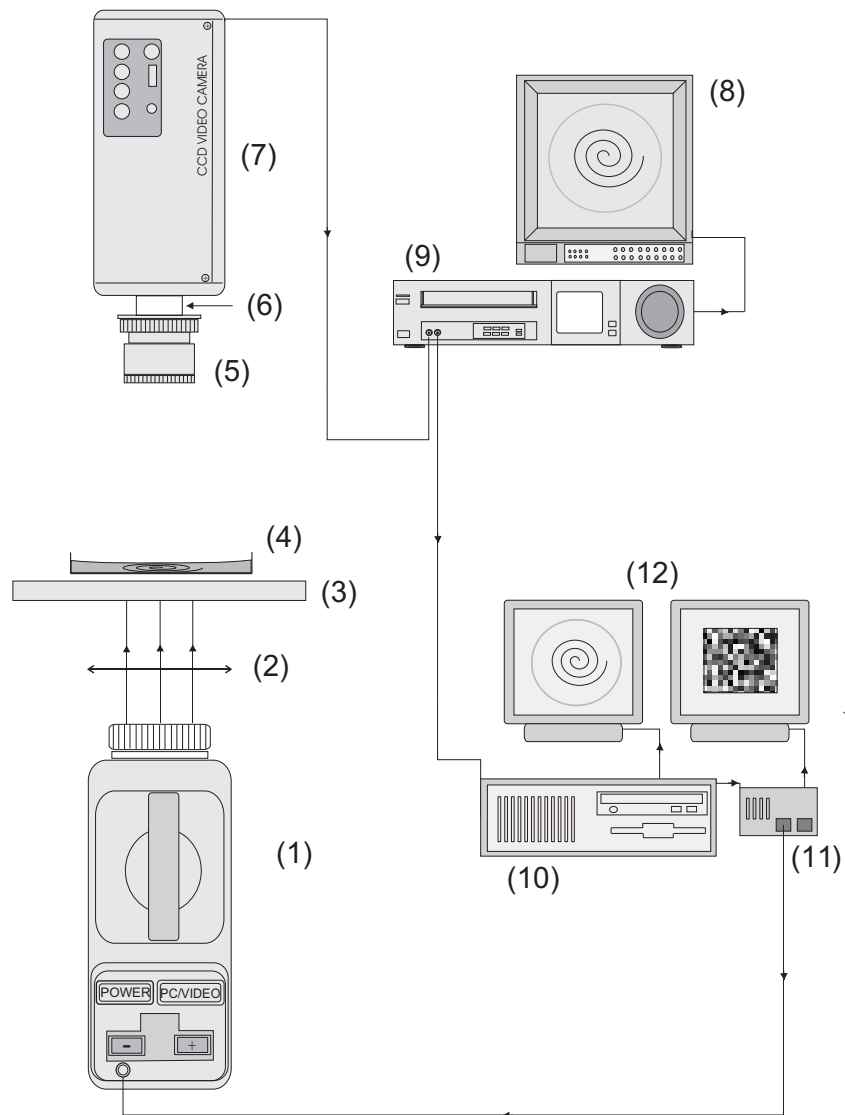
Figure 2.3: Schematic representation of the experimental setup: (1) video projector, (2) lens, (3) diffuser-glass, (4) sample dish, (5) objective lens, (6) interference filter, (7) CCD camera, (8) TV monitor, (9) video recorder, (10) PC, (11) signal splitter, (12) PC monitors.
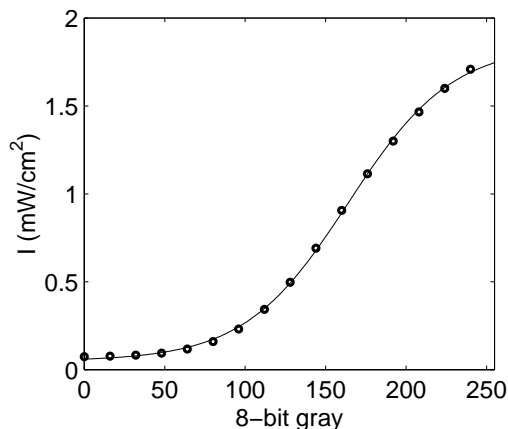
Figure 2.4: Calibration curve of the transmitted light through gray levels from 0 to 255. Light intensity (mW/cm^2) was measured with a photodiode (Appendix B) in a squared region of a given gray level. Points were fit to a sigmoidal curve: $I = GrayToVolts(G) = \frac{a_1-a_2}{1+e^{(G-G_0)/dG}} + a_2$, $a_1 = 0.05$, $a_2 = 1.85$, $G_0 = 164$, $dG = 32.33$.

The use of the filter helps to enhance the contrast since this wavelength corresponds to the maximum in the absorption spectrum of the ruthenium complex $Ru(bpy)_3^{+2}$. The observed images are monitored (12) on a PC, digitized by an image-acquisition card (miroVideo DC30 plus) and analyzed using a PC (10). A signal splitter (11) allows the signal corresponding to the eight-bit gray pattern be monitored and projected at the same time.

2.3.1 Setup Calibration

The level of excitability on the reaction medium depends on the intensity of the light from the projector reaching the gel. Different levels of intensity are set by projecting different gray levels from 0 to 255 out of 256. Before performing an experiment it is necessary to determine the transmission function, that is, the transmitted light intensity as a function of the gray level.

A photodiode (see Appendix B) was used to measure the light intensity at a point on the diffuser-glass. The dependence was found to be nonlinear as shown in Fig. 2.4. For darkest and brightest gray levels the light intensity is almost constant and only for intermediate values there is a linear response from the projector to changes in the gray level. This calibration curve corresponds to an operation mode of the video projector characterized by specific brightness and contrast settings. The knowledge of this relationship allows us to project precisely the desired illumination field in each point through the corresponding gray level distribution according to the calibration curve.

The next step in the calibration process is to determine the level of

excitability corresponding to each value of the light intensity. An indirect way to do this is to measure the velocity of a trigger wave. Kuhnert and Krug studied the velocity of the waves in an undisturbed ruthenium system [74]. They found a linear relationship between the velocity and the product of bromate and sulfuric acid concentrations, so the more acid is there the reaction the higher the velocity is. The influence of visible light was also investigated in detail in [73]. Changes in the wave velocity proportional to the intensity of illumination were found as well as inhibition of wave propagation.

We have characterized this dependence particularly due to its application in our analytical study. In analytical models, the effects of the illumination are often introduced primarily through the dependence of the velocity on the intensity of light. Thus in order to compare experimental observations with theoretical predictions such dependence has to be determined. Figure 2.5 shows a typical experiment, where five short waves propagate along five stripes of different gray levels [82]. Initially, a large planar wave is created at the beginning of these stripes by projecting a black square, thus preventing light reaching this region which becomes oscillatory. When the phase wave above the dark region reaches the boundary between the oscillatory and excitable domains, it develops into a trigger wave with planar shape. The regions between each gray stripe are nonexcitable in order to separate the wave fronts propagating at different velocities. The velocities are calculated by measuring the distance traveled in a given interval time $\Delta t = t_f - t_i$. We have found a linear relationship between light intensity and wave velocity. However, for larger and lower values of the light intensity, this linearity is lost because the closeness to the oscillatory and nonexcitable regimes.

2.3.2 Spatiotemporal Light Intensity Distributions

In the next chapters we will find different spatiotemporal configurations of the illumination field or, equivalently, of the excitability. Thus it is convenient to introduce them right now and refer to this section each time we need it.

The spatial distribution is defined by $n \times m$ square cells, each one having its own light intensity. The parameters that will characterize each pattern are the *correlation time τ* and the *correlation length ℓ*. The correlation time τ is given by the time-correlation function of the illumination $\langle (I(t) \, I(t') \rangle$ and ℓ by $\ell = L_x/n = L_y/m$, where L_x and L_y are the dimensions along the X and Y directions.
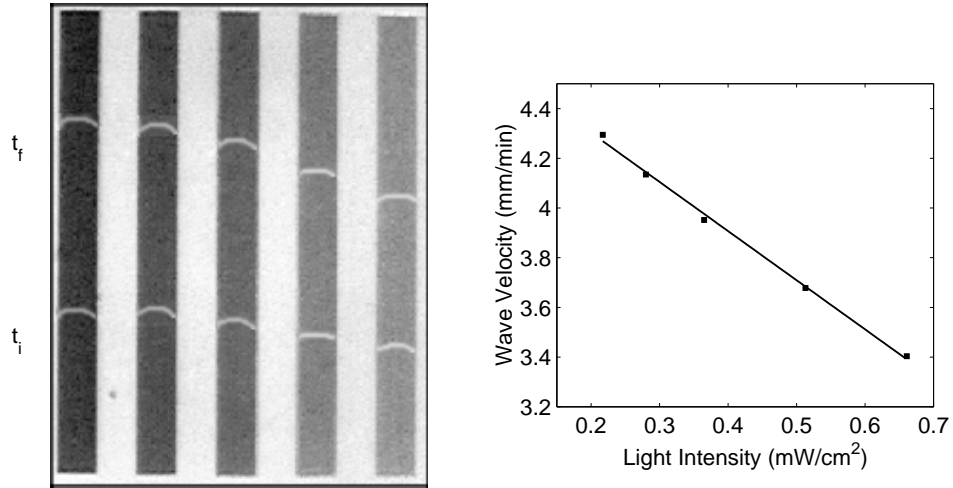
Figure 2.5: Left: Experiment to determine the light-velocity dependence consisting in five stripes of different light transmission values separated by 100% transmission regions. Each wave propagates at different velocity calculated as the rate between the space traveled between times t_i and t_f and $\Delta t = t_f - t_i$. Right: Velocity-light intensity relation.

In most cases random spatial configurations will also vary in time. The randomness can be defined here by following *Gaussian* or *dichotomous* distributions, described in detail in the following sections:

- Quenched dichotomous structured noise.

- Time correlated Gaussian structured noise.

- White Gaussian structured noise.

2.3.2.a Quenched Dichotomous Structured Noise

This is a static pattern that consists of an array of square cells of size ℓ, whose light intensities I are given by:

$$I(\mathbf{r}) = I_0 + \sum_{i=1}^{n}\sum_{j=1}^{m}\xi_{ij}\Theta_{ij}(\mathbf{r}) \tag{2.2}$$
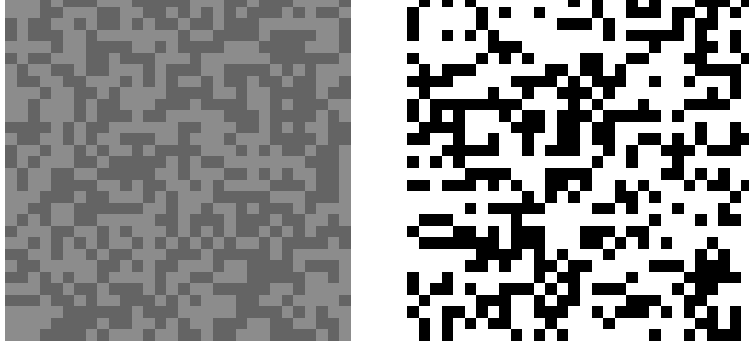
Figure 2.6: Examples of quenched dichotomous structured noise templates for the light transmission. Each of them is characterized by the cell size ℓ, the minimum correlation size, the two values of the distribution $I_0 \pm \Delta I$ and their probability. The pattern on the left side has both values in the excitable regime that occur with equal probability. The one on the right side is a typical template to study percolation phenomena because black cells permit propagation while the white ones don't. The probability of occurrence of a black cell is in this case 0.4.

where

$$\xi_{ij} = \begin{cases} +\Delta I & \text{with probability p,} \\ -\Delta I & \text{with probability q=1-p,} \end{cases} \tag{2.3}$$

accounts for the random distribution and

$$\begin{aligned} \Theta_{ij}(\mathbf{r}) &= \Theta_{ij}(x, y) \\ &= \theta(x - (i-1)\ell)\,\theta(i\ell - x)\,\theta(y - (j-1)\ell)\,\theta(j\ell - y) \end{aligned} \tag{2.4}$$

for the spatial distribution. θ is the Heaviside function and (i, j) are the discrete coordinates of a noise cell [2]. The cell size ℓ, the noise dispersion ΔI and the seeding probabilities p and q are the characteristic parameters of this light field distribution. The mean value of I is $\langle I(\mathbf{r}) \rangle = \overline{I} = I_0 + \Delta I\,(2p - 1)$.

Two examples of this kind of transmission field are shown in Fig. 2.6. Specifically, these are the ones used in Chapter 4 to study how a quenched disorder affects wave propagation and gives rise to percolation phenomena. For the first case, it is required that $p = q = \frac{1}{2}$ (which means that $\overline{I} = I_0$), and $I_0 \pm \Delta I$ within the excitable regime. For the second one, $I_0 + \Delta I$ falls in the nonexcitable regime and p ranges from 0 to 1.

To generate these patterns, a random number generator from the *Numerical Recipes* [84], producing a uniform distribution, was used. A

---

[2]This particular notation was taken from [83].

vector of size $n \times m$, initialized to 0, contains the $p \times n \times m$ random positions marked with 1. Those sites that are still 0 will be filled with one value of the distribution and those marked with 1 with the other:

```
numcell=n*m
do k=1,numcell
   irnd(k)=0
enddo
numcell_g1=p*numcell
do while (numcell_g1.gt.0)
   pos=nint((numcell)*ran1+1)
   if (irnd(pos).eq.0) then
       irnd(pos)=1
       numcell_g1=numcell_g1-1
   endif
enddo
do i=1,n
   do j=1,m
      k=(i-1)*m+j
      pattern(i,j)=irnd(k)*(g1-g2)+g2
   enddo
enddo
```

where `numcell_g1` is the number of cells of type 1 filled with gray `g1`, and `g1` and `g2` are the two gray levels of the dichotomic distribution to be projected.

A specific algorithm for $p = 0.5$ was used in order to force the mean value I_0 per row:

```
do j=1,m
   do k=1,n
      irnd(k)=0
   enddo
   numcell_g1=n/2
   do while (numcell_g1.gt.0)
      pos=nint(n*ran1+1)
      if (irnd(pos).eq.0) then
          irnd(pos)=1
          numcell_g1=numcell_g1-1
      endif
   enddo
```

```
   do i=1,n
      pattern(i,j)=irnd(i)*(g1-g2)+g2
   enddo
enddo
```

2.3.2.b   Time Correlated Gaussian Structured Noise

A time correlated Gaussian structured noise can be described by the same expression (2.2) except for ξ_{ij} that now is time dependent with a Gaussian distribution. In the time domain, the random term $\xi_{ij}(t)$ is an Ornstein-Ulhenbeck process generated by a linear damping equation driven by white noise ξ^w:

$$\frac{d\xi_{ij}}{dt} \quad = \quad \frac{-1}{\tau}\,\xi_{ij} + \frac{D}{\tau}\,\xi^w_{ij} \tag{2.5}$$

$I_{ij}(t) = I_0 + \xi_{ij}(t)$ corresponds to a Gaussian distribution, correlated in time with first and second moments given by:

$$\langle\, I_{ij}\,(\,t\,)\,\rangle \quad = \quad I_0 \tag{2.6}$$

$$\langle\, I_{ij}\,(\,t\,)\,I_{ij}\,(\,t'\,)\,\rangle \quad = \quad (D/\tau)\,exp(-\,|\,t-t'\,|\,/\tau) \tag{2.7}$$

for each (i,j) cell, as it is shown in Fig. 2.7. Cells are independent and characterized by a spatial correlation ℓ, a correlation time τ, a mean value I_0, and a noise dispersion $\sigma^2 = D/\tau$. The exponentially correlated noise $\xi(t)$ was obtained at each site (i,j) by an integral algorithm suggested by Fox *et al.* [85].

Briefly, this pattern was generated by using the algorithm cited above and a normal deviates generator from *Numerical Recipes* based on the *Box-Mueller* method. Every cell evolves independently from the others with the same mean I_med and standard deviation `sigma`:

```
call itime (iarray)
idum=-iarray(1)*iarray(2)*iarray(3)+1  /Initializing the seed
                                /with the clock of the system
do n=1,1000
   dato=ran1(idum)
enddo
expdttau = exp(-dt/tau)
desvnoise=sigma*dsqrt(1.-expdtau**2)
g_med=Inv(GrayToVolts)(I_med)
```
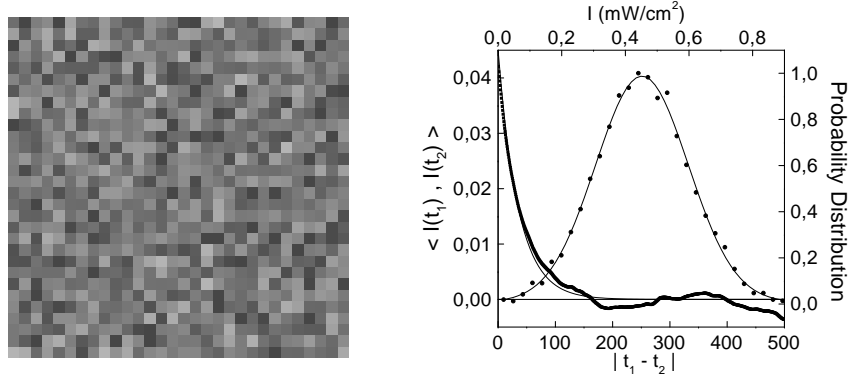
Figure 2.7: Left: example of a Gaussian structured noise transmission pattern. Right: characterization of the probability distribution and correlation function of the light intensity at one cell randomly chosen from the pattern on the left.

```
do t=1,10000,1
   do i=1,n
      do j=1,m
         aleat = gasdev(idum)
         noise(i,j)=noise(i,j)*expdttau+desvnoise*aleat
         pattern(i,j)=g_med+nint(Inv(GrayToVolts)(noise(i,j)))
      enddo
   enddo
enddo
```

being `Inv(GrayToVolts)` the inverse of the function that converts gray levels to mW/cm^2 according to the calibration curve given in Fig. 2.4. The meaning of the time scale given by `tau` is clearly shown in Fig. 2.8 where the auto-correlation of the noisy variable at different lags is investigated. When the lag is of the order of `tau`, which occurs in the forth case, the correlation is completely lost and a cloud of points develops along the diagonal of the first quadrant. Experimentally, the cells are updated every 100 ms, which is the fastest rate allowed by the computer which has to fill the matrix with the gray values to be projected and display them through the video card. This latter operation takes most of the time between consecutive updates.

2.3.2.c   White Gaussian Structured Noise

This last case of Gaussian structured noise shares the same probability distribution features of the preceding one. The difference lies in the time
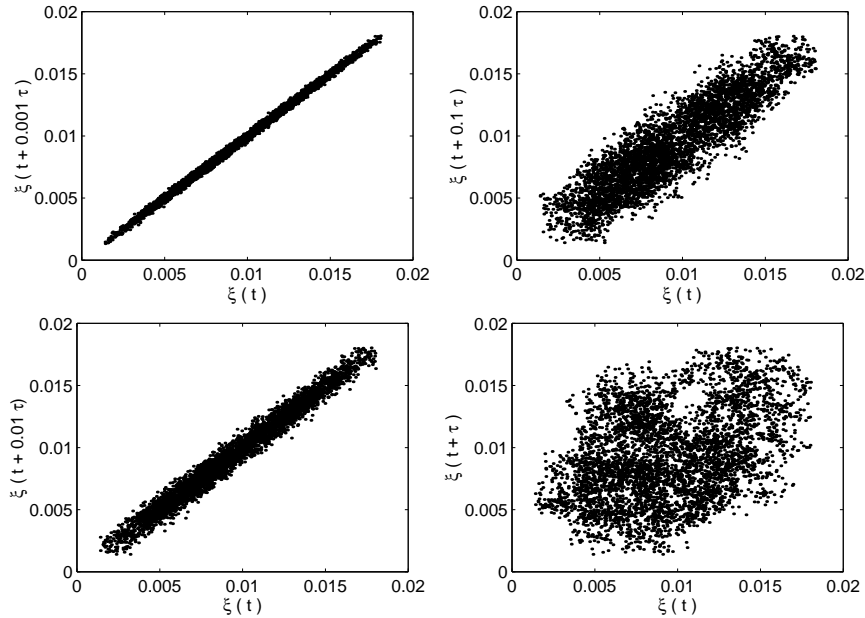
Figure 2.8: Representation of the auto-correlation of a time correlated series $\xi(t)$ for different lags. From top to bottom, and from left to right, the lag increases until it becomes of the order of the correlation time τ. The result is an increasing dispersion out of the diagonal.

evolution of each cell. Now there is no memory, and the present value of the noise is completely independent to the previous one:

```
do t=1,10000,1
   do i=1,n
      do j=1,m
         aleat = gasdev(idum)
         noise(i,j)=sigma*aleat
         pattern(i,j)=g_med+nint(VoltToGray(noise(i,j)))
      enddo
   enddo
enddo
```

The small time (100 ms) taken by the computer to refresh the array `pattern` ensures fluctuations with extremely small correlation time, approaching an effective white noise limit.

2.4 Oregonator Model

2.4.1 Introduction

The complex chemical mechanism proposed by Field, Körös and Noyes [66] at the University of Oregon, and described in Section 2.2, results in a simple model called *Oregonator* involving only three intermediate species and several reactants whose concentration is considered constant [86]. This model can be modified [87] to describe the photosensitive $Ru(bpy)_3^{+2}$-catalyzed BZ reaction:

$$A + Y \rightarrow P + X \tag{2.8}$$

$$X + Y \rightarrow 2P \tag{2.9}$$

$$A + X \rightarrow 2X + 2Z \tag{2.10}$$

$$2X \rightarrow P + A \tag{2.11}$$

$$Z \rightarrow hY \tag{2.12}$$

$$\xrightarrow{\phi} Y \tag{2.13}$$

where $A=BrO_3^-$, $P=HBrO$, $X=HBrO_2$, $Y=Br^-$, and $Z=Ru(ox)$, h is a stoichiometric factor, and ϕ the bromide flow due to the photochemical effects (also accounting for the oxygen effects). The parameter ϕ plays the same role as the light intensity does in the real experiment and models the photosensitive property of the BZ reaction.

By applying the law of mass action to reactions (2.8)–(2.13) and using the Tyson– Fife scaling procedure [88], we obtain a set of three ordinary differential equations which describes the dynamics of the Oregonator model:

$$\varepsilon \frac{du}{dt} = u(1-u) + w(q-u) \tag{2.14}$$

$$\frac{dv}{dt} = u - v \tag{2.15}$$

$$\varepsilon' \frac{dw}{dt} = \phi + fv - w(q+u) \tag{2.16}$$

where u, v, w are the dimensionless concentrations of $HBrO_2$, $Ru(bpy)_3^{+2}$ and Br^-, respectively; ε, ε' and q are the scaling parameters; $f = 2h$ is an adjustable stoichiometry parameter.

Equations (2.14)–(2.16) can be reduced to a system of only two equations by using the smallness of the parameter ε' in Eq. (2.16) compared

to ε. As the fastest variable, w can be considered in constant equilibrium with the other variables, thus $\dot{w} \equiv 0$ and

$$w \;=\; \frac{\phi + fv}{u + q} \tag{2.17}$$

$$\varepsilon \frac{du}{dt} \;=\; u(1 - u) - (\phi + fv)\frac{u - q}{u + q} \tag{2.18}$$

$$\frac{dv}{dt} \;=\; u - v \tag{2.19}$$

With this reduced Oregonator model it is possible to reproduce the dynamical behaviors found in the BZ reaction, namely oscillations and excitability. Adding diffusion terms to the system it is also possible to model the formation and propagation of traveling waves of chemical activity.

Two sets of parameters have been used throughout the numerical simulations performed to model the different experimental situations. They are summarized in the following table, with the values of the parameter ϕ for which the system changes from oscillatory to excitable and from excitable to nonexcitable also included.

	f	q	ε	D_u	D_v	osc/exc	exc/nonexc
set 1	3	0.002	0.05	1	0	-0.005	0.024
set 2	1.4	0.002	0.01/0.03	1	0.6/0	0.005	0.078/0.087

Note that the diffusion coefficient of the variable v is zero in order to mimic that in the experiments the catalyst is immobilized in a gel matrix.

2.4.2   Numerical Integration of the Deterministic Model

The complete deterministic model is obtained by adding diffusion to Eqs. (2.18) and (2.19):

$$\varepsilon \frac{\partial u}{\partial t} \;=\; u(1 - u) - (\phi + fv)\frac{u - q}{u + q} + D_u \nabla^2 u \tag{2.20}$$

$$\frac{\partial v}{\partial t} \;=\; u - v + D_v \nabla^2 v \tag{2.21}$$

The parameter ϕ is a deterministic function of time and space.

The parabolic Eqs. (2.20) and (2.21) were numerically solved by using the *finite-difference method*. Functions $u(x, y, t)$ and $v(x, y, t)$ are represented by their values at the discrete points $x_i = i\Delta x$ and $y_j = j\Delta y$ and discrete times $t_n = n\Delta t$ with $i = 0, 1, \ldots, N_x$, $j = 0, 1, \ldots, N_y$ and $n = 0, 1, \ldots, N$ [3]. The grid spacings along the x and y-axes were taken to be equal $\Delta x = \Delta y = h$. The derivative terms in Eqs. (2.20) and (2.21) were substituted by a FTCS (Forward in Time Centered in Space) representation, accurate to first-order in Δt for the time derivative and to second-order in h for the space derivative:

$$\frac{\partial u}{\partial t} \approx \frac{u_{i,j}^{n+1} - u_{i,j}^n}{\Delta t} \tag{2.22}$$

$$\nabla^2 u \approx \frac{u_{i+1,j}^n + u_{i-1,j}^n + u_{i,j+1}^n + u_{i,j-1}^n - 4u_{i,j}^n}{h^2} \tag{2.23}$$

and the same discretization scheme for the v variable.

Substitution of Eq. (2.22) and (2.23) in Eqs. (2.20)–(2.21) results in the explicit equations for the u and v evolution:

$$u_{i,j}^{n+1} = u_{i,j}^n + \Delta t \left[\frac{F_{i,j}^n(u,v)}{\varepsilon} + \frac{D_u}{h^2} \nabla^2 u \right] \tag{2.24}$$

$$v_{i,j}^{n+1} = v_{i,j}^n + \Delta t \left[G_{i,j}^n(u,v) + \frac{D_v}{h^2} \nabla^2 v \right] \tag{2.25}$$

where F and G are the reactive functions and the Laplacian operators for the u and v variables follow a *5-point* scheme, as stated above in Eq. (2.23). Both time and space steps, Δt and h respectively, were chosen to ensure numerical stability ($\frac{2D\Delta t}{h^2} \leq 0.5$) and accuracy. In addition, h has been appropriately chosen to avoid the rectangular shape that wave fronts acquire as they propagate, induced by the anisotropy between the discretization axes and the diagonal directions introduced by the five point scheme.

2.4.2.a   Initial Conditions

Three kinds of initial conditions were used, namely:

1. Plane wave

---

[3]The spatial and temporal dimensions will be given, respectively, in space and time units which are defined as 1 s.u.= *grid points* $\times \Delta s$ and 1 t.u.= *time iterations* $\times \Delta t$, being Δs the grid size and Δt the time step.

2. Spiral wave

3. Rest state

The first initial condition corresponds to the simplest form of propagation. One side of the two dimensional rectangular medium is stimulated above threshold and followed by a refractory back. After this initial setup a straight line wave front is elicited.

A spiral wave is created when a continuous wave front (such a plane wave) is broken and one half of the medium is reset to the stationary state. This allows the other half to curl and develop a spiral wave.

The rest-state initial condition corresponds to having the variables at the stationary value for the whole system.

2.4.2.b Boundary Conditions

The final step to close the numerical scheme concerns the time evolution of the points on the boundary of the spatial region to study. For a two-dimensional medium, no-flux boundary conditions (NFBC) are commonly used through this thesis to mimic the presence of an impermeable physical barrier:

$$\left.\frac{\partial u}{\partial x}\right|_{\partial\Omega} = \left.\frac{\partial u}{\partial y}\right|_{\partial\Omega} = 0 \qquad (2.26)$$

Here, $\partial\Omega$ represents the boundary of the two dimensional medium and the same condition holds for the variable v. These equations are implemented for a rectangular medium of dimensions $N_x \times N_y$ grid points in the following way:

$$
\begin{aligned}
u_{i=0,j} &= u_{i=1,j} \\
u_{i=N_x+1,j} &= u_{i=N_x,j} \qquad \forall j \\
u_{i,j=0} &= u_{i,j=1} \\
u_{i,j=N_y+1} &= u_{i,j=N_y} \qquad \forall i
\end{aligned}
\qquad (2.27)
$$

Sometimes the implementation of periodical boundary conditions (PBC) was needed to simulate an infinite medium along one or two spatial

dimensions. In those cases, this was accomplished by setting:

$$
\begin{aligned}
u_{i=0,j} &= u_{i=N_x,j} \\
u_{i=N_x+1,j} &= u_{i=1,j} &\forall j \\
u_{i,j=0} &= u_{i,j=N_y} \\
u_{i,j=N_y+1} &= u_{i,j=1} &\forall i
\end{aligned}
\tag{2.28}
$$

Finally, a last type of boundary conditions are Dirichlet ones, which specify the values of the boundary points as a function of time. These were used to impose specific values on the variables at the boundaries or in cases with a pacemaker at the beginning of the medium.

2.4.3   Numerical Integration of the Stochastic Model

Differences in the numerical integration of Eqs. (2.20)- (2.21) arise when the term ϕ is no longer deterministic but fluctuates in time. They become stochastic partial differential equations (SPDEs), and require special treatment in their numerical simulation. We will follow the algorithms developed in [89, 1] to obtain the discretized form of Eqs. (2.20)-(2.21) with a random term that ranges from white noise to colored noise of the Ornstein-Ulhenbeck type, or quenched noise through a random spatial distribution of the field ϕ. The difference between white and colored noise is that the latter is in turn generated by a linear damping equation driven by white noise (Eq. (2.5)) whose evolution in time must also be simulated. Quenched situations do not require special numerical techniques as they can be simulated using the algorithms for PDEs. In any of these cases, the solution depends on the averaging over many simulations, each of which corresponds to a particular realization of the stochastic term.

The stochastic part to be integrated can be expressed in the following form:

$$
\frac{\partial u}{\partial t} = D_u \nabla^2 u + F(u, v, \nabla^2) + G(u, v)\xi(\mathbf{r}, t)
\tag{2.29}
$$

where $F = \frac{1}{\varepsilon}u(1 - u) - (fv + \phi_0)\frac{u-q}{u+q}$ is the deterministic part and $G = -\frac{u-q}{u+q}$ is the function that multiplies the noise term $\xi(\mathbf{r}, t)$ which has a general correlation function given by Eq. (1.9). Further we shall present two numerical algorithms used depending on wether the noise is white or colored in time.

2.4.3.a   Gaussian Noise White in Time

A noise white in time is characterized by the following correlation function:

$$\langle \xi(t)\xi(t') \rangle = 2D\delta(t - t') \tag{2.30}$$

where D is the noise intensity. For a spatially structured noise, $\xi(\mathbf{r}, t)$ in Eq. (2.29) is simulated by placing a ξ_{ij} with correlation (2.30) and Gaussian distribution within each cell of size ℓ. For a discretized medium with $N_x \times N_y$ grid points, it implies generating $\frac{N_x}{l} \times \frac{N_y}{l}$ totally uncorrelated Gaussian random numbers at each time step. Considering the k*th* cell, the algorithm to evaluate the variable u at time $t + \Delta t$ is given by:

$$
\begin{aligned}
u_{i,j}^{n+1} &= u_{i,j}^n + \frac{D_u}{h^2}\Delta t \nabla^2 u + F_{i,j}^n \Delta t \\
&+ G_{i,j}^n X_k^n + \frac{1}{2}G_{i,j}^n \frac{dG_{i,j}^n}{du}[X_k^n]^2 + \mathcal{O}\left(\Delta t^{3/2}\right)
\end{aligned} \tag{2.31}
$$

where:

$$X_k^n = \int_t^{t+\Delta t} \xi(t')\, dt' = \sqrt{2D\Delta t}\ \ \gamma^n \tag{2.32}$$

is a Gaussian random number with zero mean value and variance $\langle X_k^2 \rangle = 2D\Delta t$, defined in terms of γ^n (a Gaussian random number with zero mean value and variance equal to one). The algorithm used in simulations is of first order in Δt, which is more sensitive to the actual value of Δt and to the number of realizations than one with higher order terms in Δt. The Gaussian random numbers γ were generated most of the times by using the *gasdev* subroutine from *Numerical Recipes* [84], which in turn produces Gaussian random numbers by means of the *Box-Mueller algorithm*. In particular, the Gaussian random number generator proposed by [90] was used in the simulations performed in Sec. 4.2.

2.4.3.b   Gaussian Noise Colored in Time

The same procedure developed in Section 2.4.3.a applies for the case of noise colored in time of the Ornstein-Uhlenbeck type whose correlation function is given by:

$$\langle \xi(t)\xi(t') \rangle = \frac{D}{\tau}e^{-\frac{|t-t'|}{\tau}} \tag{2.33}$$

of variance $\sigma^2 = \frac{D}{\tau}$ and correlation time τ. Now, due to the fact that ξ_k is colored in time, the algorithm is much simpler than the one given in the

previous section for the white noise case:

$$
\begin{aligned}
u_{i,j}^{n+1} &= u_{i,j}^n + \frac{D_u}{h^2}\Delta t \nabla^2 u + F_{i,j}^n \Delta t \\
&+ G_{i,j}^n {\xi_k}^n + \mathcal{O}\left(\Delta t^{3/2}\right)
\end{aligned}
\tag{2.34}
$$

The calculation of ξ_k^n for each time step was performed by exactly solving the linear differential equation for ξ driven by white noise (Eq. (2.5)) leading to the following algorithm [85]:

$$
\xi^{n+1} = \xi^n e^{-\frac{\Delta t}{\tau}} + \sigma\sqrt{\left(1 - e^{-\frac{2\Delta t}{\tau}}\right)}\ \gamma^n
\tag{2.35}
$$

where γ^n is a Gaussian random number with zero mean and variance equal to one. For each time step and correlated cell, algorithm (2.35) has to be implemented to feed (2.34). The Gaussian random numbers γ were generated as in the previous section.

Chapter 3

Effects of Periodical Forcing on Wave Propagation

Abstract. *In this chapter the effect of space- and time-periodic forcing on wave propagation is investigated. The impact of domain shape on wave propagation in excitable media is considered using channeled domains with sinusoidal boundaries. Trains of fronts generated periodically at an end of the channel are found to assume a quasiperiodic spatial configuration which repeats periodically in time. The phenomenon is numerically studied using the Oregonator model. Spatial return maps for the height and position of the successive fronts are analytically obtained, and reveal the similarity between this spatial quasiperiodicity and the temporal quasiperiodicity appearing in forced oscillators. The effect of homogeneous modulation of the excitability is studied for a subexcitable system. Wave propagation in such system is made possible by periodical modulation of a homogeneous illumination field. The propagation can be understood in terms of an interplay between the radial expansion of the wave and the motion of its free ends as the excitability varies periodically. This description leads to a simple kinematic analysis that provides insights into the initial conditions and forcing parameters giving rise to sustained wave propagation.*

3.1 Introduction

Spatially extended dynamical systems display interesting and sometimes unexpected behavior in response to external perturbations [21, 33]. Temporal perturbations of excitable media [91, 92, 79, 16], as well as spatial modulations [93, 94] and spatiotemporal fluctuations [95, 96, 11, 10], give rise to new types of dynamical behavior. In this chapter, the effects of simple spatially homogeneous periodic modulations are investigated in two very different scenarios. In the first one, developed in Section 3.2, periodic modulation is introduced through the geometry of the boundaries. A wave

train propagates along a narrow excitable channel with sinusoidally varying width. The spatial frequency and the amplitude of the modulation are expected to nontrivially affect the spatial distribution of the fronts, since the propagation depends on the width of the medium. The second system presented in Section 3.3 makes use of temporal periodical modulation of the excitability in a subexcitable medium (Section 1.2.2), that is, a medium unable to sustain propagation of bounded fronts. Again, it can be presumed that changes in the forcing parameters such as the period and the amplitude of the modulation around the subexcitable state may lead to final states different from ones in absence of modulation. A parameter region is shown to exist, where the subexcitable character of the medium is inverted and propagation sustained.

3.2   Quasiperiodicity in a Sausage-Shaped Domain

Excitable media display a very rich spatiotemporal behavior with regimes ranging from fairly well ordered structures of propagating waves [33] to highly uncorrelated spatiotemporal chaos. The study of these features and their mutual connections provides insight for understanding and maybe eventually controlling phenomena of great practical importance, for instance the arisal of deadly fibrillations in cardiac tissue [97]. Similar ordered and turbulent patterns also occur in extended chemical reactors operating away from equilibrium conditions. In many of these applications, a crucial but frequently ignored ingredient is the presence of boundaries. For example, it has been shown that boundaries and obstacles in inhomogeneous media serve to either pin or repel spiral patterns [98, 49, 99, 100] or even to create them [57, 56]; moving boundaries [78], striped domains [101, 77] and propagation through narrow channels [102] have also been reported in the literature as nontrivial domain configurations, as they change the properties of waves such as their frequency [78] or their velocity [101, 77].

Unfortunately, the current understanding of boundary effects in nonlinear partial differential equations is rather incomplete, and sometimes surprisingly nontrivial behavior lurk behind the apparent simplicity of some problems. A recent study [103], for example, shows that relatively regular boundary conditions such as Dirichlet's on the banks of a sausage-shaped channel can elicit several types of spatial complexity such as frozen quasiperiodicity and chaos even in very simple reaction diffusion

equations. There, the axial coordinate along the channel acts as a 'time' in the equations describing the time-independent spatial patterns and the undulated boundaries play the role of a periodic force inducing chaos in a dynamical system that is nonchaotic in the absence of driving.

At the same time, propagation of waves in excitable media has been studied exhaustively in other contexts [33]. Due to their ubiquity in large two-dimensional systems, much of this work deals with spiral waves. In contrast, the propagation of front trains has received much less attention. This may seem surprising since the same spirals themselves can be regarded far from their cores as a periodic train of two-dimensional traveling fronts. These trains are characterized by a dispersion relation $c = c(\lambda)$, giving a relation between the constant front train velocity and its uniform spacing λ, and their dynamics is very simple. More complex behavior appears even in one-dimensional systems if the excitable medium recovers the rest state not monotonically but via damped oscillations [104]. In this regime, propagating wave trains often relax to irregularly spaced configurations of fronts that can be seen as spatial chaos.

Guided by the previous results obtained by Eguíluz et. *al* in [103], the purpose of the present study is to investigate the asymptotic propagation of excitable wave trains generated by local time-periodic stimulation at the end of a sinusoidally undulated channel [105]. This elongated configuration enables us to borrow concepts from the theory of dynamical systems since spatial longitudinal coordinate along the channel behaves as a *time-like* coordinate. The outline of this chapter is as follows. In Section 3.2.1 the method used to handle the boundary conditions is described within the framework of the Oregonator model. This consists of a coordinate change which brings the undulated domain into a rectangular one. The study has been performed by varying the parameters of the sinusoidal forcing and results are presented in Section 3.2.2 which is divided in two parts devoted respectively to strong and weak forcing. Finally, in Section 3.2.3 we present a more general analytic theory of the results obtained in Section 3.2.2.

3.2.1   Numerical Model

The simulations were performed on the Oregonator model given by Eqs. (2.20) and (2.21) with the parameters $f = 3$, $q = 0.002$, $\varepsilon = 0.05$, $\phi = 0.002$, $D_u = 1$, and $D_v = 0$[1].

---

[1]Unless explicitly indicated, all variables are dimensionless except for those given in space and time units. $\Delta t = 0.0005$, horizontal axis $\Delta x = 0.15$, vertical axis $\Delta y = 0.05$.
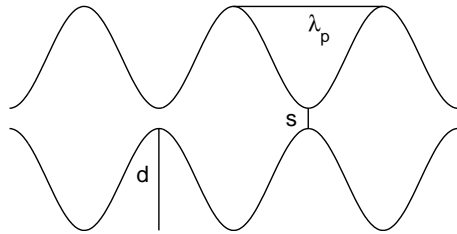
Figure 3.1: Channel-like domain of integration with sinusoidal boundaries. The upper and lower curves are defined by the functions $y_0(x)$ and $y_1(x)$. The modulated distance between them is given by $\Delta(x) = s + d - d\cos(\frac{2\pi x}{\lambda_p})$.

The spatial domain of integration is tailored as sausage-shaped channel along the longitudinal direction as shown in Fig. 3.1. The transverse coordinate y is bounded by two sinusoidal walls, $y_0(x)$ and $y_1(x) = s - y_0(x)$, with

$$y_0(x) = -\frac{d}{2}[1 - \cos(kx)] \qquad (3.1)$$

The spatial frequency is $k = 2\pi/\lambda_p$, the undulation amplitude d, the minimum separation s, and the transverse distance between the boundaries $\Delta(x) = y_1(x) - y_0(x) = s + d - d\cos(kx)$. At the boundaries we impose the Dirichlet condition $u(x, y_0, t) = u(x, y_1, t) = 0.004$, a value close to the fixed point of the local dynamics (this could be implemented in the photochemical BZ reaction by annihilating any excitation in the exterior of the domain via strong enough illumination. In contrast, a physical barrier -such as the border of a Petri dish or any obstacle in the medium- would imply zero-flux boundary conditions).

An efficient way described in [103] to solve numerically Eqs. (2.20)-(2.21) within the region limited by $y_0(x)$ and $y_1(x)$ and by $x = 0, L$, is by mapping this undulated region onto a rectangular one defined by $\widetilde{y}_1 = 1$, $\widetilde{y}_0 = 0$, and $x = 0, L$, where L is the length of the channel. For arbitrary functions $y_0(x)$ and $y_1(x)$, the map $(x, y) \rightarrow (x, \widetilde{y})$ is obtained with the change of variables,

$$\widetilde{y} = \frac{y - y_0}{y_1 - y_0} \qquad (3.2)$$

Under this map, the diffusion term in Eq. (2.20) transforms as [103]:

$$\nabla^2 u \rightarrow \partial_{xx}^2 \widetilde{u} + F(x)\partial_{\widetilde{y}\widetilde{y}}^2 \widetilde{u} + G(x)\partial_{x\widetilde{y}}^2 \widetilde{u} + H(x)\partial_{\widetilde{y}}\widetilde{u} , \qquad (3.3)$$

where

$$F(x) = \frac{1 + (\Delta_x \widetilde{y} + y_{0x})^2}{\Delta^2} \tag{3.4}$$

$$G(x) = -2\frac{\Delta_x \widetilde{y} + y_{0x}}{\Delta} \tag{3.5}$$

$$H(x) = \frac{\widetilde{y}\left(2\Delta_x^2 - \Delta\Delta_{xx}\right) - \Delta y_{0xx} + 2\Delta_x y_{0x}}{\Delta^2} \tag{3.6}$$

$$\Delta(x) = y_1(x) - y_0(x) \tag{3.7}$$

$$\Delta_x(x) = \frac{d}{dx}\Delta(x) \tag{3.8}$$

$$\Delta_{xx}(x) = \frac{d^2}{dx^2}\Delta x(x) \tag{3.9}$$

$$y_{0,1x} = \frac{d}{dx}y_{0,1} \tag{3.10}$$

$$y_{0,1xx} = \frac{d^2}{dx^2}y_{0,1} \tag{3.11}$$

Note that, if the channel has constant width, $\Delta_x = \Delta_{xx} = 0$. $F(x)$, $G(x)$ and $H(x)$ are periodic functions reflecting the undulations of the boundaries via modulations measured by the product kd. In the limit $kd \to 0$ (straight channel), Eq.(3.3) becomes the standard Laplacian.

Wave trains are generated by stimulating the medium at the left end $x = 0$ of the channel by driving u periodically in time above and below the excitability threshold. The opposite end of the channel ($x = L$) is a no-flux boundary. During the simulations we have mainly varied the forcing parameters λ_p and d, for several wave train periods and channel widths. After a transient, the fields u and v converge to a configuration of propagating fronts that repeats itself periodically in time in synchrony with the wave generator at $x = 0$.

In the following discussion, we denote by x_n and a_n the longitudinal position and maximum of u at the channel axis, respectively, for the n*th* front. A snapshot of a segment of the channel is plot in the upper part of Fig. 3.2 where different gray levels are proportional to the value of u, maxima of which are plotted in the lower part of Fig. 3.2.

For comparison, in a straight channel ($d = 0$) of a width s the asymptotic configuration consists of equally spaced wave fronts propagating with velocity $c = \lambda/T$, where λ is the spacing between successive fronts and T is the forcing period. This velocity increases with the channel width [77]
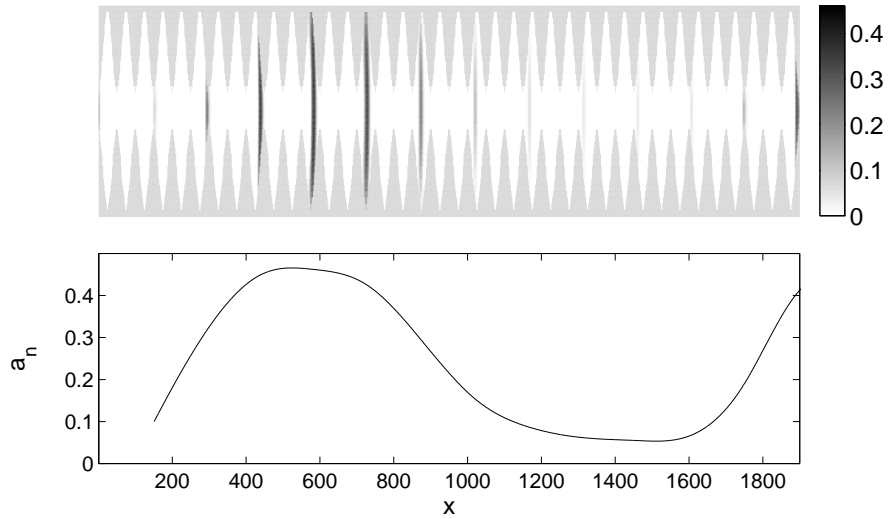
Figure 3.2: In the upper panel, the white area limited by gray undulated boundaries is the excitable region where fronts originated at the left end propagate. The transverse features are the fronts traveling to the right. Darker fronts have a larger value of u, as indicated in the colorbar. The lower panel displays the envelope of the maximum amplitude of the fronts. Parameters: $\lambda_p = 50$, $s = 1.1$ s.u., and $d = 1.9$ s.u.
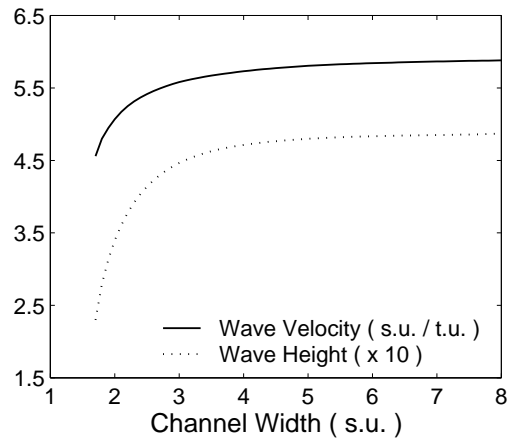
Figure 3.3: Wave train velocity and wave height (multiplied by a factor of 10) in straight channels of different widths. There is a critical value, $s_c = 1.65$ s.u., below which propagation becomes impossible. $T = 5$ t.u.
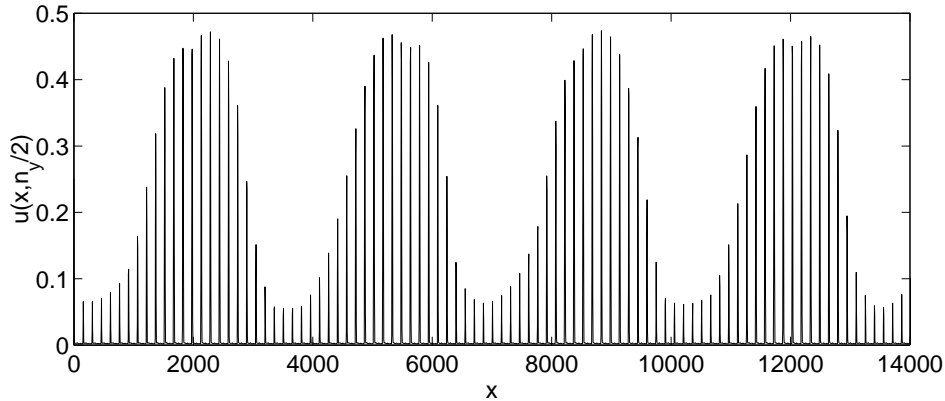
Figure 3.4: Profile of the variable u along the middle line of a sinusoidal channel of $\lambda_p = 50$, $s = 1.1$ s.u., $d = 4$ s.u., and $T = 5$ t.u.

above critical value s_c. For narrower channels the fronts cannot propagate since the unexcited boundary layers fill-up the whole width of the channel. In Fig. 3.3 we plot the train velocity and the maximum amplitude of the wave fronts as a function of the width of the straight channel.

3.2.2 Results

In modulated domains with $d \neq 0$ a wide range of new spatial configurations emerge, which are incommensurated with the boundaries. Typically, both the spacing and the amplitude of the fronts become spatially quasiperiodic. This can be seen in Fig. 3.4, where the profile of the variable u at time $t = 644$ t.u. is plotted along the center of the channel. The mean wavelength of this train is about 150 grid points for a stimulating period of $T = 5$ t.u. The observed pattern in this figure occurs in a modulated channel of $\lambda_p = 50$ grid points.

According to the strength of the spatial forcing $kd \propto d/\lambda_p$ we distinguish strong and weak modulations. We shall describe, as an illustration, in more detail, the cases $\lambda_p = 50$ and $\lambda_p = 1000$.

The results for strong modulation are shown in Figs. 3.5, 3.6 and 3.7 corresponding to different minimum channel separation s. For each figure, the amplitude of the boundary undulation d increases from top to bottom. The quasiperiodic behavior of the pulse height in the first column, becomes evident as d increases. The second column in Fig. 3.5 shows also the maximum a_n of each front as a function of its position
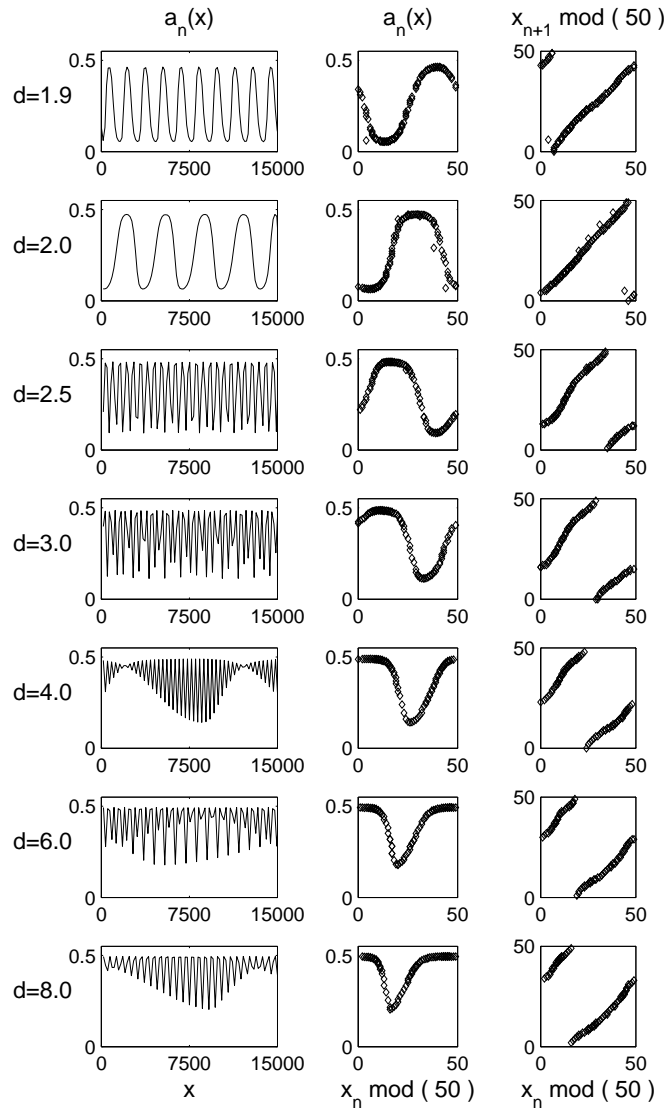
Figure 3.5: Numerical results obtained with the Oregonator model for strong forcing. First column: Maximum height of each front within the train, as a function of position x. Second column: Same as before but with position x folded modulo $\lambda_p = 50$. Third column: Return map of the front positions modulo λ_p. Each row is for a different amplitude d (in s.u.). Parameters: $\lambda_p = 50$, $T = 5$ t.u., $s = 1.1$ s.u.. Note that channel length $L = 15000$ is much larger than that in Fig. 3.2.
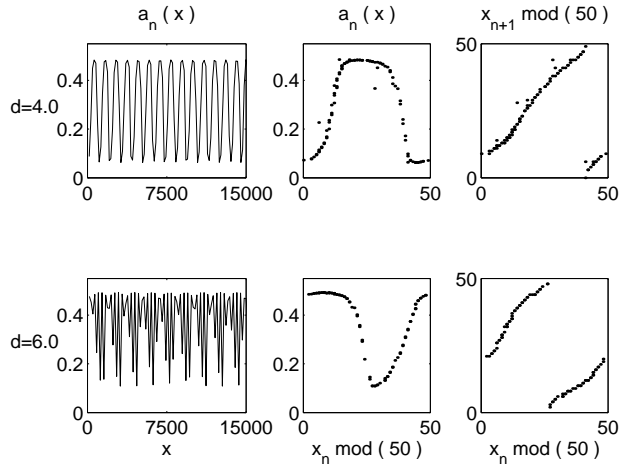
Figure 3.6: The same as in Fig. 3.5 but $s = 0.95$ s.u.
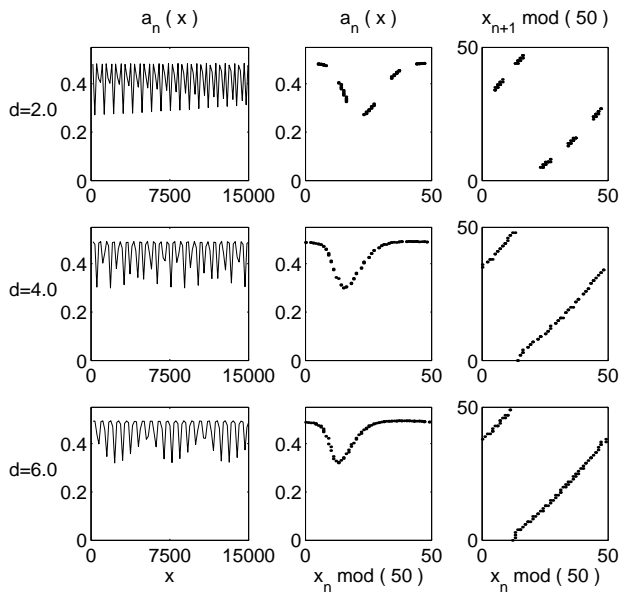
Figure 3.7: The same as in Fig. 3.5 but $s = 1.5$ s.u.
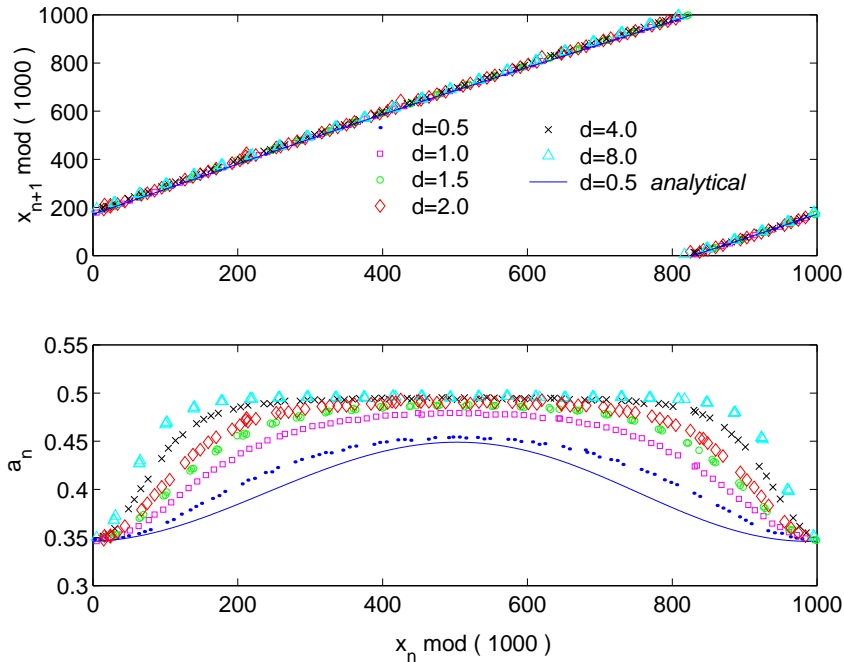
Figure 3.8: Weak forcing behavior at $\lambda_p = 1000$ and $s = 2$ s.u. Above: Return map of the front positions modulo λ_p. Below: Maximum height of each front as a function of the front position modulo λ_p. Solid lines are from Eqs. (3.17) and (3.19).

modulo, λ_p. This plot provides information about the distribution of the front height maxima relative to the elementary unit of the channel. Notice that the fronts do not always reach their minimal height at the narrowest channel sections ($x = m\lambda_p$) as one might expect from the behavior in straight channels depicted in Fig. 3.2. Moreover, the fronts can now propagate even when the channel is narrower ($s = 1.1$ s.u.) in some places than the minimum width $s_c = 1.65$ s.u. that allows propagation in straight channels. The last column in Fig. 3.5 displays the *return maps* of the (n+1)*th* front position x_{n+1} (relative to the unit channel cell) as a function of the position x_n of the previous front. The shapes of the curves are similar to the *circle maps* (see Appendix C) describing the temporal dynamics of periodically forced self-oscillators, thus confirming our aim when constructing the system: the analogy between spatial behavior along a longitudinal coordinate in a channeled domain, and time evolution in dynamical systems. The analogy suggests that our system should exhibit the same richness of spatial behaviors as present in time evolutions of the
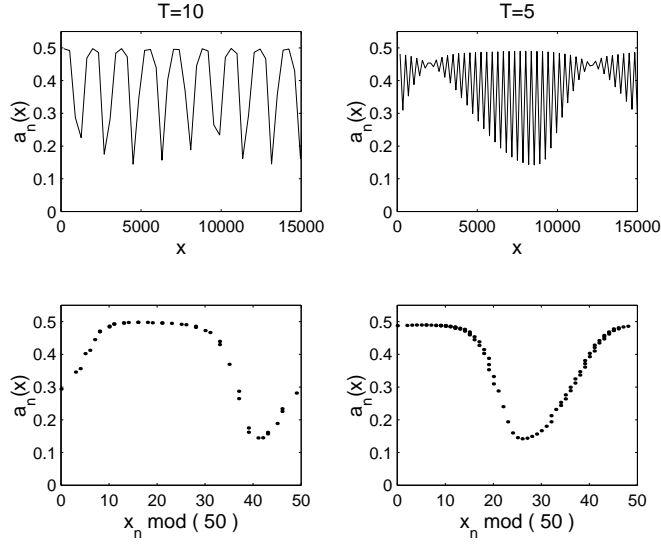
Figure 3.9: Comparison of the resulting patterns for different periods of the wave train propagating in identically modulated channels. Left: $T = 10$ t.u., the maximum height of each front $a_n(x)$ along the channel (above) and within one modulation wavelength of the channel (below). Right: the same as in left side but $T = 5$ t.u. Rest of parameters: $\lambda_p = 50$, $d = 4$ s.u., $s = 1.1$ s.u. The system is shown at $t = 644$ t.u. corresponding to a stationary configuration which persists after the initial transient.

circle map.

The weak forcing case is illustrated in Fig. 3.8. As in the case of circle maps for very weak forcing, the front-positions return map shows a very small deviation from linearity with the given parameter values. This approximate linearity implies that the front train wavelength is nearly constant and the influence of the channel walls is negligible. This influence on the front heights is, however, more pronounced. Minima of front height are situated at the narrowest channel sections, in agreement with Fig. 3.3, while the maxima saturate for large enough d.

The effect of varying the period of wave initiation at $x = 0$ on the resulting spatial configuration is illustrated in Fig. 3.9. The maximum wave height along the channel is shown for two different periods, $T = 5$ and $T = 10$ t.u. The parameters of the spatial forcing are the same in both cases.

3.2.3   Theoretical Analysis

We shall now derive an analytical expression for the return maps of successive wave fronts positions and maximum heights. The approach is based on rather general arguments, not explicitly dependent on the particular model Eqs. (2.20)-(2.21). In case of weak forcing we assume that the front velocity approaches quasiadiabatically the velocity $c(\Delta)$ of the wave in an uniform channel of the same width Δ as the local width of the undulated channel Fig. 3.3.

   This is confirmed in Fig. 3.10 where the maximum heights of the fronts at position x_n are plotted against the corresponding channel width at that position and superimposed to the case of a straight channel (curve extracted from Fig. 3.3). Thus, the velocity of the n*th* front is

$$\dot{x}_n(t) = c(\Delta(x_n)) \tag{3.12}$$

In our channel $\Delta(x) = \Delta_0 - \Delta_1 \cos(kx)$ with $\Delta_0 = s + d$ and $\Delta_1 =$
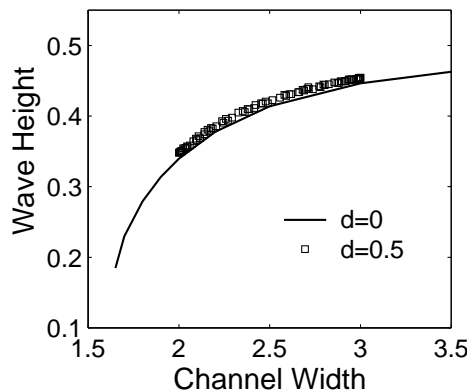
Figure 3.10: Maximum heights of the fronts at position x_n as a function of the channel width of a straight channel (solid line) and of a modulated channel ($\square$). $\lambda_p = 1000$ and $s = 2$ s.u.

d. In order to proceed analytically an approximation for $c(\Delta)$ should be introduced. For small d's the width variation is also small and $c(\Delta)$ can be replaced by a linear fit $a + b\Delta$ of an appropriate range of data in Fig. 3.3. Hence, $c(\Delta(x_n)) \approx c_0 - c_1 \cos(kx_n)$ where $c_0 = a + b\Delta_0$ and $c_1 = b\Delta_1$. Eq. (3.12) can now be integrated during one period T of the front generator,

$$\int_{x_n(0)}^{x_n(T)} \frac{dx_n}{c_0 - c_1 \cos(kx_n)} = T \tag{3.13}$$

to obtain:

$$\frac{2}{k\sqrt{c_0^2 - c_1^2}} \left[\arctan f(x_n) \right]_{x_n(0)}^{x_{n+1}(0)} = T \tag{3.14}$$

with

$$z_n = f(x_n) = \sqrt{\frac{c_0 + c_1}{c_0 - c_1}} \tan\left(\frac{kx_n}{2}\right) \tag{3.15}$$

In Eq. (3.14) we use the time periodicity of the wave train to write $x_n(T) = x_{n+1}(0)$. This is the crucial step to convert the time-differential equation (3.12) into a map for space positions.
Defining $\varphi = \arctan z$ and $\triangle = 0.5\, kT\sqrt{c_0^2 - c_1^2}$ we have $\triangle = \varphi_{n+1} - \varphi_n$, and the return map for the variable z is

$$z_{n+1} = g(z_n) = \frac{z_n + \tan\triangle}{1 - \tan\triangle \cdot z_n} \tag{3.16}$$

In terms of the front position x we finally have:

$$x_{n+1} = f^{-1}\left(g(f(x_n))\right) \tag{3.17}$$

For the maximum height of the wave fronts, the same adiabatic assumption leads to $a_n = h\left(\Delta_0 - \Delta_1 \cos(kx_n)\right)$, with $h(\Delta)$ being the maximum height of the fronts in a straight channel of width Δ. A further step in the qualitative description of the observed positional mismatch between the minimal-height of the fronts and the narrowest sections of the channel is to consider a short adaptation time τ_a of the front characteristics to the local width:

$$\dot{a}_n(t) = \frac{1}{\tau_a}\left(h(\Delta(x_n)) - a_n\right) \tag{3.18}$$

Linearly fitting the data from Fig. 3.3 in the range $(s, s + 2d)$ we have $h(\Delta) \approx a' + b'\Delta$ for small d. Then, $h(\Delta(x)) \approx h_0 - h_1 \cos(kx)$, with $h_0 = a' + b'\Delta_0$, and $h_1 = b'\Delta_1$.

Integrating Eq. (3.18) for small d and $kc_0\tau_a \ll 1$ so that we can set $x_n(t) = x_n(0) + c_0 t + \mathcal{O}(d)$, we get a relationship linking the wave front heights and positions,

$$a_{n+1} = h_0 - \frac{h_1}{\sqrt{1 + \tau_a^2 k^2 c_0^2}} \sin\left(k(x_n + c_0 T) + \theta\right) \tag{3.19}$$

Here $\theta = \arccos\left[1/\sqrt{1 + (\tau_a c_0 k)^2}\right]$ describes the displacement of the minimal heights from the narrowest sections.

Since the derivation of Eqs. (3.17) and (3.19) is formally valid only in the weak forcing limit we first contrast the theory against the numerical
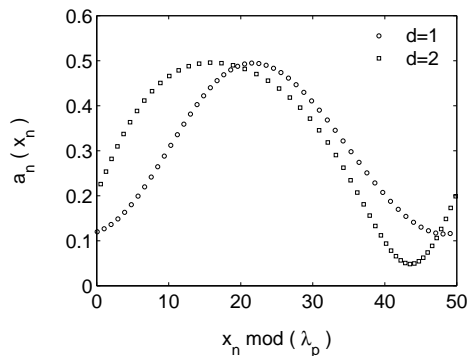
Figure 3.11: Change in the shape of $a_n(x_n)$ from Eq. (3.19) by increasing d (s.u.) beyond the weak forcing limit. $\tau_a = 0.01$, $\lambda_p = 50$, $s = 1.1$ s.u.

data in Fig. 3.8 for $d = 0.5$, to confirm the good agreement[2]. More detailed numerical explorations reassure us that both adiabaticity and small d approximations are justified and that the small deviations in Fig. 3.8 are only due to the linear approximation on $c(\Delta)$. Moreover, a systematic d expansion in Eq. (3.17) leads precisely to a circle map supporting the observation that this model is relevant to the description of our boundary-induced patterns in a given limit (Appendix C). Finally, while the agreement between the theory and the numerics becomes less precise as the forcing increases, the theory still describes qualitative features of the strong forcing regime. As an example, Fig. 3.11 shows how the maxima and minima of $a_n(x_n)$ shift as d is increased.

3.2.4 Conclusions

In summary, we have shown that undulated channels induce nontrivial longitudinal effects on propagating periodic wave trains. In particular, the trains assume quasiperiodic spatial configurations that cannot be simply deduced from the shape of the channel. These structures can be described in terms of spatial return maps that are very similar to the circle maps whose iteration describe the temporal dynamics of forced oscillators. This similarity allows one to speculate about the existence of even more complex configurations representing the spatial realizations of the chaotic regimes of these maps. The phenomenon reported here should be experimentally observable in the photosensitive Belousov-Zhabotinsky reaction with proper lighting conditions at the boundaries.

---

[2] Fittings to Fig. 3.8 lead to $c_0 = 5.37$, $c_1 = 0.25$, $h_0 = 0.40$, $h_1 = 0.052$, and $\tau_a = 0.1$.

3.3 Sustained Propagation in a Periodically Modulated Subexcitable Medium

In this Section, we study the effects of spatially homogeneous, periodic modulations of excitability on wave propagation in a subexcitable medium.

Propagation of an excitation depends upon its spatial properties and the excitability of the medium. It is possible to determine the limiting excitability below which the medium is nonexcitable, and except for transients does not support continuous propagation of autowaves regardless of the extent of initial stimulation. For the excitable medium there is a separatrix in terms of excitability and extent of initial excitation that delineates for each excitability the initial conditions leading to continuous propagation from those that disappear after initial transient. Systems in the vicinity of this separatrix are sometimes called subexcitable since depending on small changes in size and shape of the initial conditions the same medium can exhibit qualitatively different fate of the initiated wave.

The term *subexcitable* has been used through the literature by authors who meant to address situations which here we defined as unexcitable [106, 5]. Most of the work concerned unfavorable conditions for wave or signal transmission has used external noise sources to enhance or maintain such propagation [11, 8, 107, 106]. Here we address a method of controlling wave propagation by periodically forcing the excitability of a subexcitable medium [108]. In Section 3.3.1 we present experimental examples of modulation supported wave propagation and corroborate these results with numerical studies. We also offer a simple kinematic analysis in Section 3.3.2.

3.3.1 Experimental and Numerical Results

The excitability of the medium was controlled by varying the light intensity as it has been described in Section 2.3. In order to maintain the chemical medium in a particular subexcitable state, the light intensity was set to a reference value, I_0. A modulation of the excitability was then introduced by varying the light intensity as a square wave, with values $I_0 \pm A/2$ alternating with period T. This was accomplished by projecting computer generated images similar to the one shown in Fig. 3.12 onto the gel medium. Waves were generated in the darker region on the left and allowed to propagate to the region on the right, the illumination of which has been periodically varied. The initial length of the wave front entering the forced area was determined by the size of the connecting part between these both regions.

Typical results are shown in Fig. 3.13. Panel (a) shows overlaid images
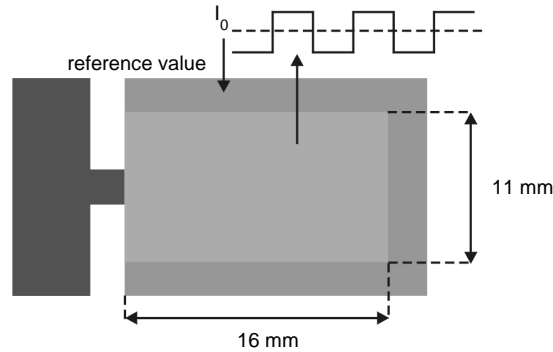
Figure 3.12: Pattern projected onto the gel: wave fronts are created at the dark leftmost part; wave propagation is investigated in the lighter region on the right; the bridge connects the two regions and determines the initial length of the wave front.

taken at equal time intervals of a wave propagating in the subexcitable medium (corresponding to constant illumination at the reference intensity I_0). We see the contraction and collapse of the wave segment due to a negative tangential component of the velocity at the free ends of the wave. Panel (b) shows that the propagation distance of the wave is increased with the application of a periodic modulation of the light intensity around I_0. With longer modulation periods, the wave propagation is greatly enhanced, as shown in panel (c). Sustained wave propagation is exhibited for certain periods and amplitudes of light intensity modulation
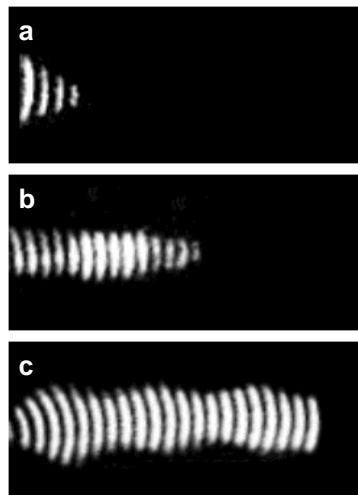
Figure 3.13: Overlay of images taken every 20 s of a wave propagating in a subexcitable light-sensitive BZ medium with periodic modulation of light intensity: $I = I_0 \pm A/2$, $I_0 = 3.87$ mW/cm^2, and $A = 0.22$ mW/cm^2. (a) wave evolution with no modulation, (b) partial support of wave propagation with a modulation period of $T = 66$ s, and (c) sustained propagation with $T = 133$ s. Reagent concentrations: 0.27 M NaBrO$_3$, 0.05 M malonic acid, 0.2 M H$_2$SO$_4$, 0.15 M bromomalonic acid, 2 mM Ru(bpy)$_3^{2+}$. The medium domain is 1.59 cm $\times$ 0.74 cm.
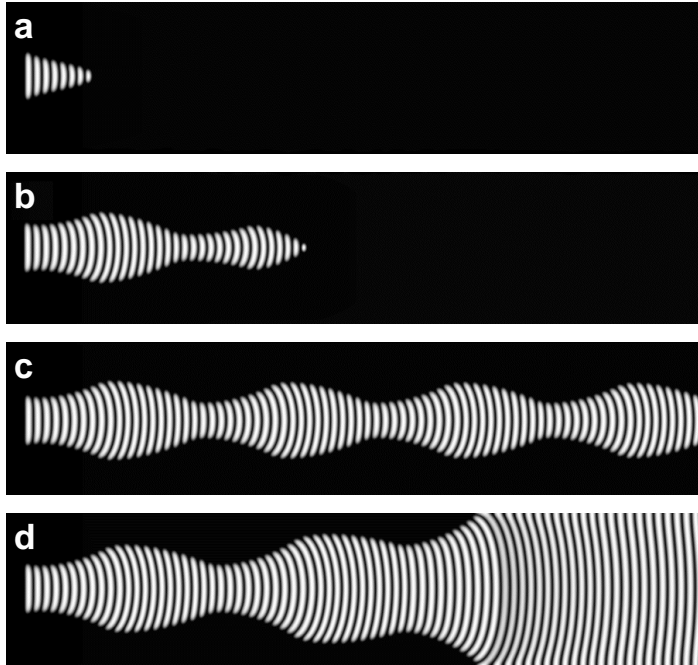
Figure 3.14: Calculated wave behavior using the Oregonator model of the photosensitive BZ reaction, Eqs. (2.20)-(2.21). Excitability is modulated periodically through $\phi = \phi_0 \pm A/2$, where $\phi_0 = 0.0766$ and $A = 0.004$, as a square wave with period T. (a) wave evolution with no modulation, (b) partial support of wave propagation with a modulation period $T = 9$, (c) sustained propagation with $T = 10$, and (d) expanding wave with $T = 11$. Zero flux boundary conditions were used in an array of 900×200 points (time step 10^{-3} and grid point spacing 0.15). The parameters were $\varepsilon = 0.03$, $f = 1.4$, $q = 0.002$, $D_u = 1$, and $D_v = 0$; the initial length of the wave segment was the same in all calculations (6.8 s.u.).

that generate excitabilities above and below the subexcitable reference state on an appropriate time scale. Numerical simulations with the two-variable Oregonator model modified to include the photosensitivity of the BZ reaction (Section 2.4), provides insights into the support of wave propagation by periodic modulation of excitability. Figure 3.14 shows the evolution of wave fronts calculated with the Oregonator model for different values of the modulation period T and a constant amplitude A. Wave propagation in the subexcitable medium without periodic modulation is shown in panel (a). With T less than the critical value, the temporal modulation of excitability temporarily prolongs the life of the wave front, as shown in panel (b), but does not prevent its eventual collapse. Sustained
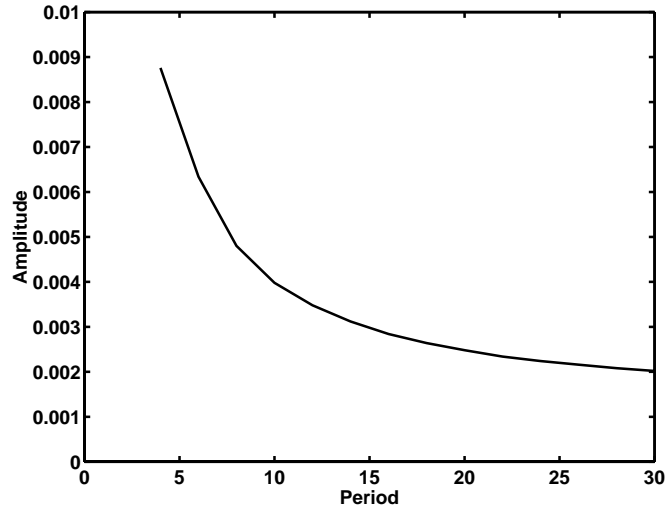
Figure 3.15: Wave behavior of the Oregonator model for different values of modulation period and amplitude. Parameter values below the line correspond to decaying wave fronts; parameter values above the line correspond to expanding wave fronts. The boundary corresponds to sustained propagation of wave fronts with periodically modulated length. System parameters and numerical integration are the same as in Fig. 3.14.

wave propagation occurs at the critical period T_c, shown in panel (c), where the wave front displays a periodic modulation in length corresponding to the periodic modulation in excitability. For periods longer than T_c, the wave front grows until it reaches the boundary of the medium, panel (d). Once pinned at the boundaries, the wave takes on the features of an unbounded planar wave, which propagates indefinitely for these conditions.

The effects of periodic excitability modulation on wave propagation are summarized in the phase diagram shown in Fig. 3.15, which shows the qualitative asymptotic behavior as a function of the forcing period and amplitude. Along the critical line, a balance between the rates of contraction and expansion gives rise to sustained wave propagation. Below this line, the modulation is not sufficient to prevent wave collapse, although wave propagation is increasingly enhanced for periods and amplitudes approaching the line. Above the critical line, the excitability modulation supports propagation, and the wave segment increases in length as it propagates. In our experiments and model calculations, this expansion always resulted in an extension of the wave to the boundaries of the rectangular reaction domain.
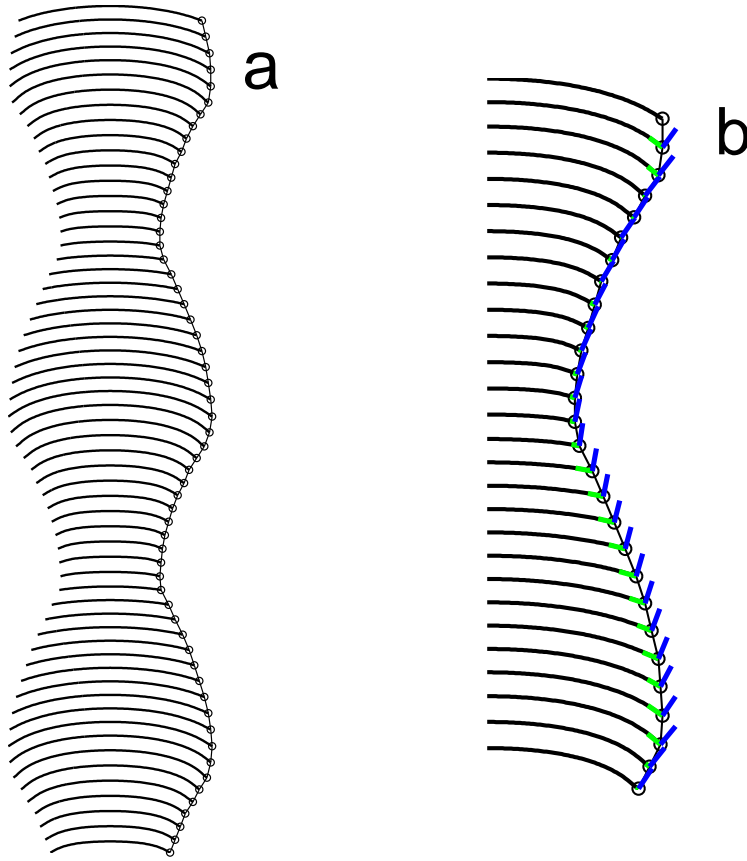
Figure 3.16: (a) Contours of the excited fronts of panel (c) of Fig. 3.14 together with circles at the right side marking the end points. (b) Enlargement of (a) with added tangential and normal velocity vectors.

We follow the motion of one of the end points of the front (since it is symmetrical). The end point is located on the contour of the excited region for panel (c) of Fig. 3.14. Figure 3.16(a) shows those contours with the end points marked with a circle. A blow-up of this figure is shown in Fig. 3.16(b) where the tangential and normal velocity vectors are also plotted at the end points. Note how the tangential component becomes negligible during wave expansion and negative when contraction.

Graphs of the temporal evolution of the velocity (Fig. 3.17(a)) both at the middle point of the wave front, v_m, and at the end point, v_t and v_n, show a periodical modulation with the forcing period. Whereas v_m
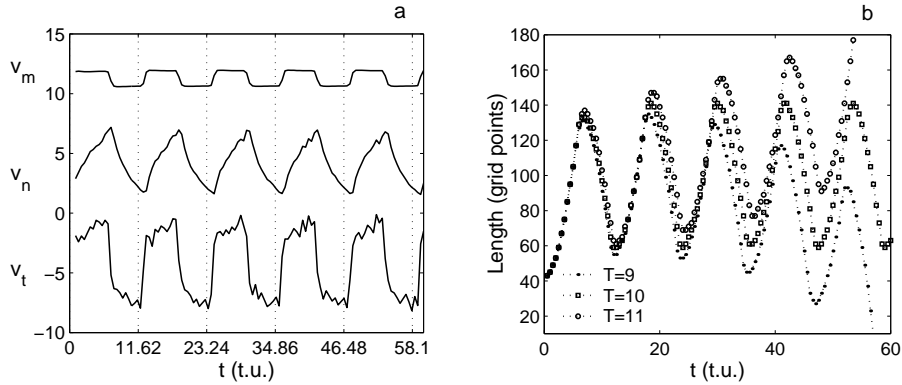
Figure 3.17: (a) Temporal variations of the normal velocity at the middle (v_m) of the wave front and of the normal (v_n) and tangential (v_t) velocities at the end point for the case of panel (c) in Fig. 3.14. (b) Temporal evolution of the size of the wave fronts of panels (b), (c) and (d) of Fig. 3.14.

and v_t present a clear square pulse shape synchronized with the external modulation, v_n behaves similarly to wave front in Fig. 3.17(b). Its behavior is a composition of exponential growth and decay periods.

3.3.2   Analytical Approach

Chemical wave propagation in a medium with modulated excitability can be analyzed using a simple kinematic model for the motion of a curved wave front with free ends (see Appendix A). The wave is represented by a single oriented curve with two end points. Each small segment of the curve moves in its normal direction with velocity v_n, and the end points have a tangential velocity component v_t. We consider an expression for the total length ℓ of the curve, evolving in time for homogeneous conditions,

$$\frac{d\ell}{dt} = \int_0^\ell k\, v_n\, d\ell \; + \; 2v_t \tag{3.20}$$

The first term in Eq. 3.20 represents the increase in length due to the radial expansion of the curve, whereas the second term corresponds to the contraction of the curve at its ends. For critical values of the parameters, these two processes compensate each other to yield a propagating wave with a constant shape. Thus, integrating Eq. 3.20 under the assumption $k = const.$, results in the following temporal variation for the total length,

$$\ell(t) = (\,\ell_0 - \ell_c\,)\, e^{\frac{t}{\tau}} \; + \; \ell_c \tag{3.21}$$
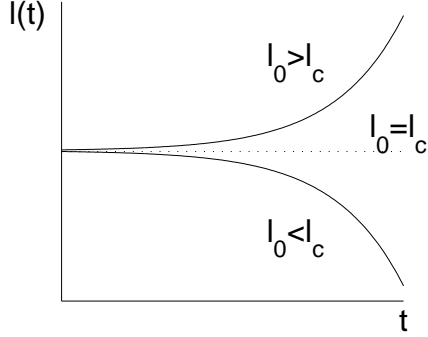
Figure 3.18: Temporal evolution given by Eq. (3.21) for different initial lengths ℓ_0

where $\ell_0 = \ell(0)$ is the initial length, $\tau = (kv_n)^{-1}$ is the characteristic time, and $\ell_c = -2v_t\tau$ is the critical length such that when $\ell_0 > \ell_c$, $\ell(t) \to \infty$ and when $\ell_0 < \ell_c$, $\ell(t) \to 0$ [3].

This solution is, thus, unstable, with any deviation from the critical length l_c respect to l_0, leading to an exponential divergence from this length with a characteristic time τ as shown in Fig. 3.18.

Observations suggest that modulation of excitability results in two effectively separate modes of wave evolution, each approximately described by its own set of empirical kinematic parameters that can be measured from images of propagating wave fronts (Fig. 3.16). These parameters define two critical lengths $\ell_c^- < \ell_c^+$ and the corresponding time constants τ^- and τ^+. The solution for the modulated medium can, thus be written as a piecewise function:

$$\ell = \begin{cases} (\ell_0 - l_c^-) \, e^{\frac{t}{\tau^-}} + \ell_c^- & 0 < t \leq \frac{T}{2} \\ (\ell(\frac{T}{2}) - \ell_c^+) \, e^{(t-\frac{T}{2})\frac{1}{\tau^+}} + \ell_c^+ & \frac{T}{2} < t \leq T \end{cases}$$

where t is taken modulo T. Since the length changes periodically in time, the length at the end of the period must return to its initial value, $\ell(T) = \ell(0)$, which leads to the following relation between the initial condition l_0 and the forcing parameters:

$$\ell_0 = \frac{\ell_c^- \, (1 - e^{\frac{T}{2\tau^-}}) \, e^{\frac{T}{2\tau^+}} + \ell_c^+ \, (1 - e^{\frac{T}{2\tau^+}})}{1 - e^{\frac{T}{2}(\frac{1}{\tau^-} + \frac{1}{\tau^+})}} \tag{3.22}$$

---

[3] It should be noted that exponential trends are also observed experimentally during one half of the modulation (see Fig. 3.16)
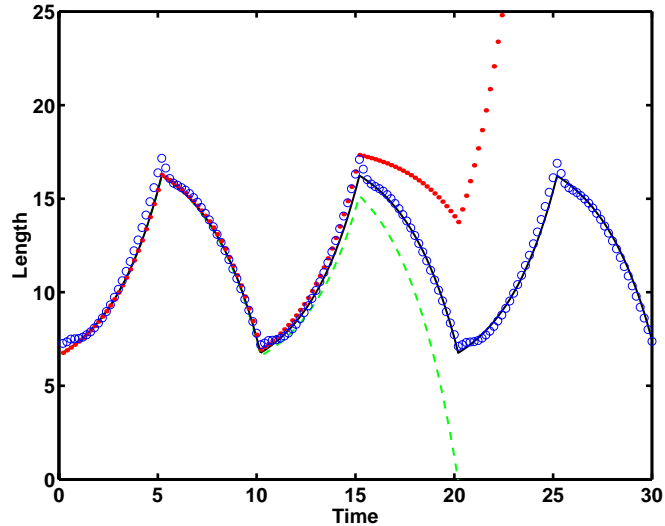
Figure 3.19: Length of expanding (dotted line), sustained (solid line), and contracting (dashed line) waves according to Eq. 3.20. Modulation periods are $T = 9.985$, 10.000, and 10.015, respectively, with 10.000 being the critical period for the initial half-length $\ell_0 = 6.66$ s.u. Parameters are $\ell_c^- = 5$, $\ell_c^+ = 18$, $\tau^+ = \tau^- = 2.6$. Small circles correspond to length of the wave calculated with the Oregonator model with the same parameters as in Fig. 3.14, panel (c).

Figure 3.19 shows the evolution of the front length given by Eq. 3.22. The parameters are chosen to approximate the wave behavior in Fig. 3.14. The three trajectories correspond to three different modulation periods. The modulation with the critical period T_c, found from Eq. 3.22 for this particular initial length, results in a periodic solution. The modulation with a lower period, $T < T_c$, produces a decaying solution; the modulation with a higher period, $T > T_c$, produces an unconstrained growth in the length of the wave.

The support of wave propagation in a subexcitable medium by excitability modulation can be understood by considering the wave segment evolution during each half of the driving period. During the half where the medium is more excitable, the wave develops a curved shape and increases in length; during the half where the medium is less excitable, the wave shrinks and becomes quasiplanar. Both the amplitude and period of the modulation, as well as the initial length and curvature of the wave segment, determine which process dominates and, hence, whether the wave shrinks and disappears or grows and continues to propagate. When these processes

are balanced, sustained propagation is exhibited, as shown in panels (c) of Figs. 3.13 and 3.14 respectively.

We should note, however, that although this approach yields a description in good agreement with the phenomenology, it relays on rather arbitrary definition of the 'front' and its 'endpoint'.

A more satisfactory approach can be developed starting with a shape of a wave segment propagating with a constant size in a medium of just sufficient excitability. In this case it is possible to define a meaningful contour of the reaction zone. The point where the contour becomes tangential to the direction of the wave translation provides an unambiguous definition of the endpoint. Considering how the shape of such segment changes in response to a small perturbation of the medium excitability, one can arrive to the exponential divergence law similar to the one presented above.

3.3.3 Conclusions

In summary, we have found that periodic modulation of excitability around a subexcitable state may give rise to sustained wave propagation, depending on the forcing parameters and initial conditions. For critical values of these constraints, the sustained propagation assumes a form where the length of the wave varies periodically with the period of the external modulation. The propagation is further enhanced by adjusting the forcing parameters such that the wave front grows in length.

It should be noted that both experiments and numerical simulations have been carried out by using a square-shaped periodical function. Similar results can be obtained with a smoother periodical modulation such a sinusoidal one and a continuous analytical model can be derived showing analogous trends as the ones displayed by the piecewise model here introduced.

Chapter 4

Wave Propagation under Disorder

Abstract. *The effect of **quenched disorder** on the propagation of autowaves in excitable media is studied both experimentally and numerically in relation with the light-sensitive Belousov-Zhabotinsky reaction. Spatial disorder is introduced through a random distribution with two different levels of light intensity. In one dimensional case the (time-averaged) wave speed is smaller than the corresponding to a homogeneous medium with the mean excitability. On the contrary, in two dimensional medium the velocity increases. The results are interpreted using kinematic and scaling arguments. In particular, for $d = 2$ we verify a theoretical prediction of a power-law dependence for the relative change of the propagation speed on the disorder amplitude. In a complementary study, the behavior of chemical waves advancing through a disordered excitable medium is investigated in terms of the percolation theory. By controlling the number of sites with a given illumination, different percolation thresholds for propagation are observed. The influence of **spatiotemporal colored disorder** on wave train propagation in nonexcitable media is also investigated. This study has been performed within the framework of the Oregonator model in terms of the characteristic noise parameters. Some features seen in single front propagation, for instance, noise induced propagation improvement for an optimal level of the noise intensity, are also found for periodic wave trains. However, we also observe novel phenomena, such as an enhancement of propagation for correlation times of the noise comparable to the period of the wave train.*

4.1 Wave Propagation under a Quenched Disorder

4.1.1 Introduction

Propagation of excitation waves in inhomogeneous media has been studied from different points of view. One such approach considers the interaction of waves and inert obstacles, which is thought to be relevant to cardiac

fibrillation. Excitation waves may be disrupted by irregularities in the heart muscle [109, 110, 111] and the planar front broken [112, 55, 56]). The effect of fluctuations on nucleation and propagation of waves has also been a subject of extensive research [113, 114, 10, 83]. Earlier studies demonstrated many ingenious ways to introduce fluctuations into chemically reactive systems. In one experiment carried out by De Kepper and Horsthemke [115] the noise generator has been a container full of polystyrene balls shaken by a turbulent flux of air. After crossing this device, stochastically modulated light has been used to produce transitions in a chemical reaction. In a different experiment performed by Maselko and Showalter [116] catalyst coated resin beads in a BZ medium served as nucleation sites for the wavefronts.

Fluctuations allow systems to explore new regions around those present in the deterministic scenario. Noise is ubiquitous in any realistic situation and it is natural that its effects on wave front propagation had been addressed in many papers during the last years [117, 118, 119, 120, 121, 122, 123, 124, 14, 15]. Different aspects of front propagation have been considered, especially the modification of the front velocity and the spreading of the front due to fluctuations [117, 122, 123] and with self-affine scaling behavior characterized by a roughening exponent [124, 14, 15]. The scaling phenomenology exhibited by stochastically growing interfaces has been analyzed from different points of view, namely during the time regime corresponding to transient development [15, 125] and during the time that follows transient relaxation where the overall propagation rate of the steady propagation of the interface is characterized [14].

The role of fluctuations has been modeled using both additive and multiplicative noise sources. Both bistable or excitable wave front motion in one and two dimensional media have been considered. Front roughness induced by fluctuations has received special attention [126, 127]. Particularly there have been analyzed the quenched versions [128, 125] of either the Edwards-Wilkinson (EW) [129] or the Kardar-Parisi-Zhang equations [15] as they apply to kinetic roughening induced by time-independent disorder. In this section we aim at studying, both experimentally and numerically, the effects on the propagation of autowaves originated by introducing time independent random spatial fluctuations in the medium excitability [130, 131]. Specifically, rather than characterizing the front roughening we are interested in how the propagation velocity is affected by the amplitude of the disorder depending on the dimensionality of the noise. This question is elucidated in Section 4.1.2.

Wave front propagation through a lattice with random excitability affords a chance to mimic percolation phenomena experimentally using autowaves. Percolation theory allows to interpret many physical experiments where connectivity plays a fundamental role (for a review, see Refs. [132, 133]). Representative examples are electrical conductivity in disordered semiconductors [134, 135], percolation at the superconducting transition in Y–Ba–Cu–O thin films [136], two–dimensional percolation in cluster deposition [137] and fingering phenomena [138].

Considered in its original version, percolation is a *static* geometric tool relating accessibility properties within a lattice and eventual crossing of it to the occupancy probability of its constituent sites. In this sense, percolation theory establishes the existence of a threshold or critical value p_c, below which only finite (non connecting) clusters are present, whereas an infinitely connected path is generated at p_c. In addition to the examples cited above, there are well-known situations, such as fluid displacement in oil fields or forest fire spreading, where percolation ideas, even at their most simple and intuitive level, have been fruitfully used [132]. However, as far as we know percolation concepts have never been systematically addressed before in connection to autowave propagation in chemical media. This is quite surprising if one considers the apparent similarities between some of the these situations and the invasion of a non-excited medium by an excited front.

In Section 4.1.3, we study both experimentally and numerically the propagation of a wave front in a medium consisting of clusters with two different values of excitability [139]. Waves could only propagate through one kind of clusters, which reminds the situation found in experiments of disordered semiconductors [134, 135]. Characteristic times are studied as a function of the relative excitability levels and interpretations are given in terms of the classical percolation theory.

4.1.2 Random Dichotomous Disorder. Distorting Phenomena

4.1.2.a 1D Disorder

In order to investigate the effect of spatial disorder in one dimension, the experiment shown in Fig. 4.1 has been conducted. We use a photosensitive BZ medium divided into two halves - one homogeneous and another one inhomogeneous. Between them, the medium is nonexcitable because of the high light intensity. The spatial disorder on the right part is described
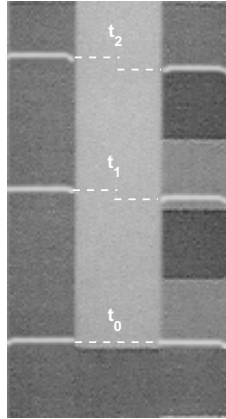
Figure 4.1: Propagating wave front on light sensitive media consisting of a left-side homogeneous and a right-side quasi-one-dimensional inhomogeneous medium with a brighter stripe between them where fronts can not propagate. An initial flat front splits into two that were represented at three different times. The front which propagates through the inhomogeneous part undergoes an appreciable delay with respect to the other one. Stripe size, $\ell = 1.1$ cm. Reagents concentrations: 0.71 mM $Ru(bpy)_3^{+2}$, 0.18 M KBr, 0.33 M malonic acid, 0.39 M $NaBrO_3$, and 0.69 M H_2SO_4.

in Section 2.3.2.a as a dichotomous quenched noise in one dimension in the direction of the wave front propagation. The light intensity in the homogeneous part is the same as the mean value I_0 in the inhomogeneous distribution.

Wave propagation starts at the bottom of the medium where a planar front is created as described in Section 2.3.1. As the front propagates upwards, it splits in two parts because of the nonexcitable middle region. The resulting wave fronts propagate through the corresponding medium of interest without interacting with each other. Figure 4.1 shows three instants of this propagation where the planar front in the inhomogeneous part is observed to propagate slower on average than that propagating under uniform illumination equal to the spatial average of the illumination in the inhomogeneous region. Note that the wave fronts preserve planar shape because of the 1D character of the modulation.

Several experiments were carried out to characterize the dependence of the wave front velocity on the amplitude of the disorder. The velocity of planar autowaves decreases linearly with light intensity in the illumination range considered here. The two values of the dichotomous distribution were varied around fixed mean light intensity I_0 giving rise to different amplitudes of the disorder. Velocities were measured as the ratio of the traveled distance between two points and the corresponding time interval.

The results are shown in Fig. 4.2 together with the numerical simulations performed using the Oregonator model (see Section 2.4). The continuous line is the analytical prediction based on kinematic arguments presented further. The vertical axis is the wave velocity v through the inhomogeneous medium relative to the velocity v_0 in the homogeneous
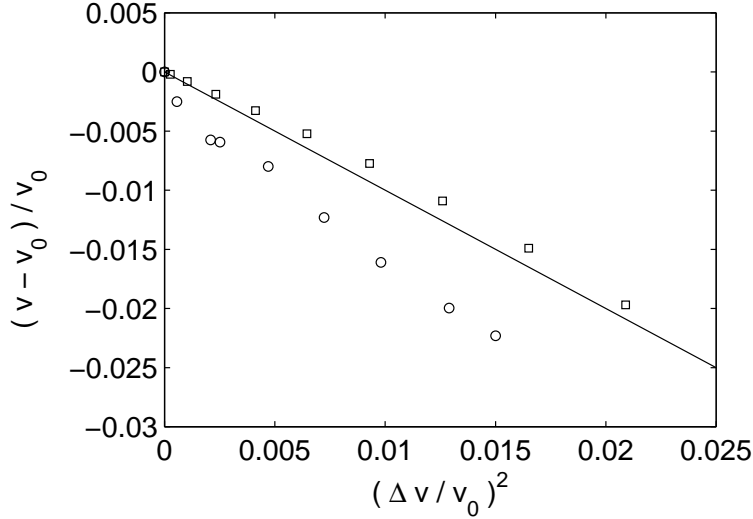
Figure 4.2: Dependence of the relative variation in wave velocity *vs* amplitude disorder both numerically ($\phi_0 = 0.01$) and experimentally ($I_0 = 0.36$ mW/cm^2). Continuous line (slope -1) represents the theoretical prediction given by Eq. (4.8). Numerical points ($\square$) were simulated with stripes of width 10 space units and the best linear fit corresponds to a slope of -0.93; experimental data (o) were obtained with squares of length of 1.1 cm and adjusted to a line of slope -1.42. Model parameters: $f = 3$, $q = 0.002$, $\varepsilon = 0.05$, $D_u = 1$, $D_v = 0$, $\phi_0 = 0.01$

part. The horizontal axis is the degree of disorder given in terms of wave velocity. The first conclusion is that one dimensional spatial disorder in excitable media induces a decrease in the wave velocity as the amplitude disorder increases. Both numerical and experimental data follow the same trend. The observed discrepancies between them probably can be caused by unavoidable experimental limitations and systematic inaccuracies in velocity measurements.

As an additional remark, there exist numerical results showing the influence of different length scales of heterogeneities on the propagation speed of pulse propagation in one spatial dimension [140]. The heterogeneous system consisted in a periodically changed excitability of modulation period d (which would correspond to our stripe size). They found an optimal size d_{opt} for which the pulse propagates faster than in the corresponding effective homogeneous medium. For $d > d_{opt}$ the velocity decreases with d. The observed feature is due to the smallness of the modulation wavelength compared to the pulse width for $d \leq d_{opt}$ (which is not our case). In these conditions the pulse profile can not completely
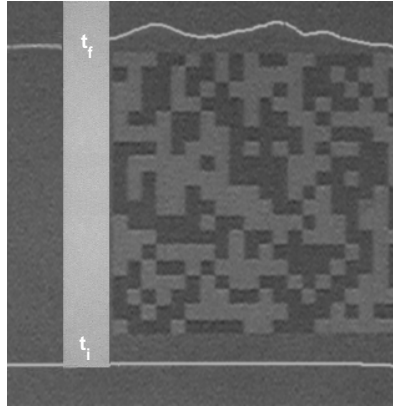
Figure 4.3: Two-dimensional setup with randomly distributed squares. An initial flat front gets distorted in the randomly illuminated zone and moves faster than in the homogeneous part; $\ell = 2.3$ mm and size of the medium in the transversal direction to the propagation is 5.4 cm. Same concentrations of reagents as in Fig. 4.1.

adapt its profile to the the local inhomogeneities as it propagates because it does not have enough time.

Our experimental and numerical conditions would fall in the limit of large modulation wavelength. In this limit, both periodically and stochastically changing excitation give rise to a propagation velocity smaller than in the corresponding homogeneous medium. Despite the authors in [140] do not analyze the velocity dependence on the difference between the two values of the dichotomic distribution, the same linear decreasing trend is expected.

4.1.2.b 2D Disorder

The 2D setup was prepared analogously to the quasi-one dimensional configuration, this time with randomly distributed squares of two possible light intensities in both directions of the inhomogeneous part, as shown in Fig. 4.3. A typical experiment consisted again in generating a planar wave at the bottom of the medium and observing its evolution along the vertical axis. In this way both the shapes and velocities of the two free-end non-interacting fronts at either side of the central stripe were compared.

Contrary to the 1D situation, in 2D, dynamically evolving, distorted although still well-defined autowaves propagate faster than the corresponding planar front propagating under uniformly distributed light with the same intensity as the spatial average over nonuniform area.

Quantitative measurements are shown in Fig. 4.4, where again the relative wave velocity in the inhomogeneous part is shown against the amplitude disorder. The wave velocity of the distorted front was measured in this case by averaging the front position $h(x, t)$ at time t_f, which is equal

to:

$$\overline{h}(t) = \frac{1}{N} \sum_{i=1}^{N} h(i, t) \tag{4.1}$$

where one summation term corresponds to one cell of the pattern.

Wave propagation was found to be dependent on the spatial correlation of the disorder. Measurements for different cell sizes carried out both numerically and experimentally are shown in Fig. 4.4. For the same amplitude of disorder, an increase in the relative wave velocity is observed as the square size becomes larger. The spatial correlation is an important factor in the wave front dynamics. As it becomes larger, the wave front gets more distorted because it has more time to adapt its profile to the local velocity field. This behavior reaches a saturation point (see Fig. 4.4) which agrees with the fact that the maximum speed of the front is given by the highest local velocity [82].

Studies of wave propagation through a medium with a checkerboard type excitability distribution have been carried out in [140] using the modified Oregonator model for light-sensitive BZ media. The authors investigate the dependence of the wave front velocity on the size of the spatial inhomogeneity obtaining higher pulse velocities than the one corresponding to the equivalent homogeneous situation. But again they do not consider the dependence on the difference of the two excitation values of the checkerboard. But within the context of growing interfaces in weak stirred fluids, periodic flow fields consisting in a checkerboard pattern of vortices of opposite signs yield quadratic dependence of the propagation-rate increment $v - v_0$ on the amplitude disorder.

These experimental observations of the differences between propagation in a one and two dimensional disorder are also found in numerical simulations. These will be discussed and interpreted in the next section in the framework of the kinematical analysis.

4.1.2.c   Theoretical Interpretation

Before proceeding further let us clearly state the conditions with which our experimental and numerical study comply. This will enable us to interpret the observed results in terms of generic kinematic arguments widening in this way the scope of our study beyond the particular randomness realization analyzed here:

  i) We restrict ourselves to thin fronts measured on the length scale introduced by the disorder.
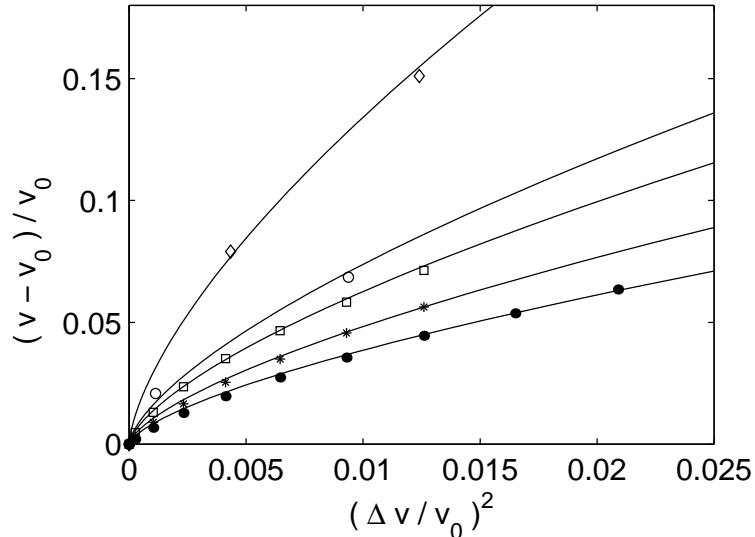
Figure 4.4: Dependence of the relative variation in wave velocity on the amplitude of disorder from simulations ($\phi_0 = 0.01$) and experiments ($I_0 = 0.36$ mW/cm^2). Simulations: medium width of 160 space units with noise squares 10 ($\bullet$), 20 ($\ast$) and 40 ($\square$) units in size. Continuous lines represent non-linear fits of Eq. (4.12), with $\beta = 0.831$, 1.04 and 1.35 respectively. The typical front width is about 2.5 s.u. Experimental results are shown for a medium width of 5.4 cm and $\ell = 2.3$ mm (o), and for 6 cm and $\ell = 2.7$ mm ($\diamond$), with $\beta = 1.59$ and 2.89 respectively. Model parameters are the same as in Fig. 4.2.

  ii) We verify, both experimentally and numerically, that the autowave speed adapts quasi-adiabatically to the local conditions.

 iii) Finally, in 2D case, we assume that the amplitude of disorder, i.e., a measure of the dispersion of local velocities in our two-state model, is small.

In particular for the 2D case, the above conditions lead us to conclude that diffusion lengths in this problem will always be considerably smaller than the length scale associated to the front deformation. In turn this justifies the use, both as a central theoretical issue as well as an advantageous computational resource, of the linear speed-curvature relation, also well-known as first-order eikonal equation ([43, 44, 141, 142] and for a much more recent treatment see also [143, 144] and references therein), which gives the normal velocity of the autowave in terms of its local plane-wave value corrected by a curvature term (see Appendix A). On

the other hand, by invoking condition (ii), this local velocity is assumed to be at any time fixed by the space-dependent illumination. We translate such a relation into Cartesian coordinates for the position of the front, denoted $y = h(x, t)$ (Appendix A):

$$h_t = v(x, h)\sqrt{1 + (h_x)^2} + D\frac{h_{xx}}{1 + (h_x)^2} \tag{4.2}$$

where D is an effective diffusion coefficient and, in general, a function of diffusion coefficients of the species involved in the front propagation. This coefficient is assumed to be independent of the light intensity [82, 145]. Besides conditions (i) and (iii) and the assumption of isolated fronts, let us consider Eq. (4.2) to be valid within the Zykov's limit (see ref. [44]). D has been estimated from the integration of the full Oregonator model with circular fronts. To validate our assumptions, both versions, the complete reaction-diffusion scheme (2.20)-(2.21) and the local one (4.2), were checked to give the same results with great accuracy, for both front shapes and velocities.

Let us formulate our theoretical scenario. In a 1D situation, and invoking conditions (i) and (ii), the propagating interface can be viewed as a point-like object which follows instantaneously a spatial profile of velocity $v(y) = v_0 + \delta v(y)$, which is two-valued and characterized by

$$\langle v(y) \rangle = 0$$
$$\langle v(y) \rangle = (\delta v)^2$$

It may be convenient to relate the time-averaged velocity $\bar{v}$ to the statistical properties of $v(y)$. If the medium width L is large enough compared to the spatial correlations of the disorder and under self-averaging conditions, then

$$\frac{1}{\bar{v}} = < \frac{1}{v(y)} > \tag{4.3}$$

Substitution of $v(y)$ and taking v_0 as a common factor gives

$$< \frac{1}{v(y)} > = \frac{1}{v_0} < \frac{1}{1 + \frac{\delta v}{v_0}} > \tag{4.4}$$

Considering $\delta v(y)$ to be bounded by $|\delta v(y)| < v_0$, the Taylor series expansion of the right part of this equation reads,

$$< \frac{1}{v(y)} > = \frac{1}{v_0} \sum_{n=0}^{\infty} (-1)^n < \left(\frac{\delta v}{v_0}\right)^n > \tag{4.5}$$

expression which relates the time-averaged velocity to the statistical moments of the disorder. For the two-state model considered here, $\delta v \equiv \pm \Delta v$, the right part of Eq. (4.5) can be computed exactly,

$$< \frac{1}{v(y)} > = \frac{1}{v_0} \sum_{n=0}^{\infty} \left(\frac{\Delta v}{v_0} \right)^{2n} \tag{4.6}$$

and immediately following from these Taylor series,

$$< \frac{1}{v(y)} > = \frac{1}{v_0} \left(\frac{1}{1 - (\frac{\delta v}{v_0})^2} \right) \tag{4.7}$$

Rearranging terms, we obtain an equation in terms of a reduced velocity, which relates the time-averaged velocity and the amplitude of disorder

$$\frac{\bar{v} - v_0}{v_0} = - \left(\frac{\Delta v}{v_0} \right)^2 \tag{4.8}$$

The theoretical prediction represented by this equation was compared with numerical and experimental results in Fig. 4.2. The quantitative agreement is excellent in the numerical simulations. Experimental results also support the previous theoretical considerations given the unavoidable experimental limitations mainly due to light dispersion and intrinsic inaccuracies in velocity measurements. This effect is shown in Fig. 4.2 where experimental data deviate from the theoretical prediction (continuous line) as the amplitude of disorder increases. Here, the inhibitor which is continuously produced in the brighter squares tends to invade the darker ones, increasing there the *effective* value of the illumination intensity. This effect becomes more important as the amplitude of the disorder increases. Therefore, the corresponding mean value of the light intensity I_0 varies slightly with the amplitude of disorder.

It should be remarked that the previous expression derived for a 1D random excitability distribution can be easily obtained for a periodic distribution giving rise to the same result. If we consider N squares of size ℓ of alternating excitabilities corresponding to speeds $v_+ = v_0 + \Delta v$ and $v_- = v_0 - \Delta v$, the time-averaged velocity after propagating a distance $L = N\ell$ is $\bar{v} = L/T$, where $T = t_1 + t_2 + ... + t_N$ and t_i is the time spent in each square. Because of the periodically changing excitability, $T = \frac{N}{2}(t_+ + t_-)$ being $t_+ = \ell/v_+$ and $t_- = \ell/v_-$. Substituting T and

making some calculations, we obtain

$$\overline{v} = \frac{L}{T} = \frac{N\ell}{\frac{N}{2}(\frac{1}{v_+} + \frac{1}{v_-})} = \frac{v_0^2 - \Delta v^2}{v_0} \tag{4.9}$$

which gives the same dependence as Eq. (4.8).

In 2D the situation is more involved. We start directly from our central equation (4.2) and develop it, consistently with approximations (i)-(iii) above, using a small-gradient approximation for $(1 + h_x^2)^{\pm 1/2} \sim 1 \pm \frac{1}{2}h_x^2$. Noting $v(x, h) = v_0 + \delta v(x, h)$ and retaining the lowest-order nonlinearity on h_x we have

$$h_t = v_0 + \frac{v_0}{2}(h_x)^2 + Dh_{xx} + \delta v(x, h) \tag{4.10}$$

where an extra multiplicative term $(h_x)^2 \delta v(x, h)$ has been neglected assuming small amplitudes of disorder. Notice that, written in this way and after some trivial reparameterization to remove the trivial v_0 term ($h \rightarrow h - v_0 t$), this equation strongly resembles the well-known KPZ model for the propagation of random interfaces [15]. A quite similar KPZ-like equation has also been considered by Kerstein and Ashurst [14] when dealing with interfaces propagating in randomly advected media. The only notable difference in their equation is that the diffusive term h_{xx}, responsible for the transverse redistribution of fluctuations along the interface, is replaced by a product of h_x with the transverse component of the advecting flow. They have also shown that for weak randomness (weak stirring) such transverse redistribution effect is irrelevant for their scaling analysis. What makes such an analysis particularly appropriate to our situation is that the authors have focussed explicitly on the limit of frozen flows, which is completely equivalent to our scenario of quenched disorder. Under these conditions the main result reads explicitly [14],

$$u_T = \lambda + c\lambda \left(\frac{u'}{\lambda}\right)^p \tag{4.11}$$

being u_T the steady propagation velocity, λ the laminar flame speed, u' the root-mean square velocity fluctuation of the flow field, c a numerical coefficient, and $p = \frac{4}{3}$. Identifying u_T, λ, and u' with v, v_0 and Δv respectively, and rearranging terms, Eq. (4.11) transforms into

$$\frac{\bar{v} - v_0}{v_0} = \beta \left[\left(\frac{\Delta v}{v_0}\right)^2\right]^{2/3} \tag{4.12}$$

We use this equation to fit the numerical and experimental results in Fig. 4.4 with good quantitative agreement. In particular, the observed power laws and corresponding exponent are consistent with the theoretical prediction, whereas the prefactor β in Eq. (4.12) is clearly seen to depend on the length scale of the spatial inhomogeneities.

4.1.2.d   Conclusions

In excitable media spatiotemporal variation of the medium's properties provides a rich set of possibilities for affecting wave front dynamics. We have studied propagation in a medium whose dichotomic time-independent excitability varies randomly in space. In 1D, the relative variation of the velocity with respect to the velocity v_0 in the corresponding effective homogeneous medium decreases linearly with Δv, as the total time spent in crossing the whole medium becomes larger. In 2D, the propagation-rate $v - v_0$ increases proportionally to the $\frac{4}{3}$ power of the disorder amplitude relative to v_0. This time the front gets distorted and the interplay between curvature (influenced by the length of the inhomogeneity) and the fast and slow motion of the wave parts determine the velocity of the whole front.

4.1.3   Percolation Phenomena

Many physical processes are easily explained within the context of percolation theory. Such processes are called critical phenomena in the sense that a peculiar behavior emerges near some critical value related to geometry. An illustrative example is that of an insulating surface randomly covered by small pieces of a conductive material. As we add more and more of the conductive patches, the conduction across the surface will at some point suddenly jump from zero up to some high value and will increase relatively slowly after that. There are other similar examples such as spreading of the fire in a forest as a function of the density of combustible material or percolation of a fluid through a porous substrate as a function of substrate porosity. In each of these cases there is a critical value of the relevant parameter dramatically changing the mode of conductance, fire spreading, etc.

A simple percolation model is a 2-dimensional square lattice, with cells randomly populated with a probability p. If the number of cells is very large, we see that for small probabilities p, there is no path through the populated cells connecting the opposite sides of the lattice. However, this path always exits for $p > p_c$. Specifically, the first connecting path of infinite
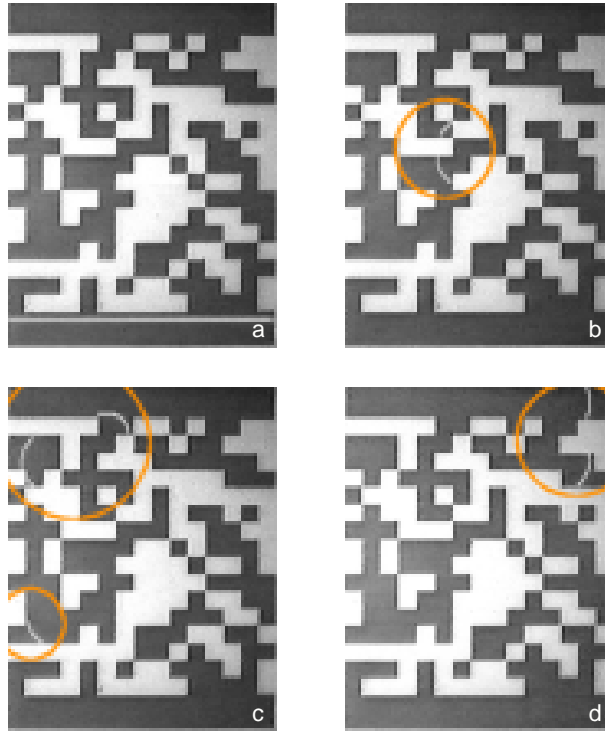
Figure 4.5: Four different snapshots of the propagation of a wave front through a light sensitive BZ medium consisting of a random distribution of excitable squares (black squares) in a nonexcitable medium (white squares). The wave can propagate only through black sites. The initial wave front propagating from the bottom, (a), breaks up and only a small part reaches the top while other fronts move around the lattice, (b-d). Times, (a) 0 s, (b) 778 s, (c) 1068 s and (d) 1405 s. (Proportion of black squares, $p = 0.5$; size square, 3 mm; medium size, 4.5 cm $\times$ 6 cm; light intensity in black squares, 250 μW/cm^2, and in white squares, 750 μW/cm^2.

length appears at $p = p_c$ (for an infinite lattice) and with increasing p its length reduces to the limit ultimately set by a straight connection between the sides of the lattice.

The phenomenology described above has the same features as the one observed with autowaves propagating through a disordered medium with nonexcitable clusters (see Fig. 2.6). This is shown in Fig. 4.5 where a planar wave front starts to propagate at the bottom-side of the medium and reaches the top side after breaking up into several parts due to the white cells that are nonexcitable. Figure 4.5 shows in four different panels the time evolution of a wave front in a single experiment. Only one of them

reaches the upper side, whereas the others wander around the lattice until their total annihilation, Fig. 4.5(d).

Experimental measurements of the *transit* and *termination times* (which will be defined later) were done for different values of the proportion p of squares with a given light intensity (excitability). Five experiments were carried out for each value of p. Each realization corresponds to a different inhomogeneous pattern of $n \times m$ randomly distributed dark and light squares (black and white from now on) of light intensities I_b and I_w respectively, chosen in such a way that the wave cannot propagate through the white squares. This favors the breaking up of the front into several small fronts that move independently through the lattice. In order to change the actual connectivity of the two–dimensional lattice, two different light intensities were used for the dark squares. With the lowest light intensity, waves can propagate from a black site both to the nearest neighbor black squares (squares with one side in common) and to the next-nearest black neighbors (squares with one vertex in common) (see Fig. 4.6(a1-a3)). With the highest light intensity, waves can only propagate between two black sites with a common side (Fig. 4.6(b1-b3)). Figure 4.6 bottom shows a schematic drawing of the two types of connectivity within the lattice, where top and bottom lines are connected through the occupied sites represented by the bigger dots.

Figure 4.7 exhibit the footprint of percolation phenomena. The inverse of the transit time is shown averaged over five realizations for each p. The transit time is defined as the time elapsed from the wave front leaving the bottom part of the medium until some small piece of it reaches first the top. No successful wave propagation is found below a critical value p_c which depends on the light intensity used for the black cells, $p_c \approx 0.4$ or $p_c \approx 0.6$. For p well below p_c, there are mostly isolated sites and a few small clusters, so that the wave front cannot reach the upper edge of the pattern. For p well above p_c, most of the black sites belong to the *infinite cluster*, and the transit time is approximately constant. At the percolation threshold, p_c, a fractal path of neighboring black squares appears which connects the bottom with the top of the medium for the first time, either through the corners or common sides, $p_c \approx 0.4$, or only through the common sides, $p_c \approx 0.6$. As a result, even though the wave propagates through the medium, the percolating cluster is very different from a straight line, slowing the wave front down.

What happens near p_c is called *critical phenomena* and most of the quantities that describe the system either become null or diverge at p_c as
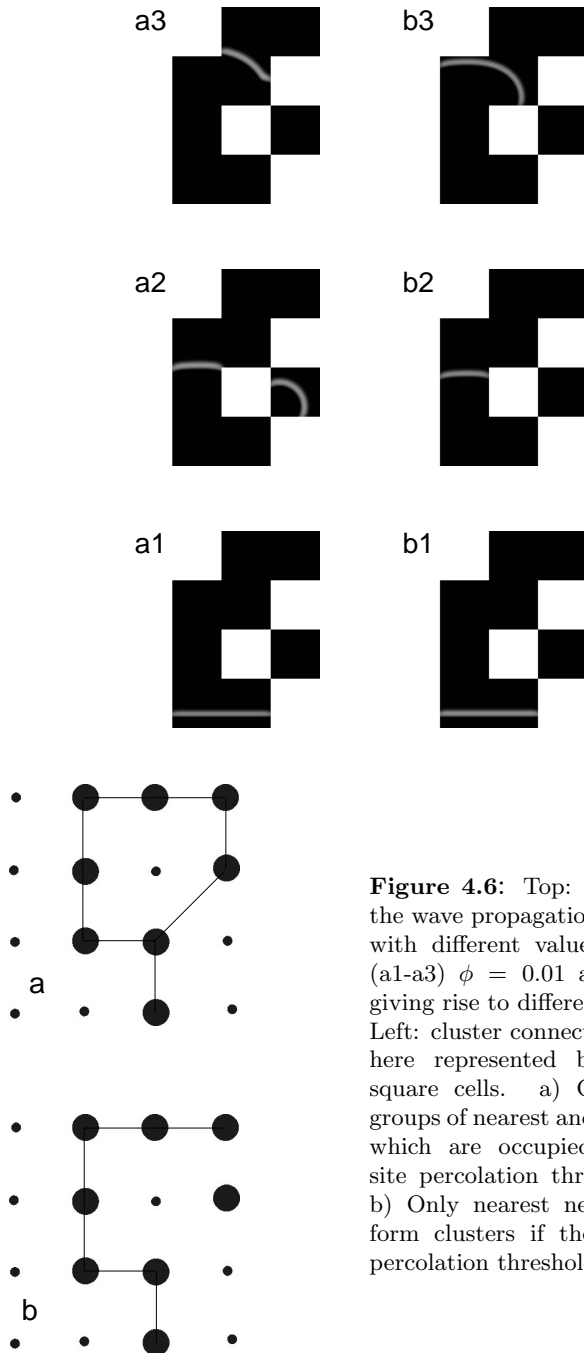
Figure 4.6: Top: numerical simulation of the wave propagation through black squares with different values of the parameter ϕ, (a1-a3) $\phi = 0.01$ and (b1-b3) $\phi = 0.015$ giving rise to different types of connectivity. Left: cluster connectivity in a square lattice here represented by the centers of the square cells. a) Clusters are defined as groups of nearest and next-nearest neighbors which are occupied (bigger dots). The site percolation threshold is about 0.4072. b) Only nearest neighbors are allowed to form clusters if they are occupied. The percolation threshold is shifted to 0.5928.
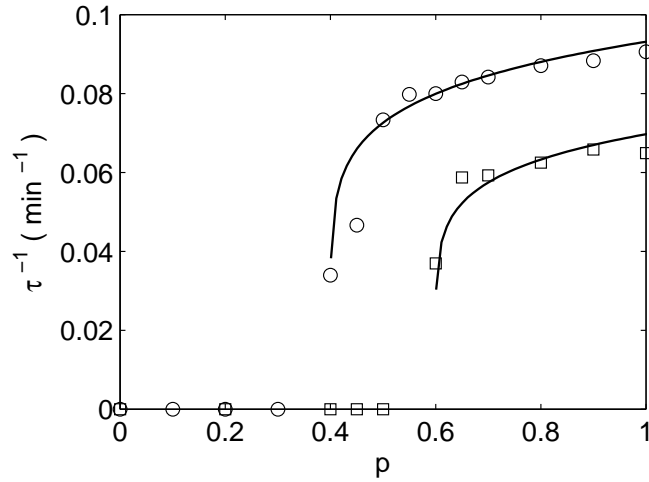
Figure 4.7: Inverse of the transit time for propagation between both edges of the experimental system (see text) is plotted as a function of the probability of black sites p. The continuous lines represent nonlinear fits to Eq. (4.13) above the percolation threshold for two different geometries, ($\square$) cells connected by common sides, (o) cells connected by common sides and corners. At least five experiments were carried out for each value of p in order to compare with theoretical results typical of infinite media. Parameters of the fitting curves are: (o) $\alpha = 0.1$, $p_c = 0.4$. ($\square$) $\alpha = 0.08$, $p_c = 0.6$.

a power law according to a critical exponent. In our case, the fraction P of sites belonging to the infinite network is proportional to the inverse of the transit time τ: for large lattices we have no propagation ($\tau^{-1} = 0$) if no infinite network of neighbors is present, that is for $p < p_c$. When p is appreciably larger than p_c, nearly all the black squares have clustered together to form one infinite network, and the wave front velocity ($\propto \tau^{-1}$) as well as the fraction P of sites in the infinite network increase linearly with p. We expect that this linear relationship between P and τ^{-1} holds for the whole range of p.

From percolation theory, the parameter P obeys a power law when $p \to p_c$, in the form $P \propto (p - p_c)^\beta$. The critical exponent β describes how rapidly the connectivity of the infinite network disappears at the percolation threshold. In Fig. 4.7, points corresponding to the elapsed time for $p > p_c$ were fitted as

$$\tau^{-1} = \alpha(p - p_c)^\beta \tag{4.13}$$

with the critical exponent $\beta = \frac{5}{36}$ corresponding to the square lattice [132]. It should be noted that critical exponent only depends on the
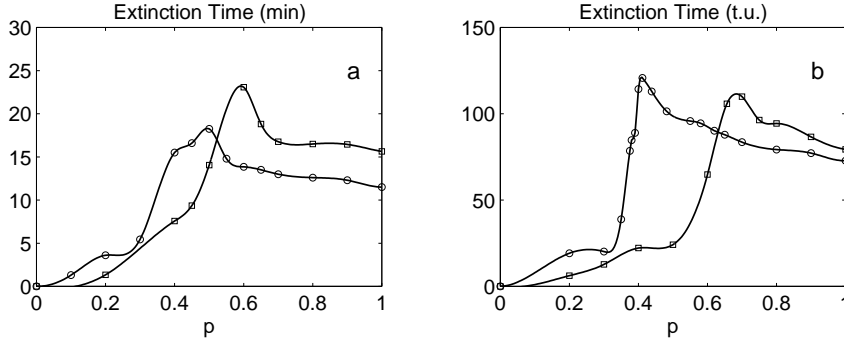
Figure 4.8: Extinction time for autowaves propagating through lattices with probability of black sites p, (left) experimental, (right) numerical simulations, for two different lattice geometries (symbols have the same meaning as in Fig. 4.7). For $p \to 0$, the front can propagate only through a few black sites before extinction, while for $p \to 1$, almost the whole front reaches the top of the lattice. In between, at the cusp the small broken parts of the front spend an *infinite* time wandering through the lattice until annihilation. Solid lines are spline interpolations of the experimental and numerical data (which are averaged over 10 runs for each value of p). (a) Experiments: Maxima located at (o) $p_c \approx 0.5$, ($\square$) $p_c = 0.6$. Parameters as in Fig. 4.7. (b) Simulations: Maxima located at (o) $p_c \approx 0.45$, ($\square$) $p_c = 0.6$. Model parameters: $\Delta t = 0.001$, $\Delta x = 0.3$, $f = 3$, $q = 0.002$, $\varepsilon = 0.05$, $D_u = 1$, $D_v = 0$, $\phi_b = 0.01(0.015)$ $\phi_w = 0.04(0.04)$ to produce $p_c \approx 0.45$, ($p_c = 0.6$).

dimensionality of the lattice and does not depend on its structure. Thus, regardless of the different number of neighbors on a given black site (eight and four), the disappearance of the connecting network at the percolation threshold follows the same law, only at different percolation thresholds (0.5928 and 0.4072, respectively).

The extinction time is defined as the time elapsed until complete disappearance of all waves from the same lattice. Figures 4.8(a-b) show the lifetime of autowaves averaged over many lattices with the same p as a function of probability p for two spatial geometries: square lattice connected only by nearest neighbors and by both nearest and next-nearest neighbors. Experiments show a peak at $p \approx 0.6$ for the first geometry and near $p \approx 0.5$ for the second one. At $p \approx 0.6$ extinction times are longer than at $p \approx 0.5$ because in experiments light intensity was kept higher in order to restrict wave propagation through sides in common only, thus decreasing wave velocity. The presence of such peaks is associated to the fractal properties of the connecting cluster present at $p = p_c$, whose length (and hence the corresponding transit time) is no longer linearly proportional to the length of the lattice. Due to finite-size effects the peaks appear as of finite height, and are round shaped. In fact, the value of

$p \approx 0.5$ does not match exactly the threshold $p_c = 0.4072$ predicted by the theory and found in the transit times measurements of Fig. 4.7. However, in the simulations lattice sizes were larger, and the critical value obtained in Fig. 4.8(b), $p_c \approx 0.4$, agrees better with the expected value[1].

4.2 Noise-Enhanced Wave Train Propagation in Unexcitable Media

4.2.1 Introduction

Several publications have appeared recently regarding the effects of noise on spatial structures in dynamical systems [5, 96, 130, 131, 95, 11, 10]. Most of them have dealt with *single front* propagation in *subcritical* conditions, which is enhanced when an optimal *level* of noise is added to the system. This phenomenon implies that noisy backgrounds can help weak signal transmission through neural fibers [146, 147] or other nonlinear electronic circuits [8, 107]. The phenomenon lying behind these examples is generally referred to as "stochastic resonance"[148].

In 1998, Kádár *et al.* described noise-supported traveling waves in two-dimensional *subexcitable* media [11]. Spatiotemporal noise was applied to a photosensitive chemical medium for different pixel sizes and using a Gaussian noise updated at regular time intervals. An optimal noise level was found at which the relative signal strength became maximal. The authors also suggested the existence of an optimal noise *time scale* supporting propagation. As it was explained in Chapter 1, in subcritical conditions of excitability, there are two different modes of propagation: *subexcitable* [11, 10, 108] and *unexcitable*. In the *sub*excitable regime, wave segments with free ends contract tangentially and may eventually disappear, depending on their size and shape. In the *un*excitable one, any initial perturbation decays in amplitude until it eventually disappears. This last scenario is more dramatic since even unbounded waves disappear.

In the present section we study the propagation of a one dimensional *train* of wave fronts in the unexcitable regime under a spatiotemporal noise forcing [149]. Because of the one-dimensional situation we are considering, only transitions from excitable to unexcitable regimes are possible. The consideration of a time periodic structure introduces a new feature: the possibility of interaction between consecutive fronts. We expect to find

---

[1]The numerical calculations included in Section 4.1 have been performed by Daniel Vives, who has collaborated with our group during this PhD thesis.
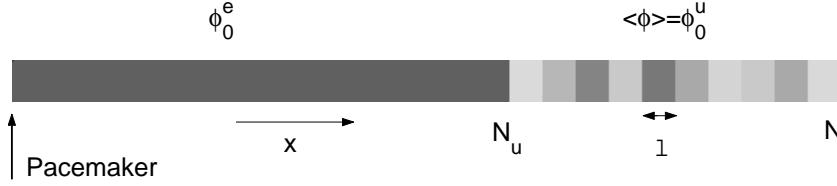
Figure 4.9: Simulated medium with the excitability represented in a eight-bit gray scale. N_u denotes the boundary between the excitable region on the left, where the wave train is created and propagates, and the spatial distribution of cells of size ℓ that fluctuate independently of one another around a mean value ϕ_0^u in the nonexcitable region.

different rates of supported transmission depending on the period of the wave train and on the correlation time of the noise. Previous studies have found stochastic resonance related to the intensity of the noise giving rise to an improvement of the wave front propagation through a subexcitable medium. Here, we will try to determine from a numerical point of view the effects on the propagation of a *periodic* wave train through an unexcitable channel of a time-correlated spatiotemporal noise as a function of its noise *intensity*, correlation *time* and correlation *length*.

4.2.2 Numerical Model

Numerical studies were performed using the two-variable Oregonator model introduced in Section 2.4.2 with a time step of 10^{-3} t.u. and a grid size of 0.15 s.u. in a one dimensional array of $N = 1000$ points. Zero flux boundary conditions were maintained at the end of the system. The spatiotemporal fluctuations were introduced through the light intensity parameter ϕ in Eq. (2.20). Under homogeneous illumination, the system becomes unexcitable for $\phi > 0.024$.

Pulses of constant amplitude $A = 0.2$ and width $\delta t = 0.1$ t.u. (equal to 100 time steps) were periodically delivered at $x = 0$, in order to obtain a wave train with constant period T. Waves develop and travel through an excitable medium (its properties being determined by the value of $\phi_0^e = 0.002$) of size $N_u = 600$ points before entering the unexcitable region, consisting of an array of independent fluctuating cells of size ℓ lattice units, with average light intensity $\phi_0^u = 0.025$ (see Fig. 4.9). The expression for

the fluctuating field as a function of the position is thus:

$$\phi(x,t) = \begin{cases} \phi_0^e & 0 < x < N_u \\ \phi_0^u + \sum_{i=1}^{n_l}\xi_i(t)\Theta_i(x) & N_u \le x \le N \end{cases} \tag{4.14}$$

where i is the discrete coordinate of a noise cell ranging from 1 to $n_l = (N - N_u)/\ell$ and $\Theta_i(x)$ is a shorthand for $\Theta_i(x) = \Theta(x - (i-1)\ell)\,\Theta(i\ell - x)$, with Θ being the Heaviside function. $\xi_i(t)$ stands for an Ornstein-Uhlenbeck process at a cell i, namely a Gaussian process with zero mean and a correlation function $\langle\xi_i(t)\xi_l(t')\rangle = \sigma^2\exp(-|t - t'|/\tau)\delta_{il}$, which is the same expression as Eq. (2.33) except for the spatial correlation. The parameter ℓ fixes the characteristic length of the inhomogeneous fluctuating excitability. In the limit $\tau \to 0$ the white–noise limit $\xi_w(t)$ is recovered if $\sigma^2\tau$ is finite. For $\tau \to \infty$ the *frozen* or static Gaussian distributed noise is obtained. Numerical simulations have been carried out by varying the noise dispersion σ, the correlation time τ and the noise pixel size ℓ. The control points were equally distributed (each 25 lattice units) along the unexcitable channel, and another one was placed in the excitable zone ($x = 500$). Measurements of the ratio between the number of wave fronts reaching each control point to the number of waves exiting the excitable region were performed and averaged over five realizations.

4.2.3   Results

Without noise ($\sigma = 0$) waves entering the unexcitable region immediately die out. With modulation, depending on the noise parameters waves can travel longer distances. The distance also depends on the period T of the wave train. Figure 4.10 shows the percentage of wave fronts reaching each control point beyond the border between the excitable and the unexcitable regions with and without noise. Note the exponential decay with x ($x > N_u$) when noise is present, compared to the abrupt (linear) fall when it is absent, indicating that a few fronts are able to survive and do indeed reach very far. On the other hand, it seems that more spaced fronts ($T > 5$) are more vulnerable to noise, since the distance to which all of them arrive is drastically reduced.

The main results of the numerical simulations performed varying the different noise parameters are summarized in Fig. 4.11 for a constant value of $T = 5$ t.u. A colormap plot represents the percentage of wave fronts reaching the control point situated at 175 points beyond the border ($N_u =$
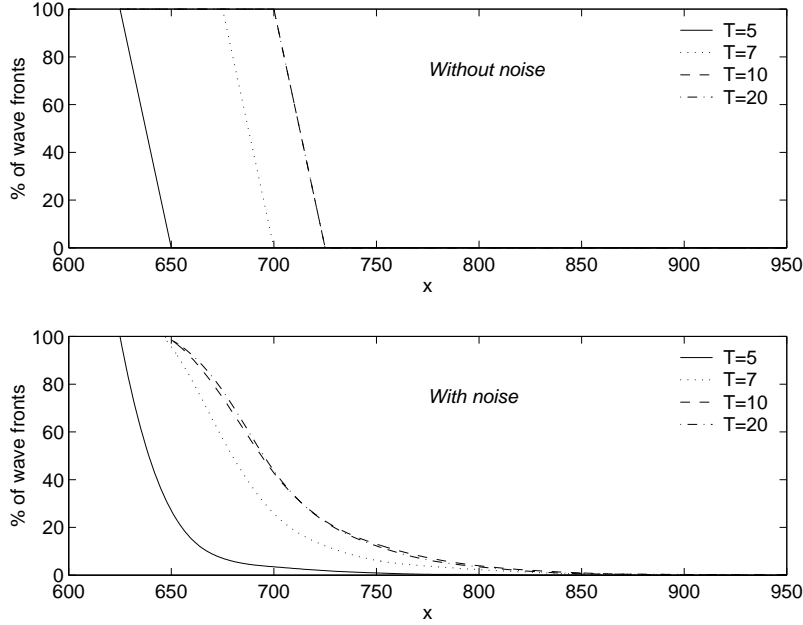
Figure 4.10: Percentage of wave fronts reaching the different control points placed along the unexcitable region $(x > N_u)$, with (bottom) and without noise (top), for several periods of the wave train. Numerical parameters: $\varepsilon = 0.05$, $f = 3$, $q = 0.002$, $D_u = 1$, and $D_v = 0$. Noise parameters: $\sigma = 0.001$, $\log_{10} \tau = -0.75$, $\ell = 40$ points.

600) as a function of the noise dispersion σ and the correlation time τ, for three different values of the noise pixel size ℓ. From the figures it is evident that *wave propagation depends on the spatial correlation of the noise*. As ℓ is increased, the percentage of wave fronts reaching the control position increases as well (note the different scales on the colorbars) and they reach a maximum for higher values of the correlation time.

- For $\ell = 10$, the noise pixel size is slightly smaller than the front width (≈ 20 lattice spacings) and there is no noise level or time scale for the noise that appears to be optimal. Instead, up to a critical value of the noise intensity (below which the transmission rate is zero) there is a sharp increase that saturates for high values of σ. No clear dependence on the correlation time is observed.

- For $\ell = 100$ there are large highly correlated regions, such that each front propagates under almost pure temporal noise. For low correlation times, temporal fluctuations occur so frequently that they are effectively averaged out. On the other hand, for $\tau > T$ the noise
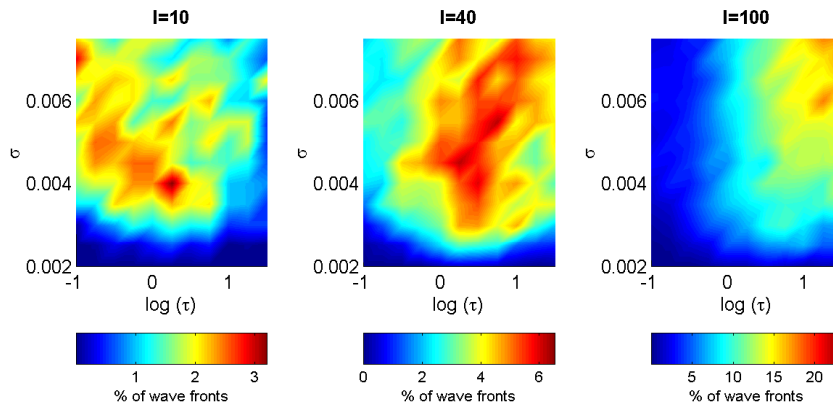
Figure 4.11: Colormap plots of the percentage of wave fronts reaching the control position at $x = N_u + 175$, as a function of the noise dispersion σ and correlation time τ for three different noise pixel sizes ℓ. Note the different scales on the percentage of wave fronts of the colorbars. Numerical parameters: $\varepsilon = 0.05$, $f = 3$, $q = 0.002$, $D_u = 1$ and $T = 5$ t.u.

     varies slowly and there are fluctuations that allow the propagation to last longer.

- For $\ell = 40$ there is a compromise between noise intensity and noise correlation time, giving rise to a tiny improvement on wave propagation for intermediate values of σ and for correlation times of the order of the period of the wave train $T = 5$.

The global effect of increasing the spatial correlation is thus a shift to the right of the maximum for the transmission rate, here shown as a red area on Fig. 4.11.

    For $\ell = 40$ and a constant value of τ (~ 1) there occurs stochastic resonance as a function of the noise amplitude. A better perspective of the phenomenon is given in Fig. 4.12, for $T = 20$ t.u. and at different control points. Close to the boundary N_u the transmission rate decreases as σ increases, see Fig. 4.12(a). But far away from the extinction point for the deterministic unexcitable system ($x > 125$) the rate of wave fronts that reach distant positions exhibits a peak as a function of the noise variance σ^2 (the signature of a stochastic resonance) Fig. 4.12(b).

    A resonance-like behavior is also observed with respect to the correlation time. Figure 4.13 shows the percentage of wave fronts versus τ for different control positions at constant noise intensity σ. As in the previous case, a local maximum develops as τ increases (Fig. 4.13(b)), while for $\tau \to 0$
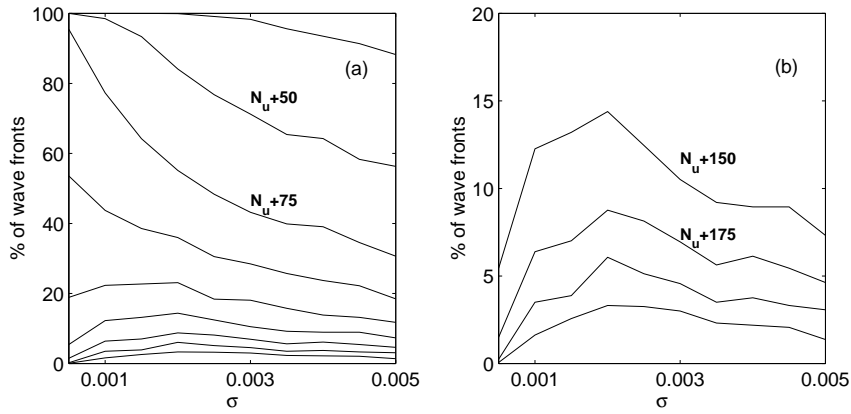
Figure 4.12: Percentage of wave fronts reaching the positions indicated as labels superimposed to the graphs, as a function of the noise dispersion σ, for $T = 20$ t.u., $\ell = 40$ and $\log(\tau) = -0.75$. (b) corresponds to a magnification of (a).
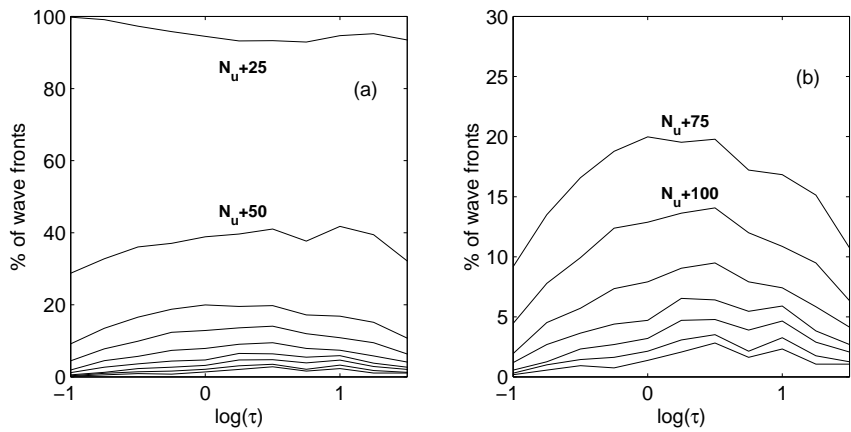
Figure 4.13: Percentage of wave fronts reaching the positions indicated as labels superimposed to the graphs, as a function of the correlation time τ, for $T = 5$ t.u., $\ell = 40$ and $\sigma = 0.001$. (b) corresponds to a magnification of (a).

the medium averages fluctuations and for $\tau \to \infty$ the wave train has to overcome a static structured noise.

In order to gain an insight into the meaning of this last behavior, we have represented the percentage of wave fronts reaching a fixed position $(x = N_u + 175)$ for two different frequencies of pulse initiation, as a function of τ. The result is plot in Fig. 4.14. It can be observed that the maximum rate occurs at different values of τ and that this value is of the order of the
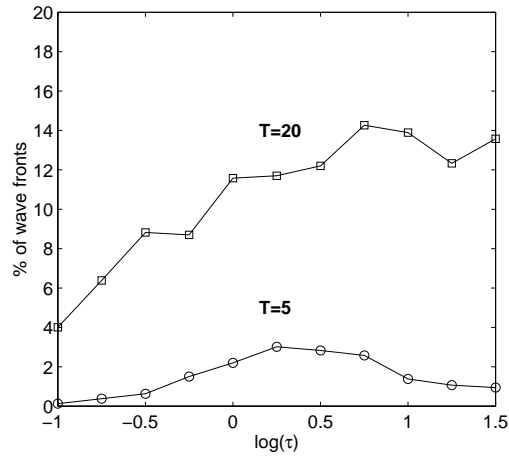
Figure 4.14: Behavior of the rate of collected wave fronts reaching position $x = N_u + 175$ as a function of the correlation time τ, for two different periods of the wave train T. Noise parameters: $\sigma = 0.001$ and $\ell = 40$.

period of the wave train.

4.3   Conclusions

We have investigated the effect of spatiotemporal fluctuations on a wave train propagating in an unexcitable regime and shown that stochastic resonance occurs not only for an optimal intensity of the noise but also for a correlation time that matches the characteristic time of the periodic structure. Generally, the introduction of noise has extended the propagation length. This is in agreement with other studies in noisy overdamped bistable oscillators [107, 150, 151] where the interplay among noise, nonlinearity and forcing gives rise to an enhancement of propagation.

Chapter 5

Noise-Induced Brownian Motion of Spiral Patterns

Abstract.   *Spiral chemical waves are experimentally and numerically investigated in the light-sensitive Belousov-Zhabotinsky reaction under randomly induced spatiotemporal variations of excitability.   When the randomness is absent, the spiral tip performs a circular motion around the core, while when spatiotemporal disorder is switched on Brownian motion is identified.   This is characterized by an effective diffusion coefficient which shows a rather complex dependence on the time and length scales of the noise relative to those of the spiral.   In particular, a resonant-like effect was observed with the time correlation and the noise dispersion fixed. A kinematically based model is used to interpret the spiral motion whose results are in good qualitative agreement with experiments and numerics.*

5.1   Introduction

Spirals are generic structures in extended nonequilibrium systems. They occur in many reaction-diffusion systems [33], such as the well-known Belousov-Zhabotinsky (BZ) reaction [13]. They have also been observed in a heart muscle during cardiac fibrillation [49, 152] and during aggregation of Dictyostelium amoebae [153].   Spiral rotating patterns have also been observed experimentally in extended electronic media such as a dc driven planar semiconductor, in freely propagating flames in combustion systems [154] or in the Rayleigh- Bénard convection for certain regimes of temperature difference across a layer of fluid [21, 32]. Spiral patterns also appear as elementary oscillatory solutions of the Complex Ginzburg-Landau (CGL) equation [155] .

Due to their presence in such diverse systems, spiral waves have been study widely both by theorists [156, 157, 158, 159, 60] and experimentalists

[13, 39] in attempts to elucidate the dynamical laws governing their development and motion. Depending on the system, different mechanisms of spiral initiation are possible. Spatial differences in the recovery properties, invasion of a wave into a vulnerable region of the preceding wave [59], as well as sharp boundaries or obstacles [57, 160, 55] are known to be able to generate spiral waves. Of particular relevance to our study, in a BZ reaction with catalyst immobilized on the resin beads [116] the number of spontaneously initiated spirals has been found to depend on the size of the bead and the level of excitability of the medium.

Beyond the standard description of spiral waves, their response to spatial and temporal forcing has been largely analyzed. With respect to temporal forcing [91, 16, 79], periodical modulation of a parameter may lead to a resonant behavior such as drift of vortices [91, 92]. Temporal [79, 161] and spatial [16] synchronization occurs when the forcing entrains the internal oscillatory dynamics with a sequence of frequency-locked regimes that can be observed as the forcing frequency is varied. Spatial forcing has been introduced as a light gradient both rotationally and translationally invariant in space [93] which induced a resonance drift of a spiral wave equivalent to the one produced by a periodic light modulation in a spatially uniform medium. Drift of vortices has also been observed under dc [162, 163] and ac [164] electric fields and periodical mechanical deformations of an elastic excitable medium [94]. Several studies have shown that the drift of a spiral as a whole can also occur due to its interaction with a boundary [98, 100], with other spirals [165, 166] or with defects [167, 168] which may break the translational symmetry of the medium.

The influence of random heterogeneities on extended excitable systems has also attracted a considerable attention. Fluctuations in excitable media have been used as initiator of new spatial structures [116, 10, 169] where the presence of random perturbations has been found to be necessary for creation and sustained maintenance of coherent structures. In particular, García-Ojalvo *et al.* [169] studied how parametric noise is able to induce a complex behavior in a simple numerical model of excitable media whose dynamics, in the absence of noise, consists of a simple spiral wave which stays static or performs a meandering motion. Close to the propagation threshold, in terms of the spatial coupling, the presence of noise gives rise to a permanent turbulent state which resembles the spiral breakup in the ventricular fibrillation in the heart muscle [112, 97]. Other constructive applications of noise concentrate in media which can not support wave propagation in deterministic homogeneous conditions. That is the case in

sustained wave propagation in subexcitable media [114, 11, 106] which is a subject of much theoretical and experimental interest.

Complementary, the role of superimposed disorder on preexisting spatiotemporal patterns has been examined, in relation to propagating pulses [130, 123, 83], to the dynamics of CGL spirals [170] and 3D scroll ring structures [96]. Concerning the vortex motion in noisy media, different behaviors have been addressed depending on the nature of the fluctuations. In this venue an oscillatory reaction-diffusion system with a structured disordered periodic forcing has been analyzed in [83]. The authors considered both quenched and time-varying disorder (updated on a time scale multiple of the forcing period) which gave rise to an irregular stop-start motion caused by pinning and depinning events and to a noisy flower-like trajectory. In the later case, the mean-square displacement of the spiral core shows a periodic behavior with time, with period equal to the mean period of rotation of the spiral. In the same context of a reaction-diffusion model but with excitable dynamics and space-time white Gaussian fluctuations, García-Ojalvo *et al.* [169] observed a slow meandering of spiral cores which eventually drift to the boundaries where they disappear. A similar dynamics due to noise has been observed and analyzed in [170] within the framework of the CGL equation. The authors start from an initially stable spiral wave of the CGL in the absence of fluctuations. The spiral core under a weak additive white noise performs a Brownian motion characterized by a diffusion constant which increases linearly with noise strength.

Through this chapter, we will study the effect of a spatiotemporally correlated structured noise on the motion of a spiral wave in the photosensitive BZ reaction [95]. In Section 5.2 the tip dynamics under simple homogeneous and periodical conditions is addressed. In Section 5.3 the random motion of the spiral tip will be described qualitatively as a function of the correlation time and characterized through the time dependence of the mean-square displacement of the spiral core. The diffusion coefficient is quantitatively analyzed for spatially uniform and spatiotemporal varying fluctuations in Section 5.3.1. The analysis is completed by proposing in Section 5.4 a simple theoretical model based on a kinematic approach [157], capturing the basic features observed in experiments and numerical simulations.

5.2   Tip Motion. Periodical Forcing

The dynamical behavior of a spiral wave in a homogeneous medium is studied following the trajectory described by its tip during rotation around the core. This motion, even in homogeneous conditions, can be very complex [171, 172] depending on the excitability of the medium and on the presence of a boundary.

Rigid rotation is the simplest regime of spiral wave motion. The spiral wave rotates around a circular core with a constant angular velocity and the shape of the wave front does not change with time, as it is shown in Fig. 5.1(a) overlaying the contours of the spiral wave at two different times. A kinematical description of this motion based on the eikonal equation is given in Appendix A.

Rigid rotation is characteristic to the highly excitable medium. As the excitability is decreased, the spiral tip starts to meander and its motion changes to quasiperiodic *cycloidal rotation* [171]. This compound rotation is characterized by two frequencies which define the tip motion around a core with radius R_1 and around another circle with radius $R_2 > R_1$, giving rise to a trajectory composed of a certain number of lobes or petals. Such trajectories are usually called *flower patterns*. In Fig. 5.1(b-d) three kinds of trajectories, from circular to five lobed pattern, are plotted corresponding to different values of the parameter f in the Oregonator model. The motion becomes more complex for lower excitabilities, consisting of irregular or even chaotic trajectories.

In order to follow the trajectory of the spiral tip, it is necessary to locate the tip during its motion. Numerically, the method used to compute the tip is described in [171] where the tip is defined as the point of maximum cross product of u and v gradients, where u and v are the variables of the Oregonator model (Section 2.4).

```
pmax=-100000
idif=0
iold=itip_cw        /Store the previous position
jold=jtip_cw        /of the tip
if(itip_cw.lt.25.or.itip_cw.gt.nx-25.or.
   jtip_cw.lt.25.or.jtip_cw.gt.ny-25) then
   write(*,*) 'The tip is close to the boundary'
   stop
endif
iini=itip_cw-xsearch
```
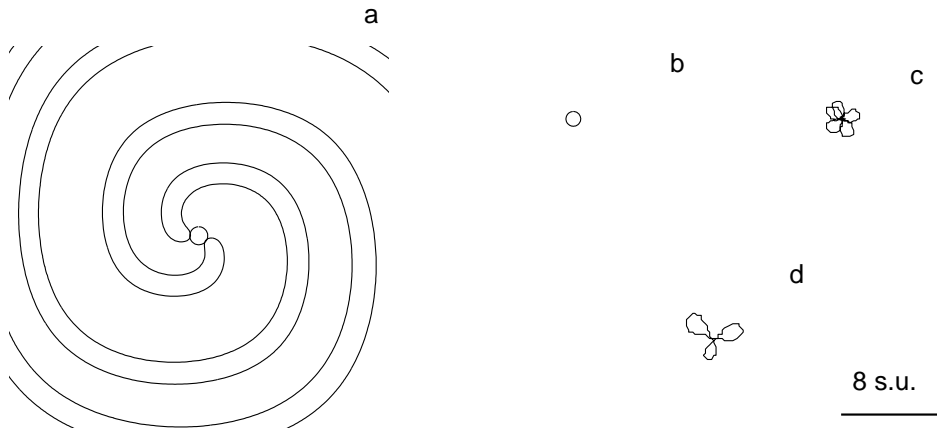
Figure 5.1: Trajectories of the spiral tip for different excitabilities of the medium. These trajectories were obtained with the Oregonator model varying the parameter f: (a) and (b) $f = 1.4$, (c) $f = 2$, (d) $f = 3$. Rest of parameters: $\varepsilon = 0.01$, $\phi = 0$, $q = 0.002$, $D_u = 1$, $D_v = 0.6$, $h = 0.16$, $\Delta t = 0.001$.

```
ifin=itip_cw+xsearch
jini=jtip_cw-ysearch
jfin=jtip_cw+ysearch    /Coordinates of the rectangular
do  i=iini,ifin         /region of search
do  j=jini,jfin
    dudx=u(i+1,j)-u(i-1,j)
    dudy=u(i,j+1)-u(i,j-1)      /Partial derivatives
    dvdx=v(i+1,j)-v(i-1,j)      /of variables u and v
    dvdy=v(i,j+1)-v(i,j-1)
    if(abs(dudx)+abs(dudy)+abs(dvdx)+abs(dvdy).ne.0.) then
        p=dudx*dvdy-dudy*dvdx       /Cross product of
        if(p.gt.pmax) then          /u and v gradients
            pmax=p
            itip_cw=i
            jtip_cw=j
        endif
    endif
enddo
```
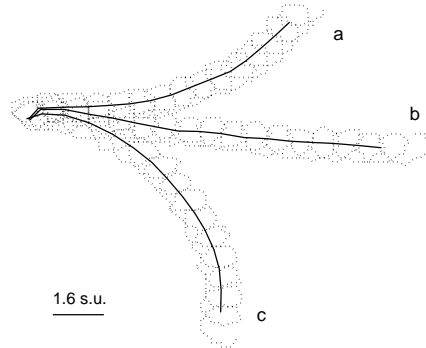
Figure 5.2: Tip trajectories measured for three different periods T_f of sinusoidal forcing of the parameter ϕ. The solid line represents the core motion. Modulation periods (a) $T_f = 1.71$, (b) $T_f = 1.7325$, (c) $T_f = 1.75$. The model is the same as in Fig. 5.1 and $f = 1.4$, $\phi_0 = 0.01$, $A = 0.003$ (amplitude of the modulation).

```
enddo
idif=idif+ abs(itip_cw-iold)+abs(jtip_cw-jold)
```

If the actual tip position changed with respect to the previous step, that is, $\mathtt{idif} \neq 0$, the coordinates of the spiral tip are stored in a vector. This algorithm works for clockwise rotation, whereas minor changes should be make in case of anticlockwise rotation (the cross product changes its sign and we are looking for the minimum).

The angular velocity and the curvature of the tip trajectory depend on the parameters of the medium. Hence, if the parameters of the system (light intensity, chemical concentrations) change, the spiral tip will follow a new trajectory with a slightly displaced center of motion. If the parameters are periodically modulated, which is the simplest way to externally force the medium, the small variations of the trajectory that occur during each period of the modulation will be accumulated in time. This causes the tip to follow a trajectory which differs significantly from the corresponding homogeneous situation and which depends on the modulation period. This is shown in Fig. 5.2 for three different periods of modulation which give rise to different resonance drifts of a spiral wave. The cores follow circular paths (solid lines) characterized by specific radii R_c. As the frequency of the external force approaches the natural frequency of rotation of the unperturbed spiral (full resonance), the core center moves along a straight line (Fig. 5.2b).

5.3   Brownian Motion. Colored Gaussian Noise

So far we have introduced the dynamics of the spiral wave in various deterministic situations such as a simple homogeneous case and the motion under periodical forcing. From now on, our concern will be the study of the spiral dynamics in fluctuating media, both spatially homogeneous and structured, subjected to a colored Gaussian temporal modulation introduced in Section 2.3.2.b.
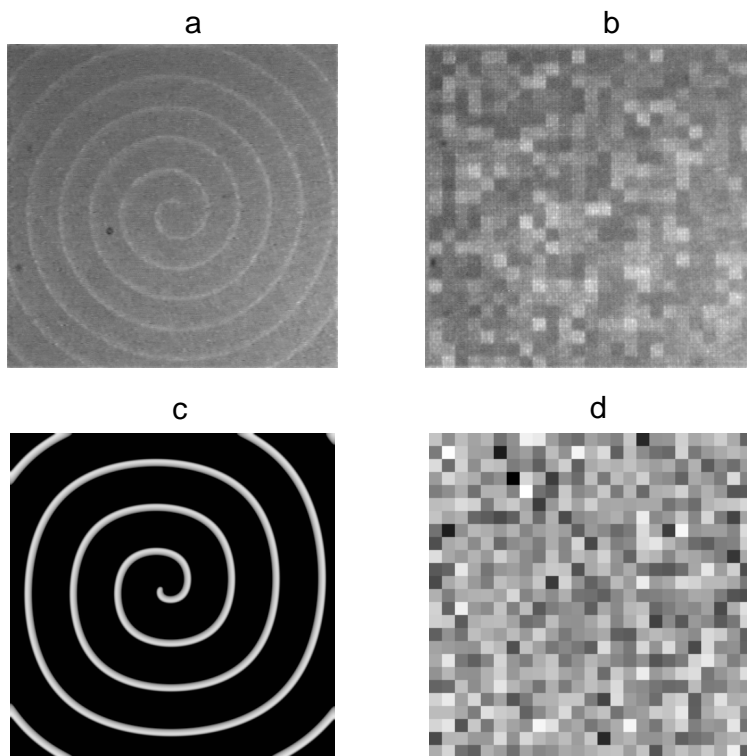
Figure 5.3: Experimental (a) and numerical (c) initial conditions consisting in a fully developed spiral wave. (a) wavelength $\lambda = 0.27$ cm, period $T = 45$ s, core size $d = 0.11$ cm, (b) $\lambda = 9.6$ s.u., $T = 1.69$ t.u., $d = 3.2$ s.u. Experimental (b) and numerical (d) characteristic patterns of fluctuating illumination. (b) $\ell = 0.9$ mm, $I_0 = 0.28$ mW cm^{-2}, (d) $\ell = 3.2$ s.u., $\phi_0 = 0.01$. Any cell in the array fluctuates around the same mean value and with a temporal autocorrelation of the exponential type.

As a first step in examining the effects of spatiotemporal noise on spiral dynamics we report on a series of experiments conducted with fixed cell size ℓ, which essentially measures the spatial correlation of the fluctuations
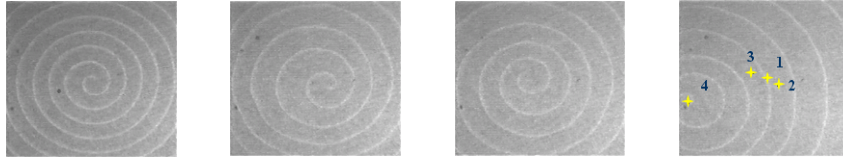
Figure 5.4: Sequence of snapshots at 0, 15, 30, and 45 min of the motion of a spiral wave under the effect of spatiotemporal fluctuations (noise-free images). The positions of the tips of the whole sequence were marked in the last image with the labels 1,2,3 and 4.

and which is assumed to always be comparable to or larger than the size of the spiral core. In each series we vary the correlation time, τ, keeping the noise dispersion, σ^2, constant (refer to Section 2.3.2.b for the meaning of the noise parameters). For the sake of comparison, a set of experiments and numerical simulations has also been performed with pure temporal noise (i.e. corresponding to the limit of infinite ℓ).

Experiments started with the generation of a free end in a square lattice of 2.5 cm $\times$ 2.5 cm size by inhibiting one half of a planar wave. After 5 minutes under uniform illumination, the medium was covered with a fully developed spiral of approximately nine wave lengths as shown in Fig. 5.3 and subjected to an illumination pattern of structured noise with Gaussian random values at each cell.

Numerically, we used the two-variable Oregonator model modified to include the effect of the light intensity on the Ru-catalyzed BZ reaction defined by the equation. (2.18)- (2.18). These equations were numerically integrated using an Euler method with a time step of 10^{-3} t.u. and a grid size of 0.16 s.u. in an array of 500 $\times$ 500 points with zero flux boundary conditions. The tip coordinates of the spiral (see Fig. 5.3) were tracked following the point where the cross product of u and v gradients was maximal (Section 5.2). For each value of τ, approximately one hundred trajectories were simulated to reduce statistical dispersion.

The experimental and numerical initial states were selected in such a way that in the absence of randomness, the spiral tip rotated quasi-rigidly around its core, with no net translational mobility. After the fully developed spiral wave was subjected to Gaussian fluctuations its core started to wander. This motion is pictured in Fig. 5.4, where the spiral follows an erratic path. In the absence of fluctuations, the sequence would be a repetition, except for a different phase, of the same initial state represented by the first image. The Doppler effect in the wave train due to the motion
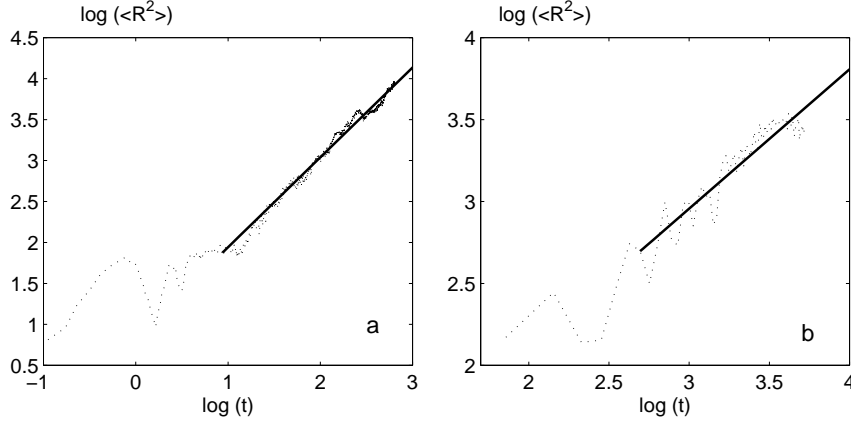
Figure 5.5: Logarithmic plots of numerical (a) and experimental (b) data of the tip dispersion averaged from 12 and 5 runs respectively. The best fit straight line has the slope 1.096 in (a) and 0.85 in (b).

of the core is also noticeable in this case.

This wandering was found to be of the Brownian diffusion type by calculating the mean-square displacement at long times. This squared dispersion follows a linear time dependence, signature of Brownian motion:

$$\langle R^2 \rangle = \langle [\mathbf{r}(t) - \mathbf{r}(0)]^2 \rangle = 2dDt \tag{5.1}$$

with $d = 2$ for the two-dimensional case, D the diffusion coefficient and $\mathbf{r}$ the position vector of the spiral tip. If we take the logarithm at both sides of Eq. (5.1), we obtain a linear equation $y = x + b$ with $y = \log \langle R^2 \rangle$, $x = \log t$, and $b = \log 2D$. In Fig. 5.5(a), the logarithm of the mean-square displacement for a set of twelve numerical trajectories obtained for $\tau = 1.5$ t.u. is shown as a function of the logarithm of time and the same is done for the experimental data for $\tau = 1$ s in Fig. 5.5(b). Skipping the initial points which correspond to a transient dynamics, the data fit well to a straight line of slope 1 in both cases, thus confirming the diffusive nature of the core motion.

The qualitative effect of τ on the Brownian motion of the spiral is illustrated in Fig. 5.6. Both experimentally (a-c) and numerically (d-f) it is found that its mobility largely depends on τ. For values of τ smaller, (Fig. 5.6(a,d)), and greater, (Fig. 5.6(c,f)), than $\tau = T/2\pi$, T being the rotation period, the trajectories are confined to a reduced part of the whole medium. On the contrary, for τ around $T/2\pi$, (Fig. 5.6(b,e)), trajectories span over a larger region reaching the boundary where the spiral finally
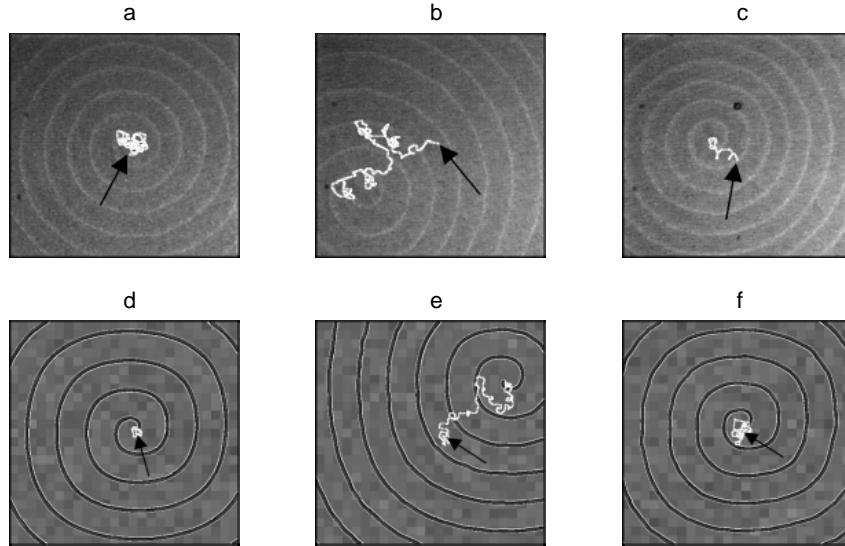
Figure 5.6: Superimposition of the final spiral state and the whole trajectory of the tip for three different values of τ obtained experimentally (a-c) and numerically (d-f). In the experiment, the noise pattern was updated at 700 ms intervals and was interrupted during 50 ms every 35 s in order to capture a noise-free image of the wave activity. (a) $\tau = 1$ s, (b) $\tau = 35$ s, (c) $\tau = 100$ s, (d) $\tau = 1$ t.u., (e) $\tau = 20$ t.u. and (f) $\tau = 100$ t.u. The arrow indicates the initial position of the tip. Experimentally, same parameters as in caption of Fig. 5.3 and concentrations 0.18 M KBr, 0.33 M malonic acid, 0.39 M NaBrO$_3$, 0.50 M H$_2$SO$_4$, and 0.71 mM Ru(bpy)$_3^{+2}$. Numerically, $\phi_0 = 0.01$, $\varepsilon = 0.01$, $f = 1.4$, $q = 0.002$, $D_u = 1$, $D_v = 0.6$, $\sigma = 0.0033$, $\ell = 3.2$ s.u.

dies out.

In the next sections, a quantitative study of this phenomenon will be shown, in terms of an effective diffusion coefficient calculated from the tip mean square displacement by averaging over many trajectories at long times.

5.3.1 Quantitative Results for the Core Dispersion

Before quantitatively studying the response of a spiral wave to the most complicated scenario of a spatiotemporal external noise, we consider fluctuations modeled as pure temporal (spatially uniform) noise for the sake of comparison. As addressed in the previous section, we report quantitative measures on spiral wave dispersion based on series of numerical and experimental realizations corresponding to a fixed value of ℓ (the spatially uniform case would correspond to the limit of infinite ℓ) which
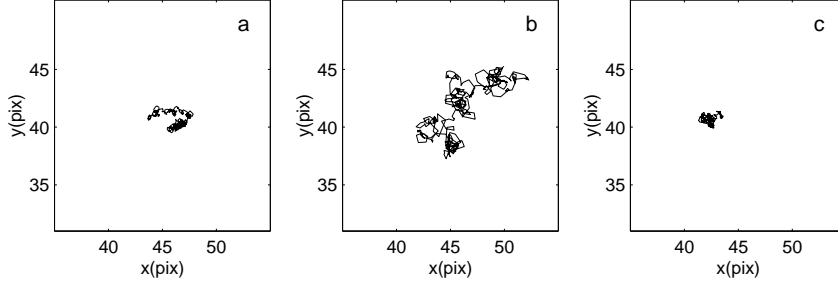
Figure 5.7: Typical paths followed by the spiral core under the effect of random fluctuations for three values of the correlation time. (a) $\tau = 0.01$ t.u, (b) $\tau = 0.27$ t.u, (c) $\tau = 10$ t.u. Rest of parameters the same as in Fig. 5.6.

is larger than or comparable to the spiral core. In each series we varied the correlation time τ while keeping the noise dispersion σ^2 constant. Representative trajectories of the core motion forced with spatially uniform noise are shown in Fig. 5.7 for different correlation times.
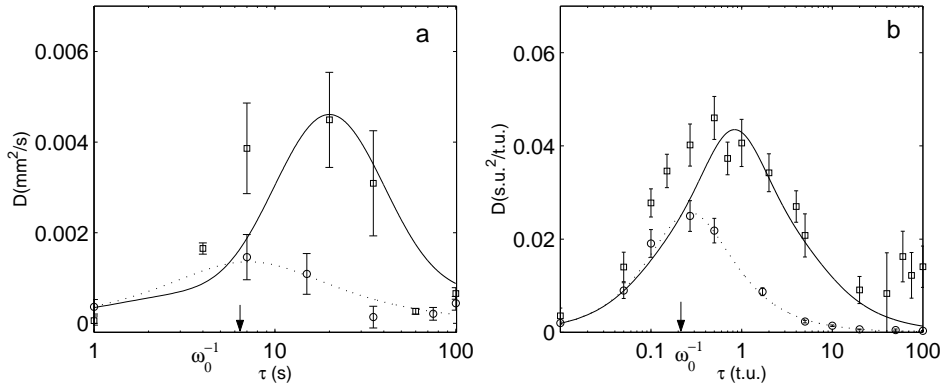
Figure 5.8: Effective diffusion coefficient versus noise correlation time τ. Continuous (spatiotemporal noise case) and dotted (temporal noise case) lines correspond to the fits of the analytical results given in Section 5.4. (a) Experimental results with parameters as in Fig. 5.3. Parameter values for the pure temporal case ($\circ$) are: $\sigma^2 = 0.00076$, $\omega_0 = 0.14$. Parameter values for the spatiotemporal case ($\square$) are: σ^2, ω_0 as before and $\frac{\bar{V}_0}{\omega_0 \ell} = 4$, $a = 400$. (b) Results for the Oregonator model with parameters of Fig. 5.6, except $\ell = 6.4$ s.u. Parameter values for the pure temporal case ($\circ$) are: $\sigma^2 = 0.38$, $\omega_0 = 3.7$. Parameter values for the spatiotemporal case ($\square$) are: σ^2, ω_0 as before and $\frac{\bar{V}_0}{\omega_0 \ell} = 1$, $a = 0.7$. Error bars associated to the statistics of the experimental and numerical data are depicted.

Quantitative results for the spatially uniform case are displayed in Fig. 5.8 as circles. A resonance-like behavior with the time scale of the noise is present both experimentally Fig. 5.8(a) and numerically Fig. 5.8(b). Even more, the resonant correlation time matches the characteristic time scale of the spiral rotation parameterized by the inverse of its rotation frequency $\tau_{res} \approx \omega_0^{-1} = T_0/2\pi$.

The resonant effect on the diffusion coefficient implies larger regions visited by the spiral core in its wandering for a range of correlation times close to the intrinsic rotation frequency of the spiral (see Fig.5.7(b)). We can conjecture a physical interpretation of the shown dependence of the diffusion coefficient on τ: at fixed noise dispersion σ^2 the effect of random perturbations is irrelevant for $\tau \to 0$ since fast bounded fluctuations will be averaged out by the system (Fig.5.7(a)). On the other hand for $\omega_0\tau \gg 1$, the spiral core loses mobility because the noise does not change appreciably during a rotation period of the tip (Fig.5.7(c)). Uniform noise fluctuations are more effective if varying in a time scale close to the characteristic time of the system.

When structured noise is externally introduced, the tip wanders through cells of different excitabilities which fluctuate independently around the same mean of excitability. A set of representative trajectories are depicted in Fig. 5.9 for three different correlation times of the fluctuating field chosen in such a way that the different modes of propagation were clearly exhibited. The quantitative results are shown in Fig. 5.8. In this more complex case of spatiotemporal random excitability, absolutes values of the dispersion coefficient are even larger than in the situation of spatially uniform fluctuations, featuring again a maximum which appears at larger values of the correlation time. Now the dispersion is enhanced due to the existence of a finite spatial correlation.

5.4   Analytical Approach

In order to gain some theoretical insight, we use a kinematical approach to 2d-spiral waves for weakly excitable media [157] with the basic equations reproduced in the Appendix A. Although our experiments fall beyond that limit, such a description enables us to capture, at least qualitatively, what we believe are the essential features of the effect of structured noise on well-formed spirals. For simplicity, we restrict the standard scheme A.15 to a situation with constant angular velocity ω_0 and retain the equations for the tip position, together with the relaxation dynamics of the instantaneous
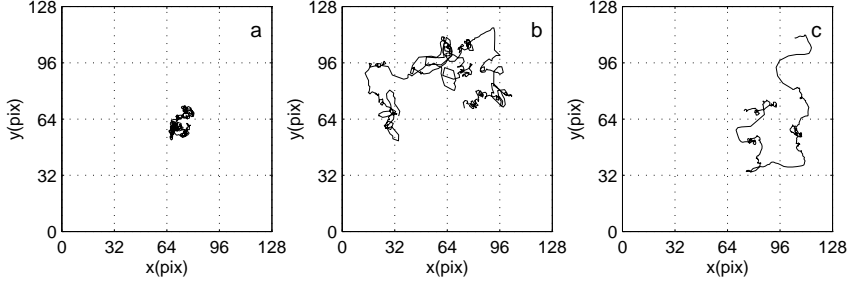
Figure 5.9: Typical paths followed by the spiral core under the effect of structured random fluctuations time correlated for three values of the correlation time and $\ell = 5.2$ s.u. (32 grid points) (a) $\tau = 0.01$ t.u., (b) $\tau = 3.2$ t.u, (c) $\tau = 30$ t.u. Rest of parameters the same as in caption of Fig. 5.6.

curvature of the spiral at its free end,

$$
\begin{aligned}
\frac{dX}{dt} &= -V_0 \sin \omega_0 t - G \cos \omega_0 t \\
\frac{dY}{dt} &= V_0 \cos \omega_0 t - G \sin \omega_0 t \\
\frac{dk}{dt} &= -\frac{1}{\tau_G}(k - k_c)
\end{aligned}
\tag{5.2}
$$

where the curvature correction to the normal velocity V was assumed negligible ($Dk \ll V_0$), so that V reduces to V_0 (a parameter which depends on the excitability and represents the characteristic propagation velocity of uncurved waves).

Within the kinematic approach, it seems more natural to consider fluctuations of V_0, the tip velocity normal to the wave front, and/or the critical curvature k_c. Let us start with the simplest situation corresponding to $V_0(\mathbf{r}, t) = \bar{V}_0 + \xi(\mathbf{r}, t)$, but with no tangential velocity ($G = \gamma(k - k_c) = 0$) of the free end (no sprouting or contraction of the spiral curve): $k_c(t) = k_c = k_0$ which represents the particular solution of rigid rotation. Within the spirit of the quasistatic approximation, implicit in the kinematic scheme above, the spatial structure of the noise will only enter through the successive positions visited by the wandering tip. Due to the complexity of the stochastic kinematic equations, an exact analytical approach cannot be accomplished exactly so we introduce a 'quasideterministic' approximation by defining effective spatial dependent noises as $\xi(\mathbf{R}(t), t)$ where $\mathbf{R}(t)$ stands for the tip deterministic trajectory, which in our case corresponds

to a circular motion with frequency ω_0 of an unperturbed steadily rotating spiral.

Before going further, it is necessary to specify the way the discrete spatial nature of the noise in the experiments is translated to the analytical kinematic scheme. Temporal and spatial correlations are bound to be statistical independent in the experiments and numerics, that is:

$$< \xi(\mathbf{r}, t)\xi(\mathbf{r}', t') > = C_\xi(\mid t - t' \mid)C(\mathbf{r} - \mathbf{r}') \tag{5.3}$$

The temporal part, C_ξ should be replaced by $\sigma^2 \exp^{-|t-t'|}/\tau$ (Eq. (2.33)). An immediate solution for the spatial correlation is to adopt a triangular-like form which accounts for the anisotropy of the problem of structured noise, i.e.:

$$C(\mathbf{r} - \mathbf{r}') = \left(1 - \frac{\mid x - x' \mid}{\ell}\right)\left(1 - \frac{\mid y - y' \mid}{\ell}\right) \tag{5.4}$$

This correlation function is anisotropic and the calculations become very complicated using it. A simpler option is to resort to an isotropic correlation function of the form:

$$C(\mathbf{r} - \mathbf{r}') = \left(1 - \frac{\mid \mathbf{r} - \mathbf{r}' \mid}{\ell^2}\right) \tag{5.5}$$

This correlation function is expected to give qualitatively similar results making at the same time the analytical treatment easier. We conjecture that the problem becomes isotropic for sufficiently large times and lengths, where the local topology of the system becomes irrelevant.

Let us first address the situation of spatially uniform noise, considering only fluctuations in the normal velocity, $V_0(t) = \bar{V}_0 + \xi(t)$, and a steady rigid rotation ($\omega = \omega_0$, $k = k_c$),

$$\begin{aligned}
\frac{dX}{dt} &= -[\bar{V}_0 + \xi(t)]\sin\omega_0 t \\
\frac{dY}{dt} &= [\bar{V}_0 + \xi(t)]\cos\omega_0 t
\end{aligned} \tag{5.6}$$

The explicit calculation of the diffusion coefficient can then be calculated

exactly[1] as is shown in [173]. The tip position can be expressed as $Z = X + iY$ and the evolution equations (5.6) as:

$$\frac{dZ}{dt} = [\bar{V}_0 + \xi(t)]ie^{iw_0 t} \tag{5.7}$$

which can be analytically integrated to give,

$$Z(t) - Z(0) = \frac{V_0}{w_0}e^{iw_0 t} + i\int_0^t \xi(t')e^{iw_0 t'}dt' \tag{5.8}$$

For the case of a Brownian diffusion, the mean-square dispersion as a function of the complex quantity Z looks like $<\mid Z(t) - Z(0) \mid^2> = 2dDt$ (see Eq. (5.1)) since $\mid Z \mid^2 = X^2 + Y^2$. Hence, the diffusion coefficient is given by,

$$\begin{aligned} 2dD &= \left\langle \frac{d \mid Z(t) - Z(0) \mid^2}{dt} \right\rangle_{t\to\infty} \\ &= 2Re\left(\left\langle \frac{d(Z(t) - Z(0))}{dt}(Z^* - Z(0))\right\rangle\right)_{t\to\infty} \end{aligned} \tag{5.9}$$

The calculation of D requires the evaluation of the average of the right-hand side. From now on, we are going to write the $Z(t) - Z(0)$ as simply $Z(t)$. By substituting the expressions for dZ/dt and Z^*, taking averages and rearranging terms, we have:

$$Re\left(\left\langle \frac{dZ}{dt}Z^* \right\rangle\right)_{t\to\infty} = \int_0^\infty <\xi(t)\xi(t')> cos\left[\omega_0(t-t')\right]dt' \tag{5.10}$$

By noting that $<\xi(t)\xi(t')> = C(\mid t - t' \mid)$, Eq. (5.10) is simply the power spectrum of the noise at the characteristic frequency of the rotating spiral

$$P(w_0) = 2\int_0^\infty C(t)\cos(\omega_0 t)dt \tag{5.11}$$

Thus, the final expression for the diffusion coefficient reads

$$D = \frac{1}{4}P(w_0) \tag{5.12}$$

that is, it is given exactly in terms of the power spectrum of the noise [173] at the natural frequency of the spiral. The problem is thus reduced to the

---

[1]Numerical simulations of the kinematic scheme described by Eqs. (5.2) have been systematically carried out in [173] together with a more thorough analytical treatment of the problem.

computation of such power spectrum for the temporal noise defined above Eq. (2.33), resulting in:

$$D = \frac{\sigma^2}{2} \frac{\tau}{1 + w_0^2 \tau^2} \tag{5.13}$$

Good agreement is obtained between the experimental and numerical points of Fig. 5.8 and this analytical prediction (dotted lines). This simple model captures the resonance at the characteristic time scale of the spiral rotation (w_0^{-1}).

For the structured case we can proceed in a similar way except now we focuss on the spatial correlation function. Using the quasideterministic circular trajectory $(w = w_0$ and $G = 0)$, $X = \frac{V_0}{w_0} \cos \omega_0 t$, $Y = \frac{V_0}{w_0} \sin \omega_0 t$ to calculate the distance between tip positions at times t and t' we obtain:

$$| \mathbf{R}(t) - \mathbf{R}(t') |^2 = 2\frac{V_0^2}{\omega_0^2} \left[1 - \cos \left(\omega_0(t - t') \right) \right] \tag{5.14}$$

The isotropic spatial correlation function (Eq. (5.5)) assumes the form of

$$C(| \mathbf{r} - \mathbf{r}' |) = 1 - 2\frac{V_0^2}{\omega_0^2} \left[1 - \cos \left(\omega_0(t - t') \right) \right] \tag{5.15}$$

Again, we have to calculate the averaged quantity $< \frac{dZ}{dt} Z^* >$, where now

$$\frac{dZ}{dt} = [V_0 + \xi(Z,t)]i e^{i\omega_0 t}$$

$$Z^*(t) = \frac{V_0}{\omega_0} e^{i\omega_0 t} + i \int_0^t \xi(Z,t') e^{i\omega_0 t'} dt' \tag{5.16}$$

After substituting these identities, the diffusion coefficient appears as:

$$
\begin{aligned}
D &= \frac{1}{4} \left\langle 2\frac{dZ}{dt} Z^* \right\rangle_{t \to \infty} \\
&= \frac{1}{4} \int_0^\infty 2 < \xi(Z,t)\xi(Z,t') > \cos \left(\omega_0(t - t') \right) dt' \\
&= \frac{1}{4} \int_0^\infty 2C(| t - t' |)C(\mathbf{r} - \mathbf{r}') \cos \left(\omega_0(t - t') \right) dt' \\
&= \frac{1}{4} \int_0^\infty dt\, 2\, C(t) \cos \left(\omega_0 t \right) \left(1 - \frac{4V_0^2}{\omega_0^2 \ell^2} \frac{1}{2} + \frac{4V_0^2}{\omega_0^2 \ell^2} \frac{1}{2} \cos \left(\omega_0 t \right) \right)
\end{aligned}
\tag{5.17}
$$

Taking into account Eq. (5.11), the diffusion coefficient can thus be expressed as a function of the power spectrum of the noise at the characteristic frequency and multiples of this frequency

$$D = \frac{P(\omega_0)}{4} + \frac{V_0^2}{4\omega_0^2 \ell^2}(P(0) - 2P(\omega_0) + P(2\omega_0)) \qquad (5.18)$$

where the trigonometric relation $2\cos^2 \omega_0 t = 1 + \cos 2\omega_0 t$ has been used. Substitution of the power spectrum of the Ornstein-Ulhenbeck noise, Eq. (5.18)

$$D = \frac{\sigma^2}{2} \frac{\tau}{1 + \omega_0^2 \tau^2} + \frac{\sigma^2}{2} \frac{V_0^2}{\omega_0^2 \ell^2} \left(\tau - \frac{2\tau}{1 + \omega_0^2 \tau^2} + \frac{\tau}{1 + 4\omega_0^2 \tau^2} \right) \qquad (5.19)$$

This final expression describes the special case of pure temporal noise, that is, $\frac{\bar{V}_0}{\omega_0 \ell} \ll 1$, *i.e.* core radius much smaller than the noise correlation length, recovering the behavior shown in Eq. (5.13). In the parameter region where $\frac{\bar{V}_0}{\omega_0 \ell} \sim O(1)$, D is significantly enhanced, particularly near resonant conditions. This is again in accordance with the experimental and numerical observations in Fig. 5.8. However, Eq. (5.19) predicts an artificial linear increase of D at large τ. The basic limitation of the quasideterministic ansatz which leads to Eq. (5.19) lies in the fact that the deterministic trajectory is closed. This introduces spurious effects at large correlation times of the noise since, for $\omega_0 \tau \gg 1$, the values of the effective noise seen by the tip appear strongly correlated after every rotation period. In fact, the actual trajectory is not closed and decorrelates the effective noise by exploring spatially uncorrelated regions.

Nevertheless, the model can be formally corrected for this effect by introducing an additional time scale τ^*, a cutoff of the correlation times, which accounts for the above spatial decorrelation. This parameter can be interpreted as the time needed for the tip to cross over a pixel. To justify this additional parameter we have to take into account a crucial ingredient that has been missing so far: the role of fluctuations in k_c [2]. Numerical simulations of Eq. (5.2) carried out by Alonso & Sagués in [173] show a rather different behavior at values of $\tau \simeq T_0$, depending on whether noise is introduced only through V_0 or on both V_0 and k_c giving rise to two different modes of dispersion. Without noise on k_c, there is a tendency of the tip motion to attach its quasicircular motion to the boundaries between

---

[2] According to complementary simulations of the kinematic scheme and Oregonator model, fluctuations in V_0 and k_c are assumed to be proportional [173]

cells and propagate along them (see Fig. 5.9(b)). On the contrary when noise is added also through k_c this effect is avoided, the tip being confined most of the time inside the cells except for relatively fast transits between them. We recognize this as a signature of a pinning effect, as is indeed also evidenced by experiments and numerical treatment of the Oregonator model at large values of τ (Fig. 5.9(c)). According to this mechanism, the pinning effect enables us to interpret the asymptotic decay of D for large τ of the form $D \sim 1/\tau$ shown in Fig. 5.9(c). For large τ, this pinned motion drastically reduces dispersion, which will be more effective for larger values of the correlation length as the tip anchoring will last longer. For smaller values of ℓ, the tip has more opportunities to move across the boundaries of the noisy cells, giving rise to an enhancement of the dispersion. This functional dependence can be incorporated into our scheme for $\frac{\bar{V}_0}{\omega_0 \ell} \sim O(1)$, by defining $\tau^* \equiv a/\tau$ and further replacing τ by τ_{eff} $(1/\tau_{eff} \equiv 1/\tau + 1/\tau^*)$ in Eq. (5.19).

Comparisons of this theory with the experimental and numerical results are shown in Fig. 5.8 (continuous lines). The good agreement between the analytical prediction Eq. (5.19) [3] (with the appropriate τ_{eff}), and both experiments and numerical integration of the Oregonator model, for a very large range of parameters, suggests that the proposed model , in spite of its apparent simplicity, does capture the basic physical mechanisms of the problem.

5.5   Conclusions

We have studied both experimentally and numerically the effect of a spatiotemporal structured noise on the motion of a spiral wave within the framework of the photosensitive BZ reaction. In the absence of randomness, the spiral tip rotates quasi-rigidly around its core, with no net translational mobility. When the noise is switched on, Brownian diffusion of the spiral is observed, characterized by a nonmonotonous dependence on the parameters of the noise. Specifically, experiments conducted with fixed noise dispersion and varying the correlation time for pure temporal fluctuations yield a resonance-like effect on the diffusion coefficient when the correlation time matched the intrinsic rotation frequency of the spiral. When structured noise is added to the system, the diffusion coefficient becomes even greater,

---

[3]To circumvent somehow the limitations of the kinematic approach as applied here in relation to the real experimental parameters, we choose to consider the dimensionless quantity $\frac{\bar{V}_0}{\omega_0 \ell}$ in Eq. (5.19) as a fitting parameter.

especially for correlation longer times. These observations were confirmed numerically using the two-variable Oregonator model and the analysis was completed by using a simple theoretical model based on a kinematic approach which captures the basic features observed in experiments.

Chapter 6

Regular Wave Propagation Out of Noise

Abstract. *A pacemaker, regularly emitting chemical waves, is created out of noise when an excitable photosensitive Belousov-Zhabotinsky (BZ) medium, strictly unable to autonomously initiate autowaves, is forced with a spatiotemporal patterned random illumination. These experimental observations are also reproduced numerically by using the Oregonator model, and further analytically interpreted in terms of genuine coupling effects arising from parametric fluctuations. Within the same framework we also address situations of noise sustained propagation in subexcitable media.*

6.1   Introduction

Since their discovery thirty years ago [13], target patterns constitute one of the most distinctive and visually compelling examples of self-organization in chemical systems. Somewhat more general, control on wave initiation and propagation may have a wealth of potential implications not only for chemical [174, 39, 33] or biochemical systems [175, 3] but extending to cardiology [176] or neurophysiology [4] contexts. Although unavoidably present in any realistic situation of these scenarios, the minimization of noise and disorder is always pursued under the rationale that their effects may if not destroy, at least largely mask, the intrinsic spatiotemporal regularities of any such wave propagation phenomena. But there exist numerous experimental and numerical examples of just the opposite, the beneficial role that noise may play in some unfavorable situations where no structures can propagate or exist under purely deterministic conditions.

That is the case of the recent experimental finding of noise-supported waves in subexcitable chemical media [11], where sustained propagation is

achieved at an optimal amount of noise. Similar results have been obtained in the context of coupled bistable electronic elements concerning noise-level dependent signal transmission [8, 107]. With this unified perspective we highlight the specificities of these phenomenologies in relation to other celebrated noise- constructive effects, taming spatiotemporal chaos with disorder [177], noise-induced synchronization to global oscillations for arrays of excitable units [178, 106, 10], noise-induced spiral dynamics in excitable media [169, 179, 114, 113] or coherence resonance oscillators [180, 181].

Regarding the onset of new spatial structures out of noise [10, 106] it is important to highlight the mechanisms involved in such phenomena. Wave activity is spontaneously nucleated due to accumulated subthreshold perturbations in [10], while in [106] an inhomogeneous initial condition is required. Spatially uncorrelated noise seems to be more effective to sustain structures than a global noise affecting in an identical way all fluctuating lattice cells. In general, there exists a value of noise which optimizes the response of the nonlinear system, as a result of a cooperative process involving noise, nonlinearity and coupling. And finally, statistical analysis of the number and size of coherent structures arising from spatiotemporal structures present power-law scaling [10, 179, 169].

Even the experimental and numerical investigations on the study of the role of spatiotemporal fluctuations is increasing, the understanding by which noise may give rise to an ordered behavior is still deficient. The purpose of this chapter is to present experimental and numerical evidence, and also an analytical explanation, of just the beneficial influence of spatiotemporal noise [182], by showing that an excitable chemical system may rectify external fluctuations into regularly organized wave trains (Sec. 6.2) as well as to support propagation which becomes impossible in their absence (Sec. 6.3). In Sec. 6.4 a theoretical framework for activator-inhibitor models will be introduced to interpret not only this experimental finding of created targets out of noise but the recent related one of noise-supported waves in subexcitable media.

6.2 Noise-Created and Supported Target in Excitable Media

Spatiotemporal structured noise is introduced into the system by using a computer controlled and continuously evolving fluctuating patterned illumination, which is video projected (from below) on to the gel film

(Sec. 2.3.2.c). The pattern of illumination consisted of an array of square cells of linear size ℓ ($\ell = 0.44$ mm), each of them obeying a gaussian statistics ($\sigma = 0.14$ mW/cm^2) around a prescribed reference illumination value I_0 for excitable conditions ($I_0 = 0.29$ mW/cm^2). The different illumination values are reproduced through an eight-bit gray scale between 0 and 255 that is filtered by means of a video projector according to a calibration curve (Fig. 2.4). All the cells are independently updated according to the smallest time provided by the computer (100 ms), to reproduce fluctuations with extremely small correlation time (mimicking an effective white noise limit).

To assure a radial distribution of the refractory time, a central black spot ($I_0 = 0$, $R \approx 1.5$ mm) (whose size was found to be critical) was projected into the sample until a circular wave emerged from this local perturbation. Structured light fluctuations were subsequently imposed
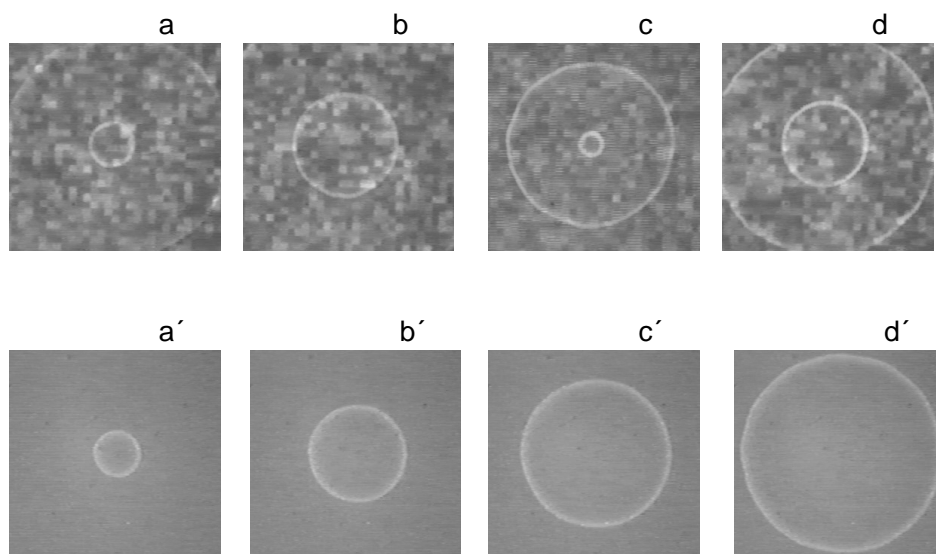
Figure 6.1: Sequence of images, (a)-(c), showing a noise-sustained target pattern in the BZ reaction. The medium is forced with a spatiotemporal fluctuating illumination. The average light intensity corresponds to excitable conditions ($I_0 = 0.29$ mW/cm^2). By comparison, images (a')-(c') correspond to a fluctuation free case with a constant and uniform illumination fixed to the averaged intensity I_0. Images shown in the figure correspond to an exposed area of 1.38×1.36 cm^2. Interval between images is 20 s. Reactant concentrations: 0.15 M KBr, 0.34 M malonic acid, 0.38 M NaBrO$_3$, 0.48 M H$_2$SO$_4$, and 1.5 mM Ru(bpy)$_3^{+2}$.
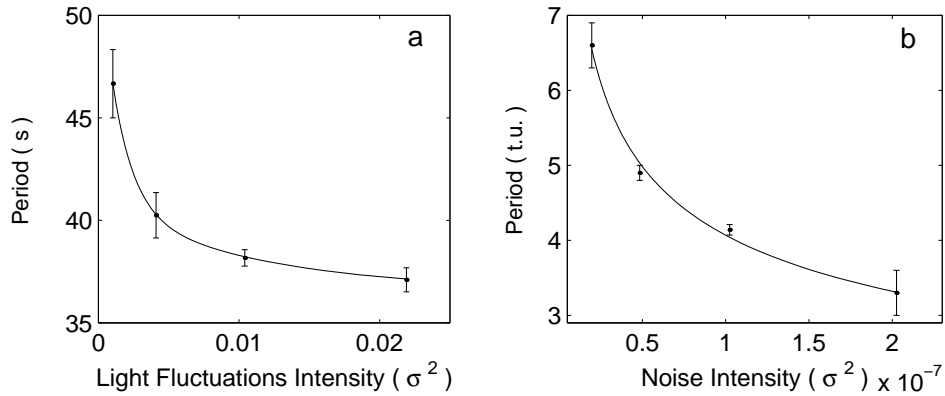
Figure 6.2: Dependence of the wave nucleation period on the noise intensity: (a) experimental results, (b) numerical results obtained from the two variable dimensionless Oregonator model. Continuous lines are simply to guide the eye. The set of numerical parameters were: $\epsilon = 0.03$, $q = 0.0015$, $f = 1$, $D_u = 1$, and $D_v = 0$. Experimental parameters are the same as in Fig. 6.1.

all over the system, and when prescribed above an intensity threshold, repeated wave nucleation, leading to a circular wave train, was observed, as shown in Fig.6.1. For the sake of comparison, we include in the same figure the case of uniform and steady illumination at the same reference value. As expected, a single autowave propagating from the initial condition is found in the absence of fluctuations.

Actually, repeated wave emission could only be sustained for an intermediate range of fluctuation intensities. For low noise level, no periodic wave emission was observed, as it is no large enough to induce new nucleations. On the contrary, under a too high noisy environment, sustained wave initiation was possible but immediately waves were continuously broken into scattered fragments progressively occupying the whole medium.

Quantitative results consisted in measuring the period of emission as a function of the noise level by averaging the time intervals between consecutive waves of the BZ reaction are summarized in Fig.6.2(a). Results reproduce a monotonous decrease of the emission period as the noise level increases. On the contrary, there exists a critical noise intensity approaching which the emission period diverges. For lower intensity fluctuations the system will stay forever under purely excitable conditions. Regarding the role of the cell size, the best results were observed when

a

b
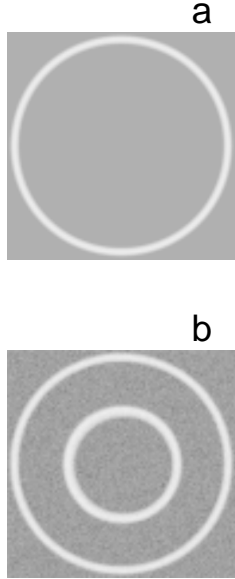
Figure 6.3: Numerical simulation showing a noise-sustained propagation (panel (b)) compared with the noise-free case (panel (a)) for the same $\phi_0 = 0.005$, $\sigma^2 = 1.4\ 10^{-4}$. Concentrations of u are represented by gray levels, higher/smaller concentration values corresponding to lighter/darker color pixels. Rest of parameters as in Fig. 6.2.

comparable to the wave width. With half this value, which corresponds to the size of an illumination pixel, waves hardly nucleated, whereas for larger sizes no waves were generated, probably due to the progressively loss of the patterned structure of the noise.

Numerical studies of noise-sustained target-like were conducted using both the complete three-variable Oregonator model (Eqs. (2.14)-(2.16)) as well as its reduced form that follows from the adiabatic elimination of the rapidly varying Br^- concentration (Eqs. (2.18)-(2.18)). Although both reproduce the experimental observations, on what follows we limit ourselves to this latter level of modelization since the theoretical considerations addressed below may widen their scope when applied to activator- inhibitor schemes and even admit in this case a fully analytic formulation. The model equations thus read,

$$
\begin{aligned}
\partial_t u &= D_u \nabla^2 u + \frac{1}{\epsilon}\left(u - u^2 - (fv + \phi)\frac{u-q}{u+q}\right); \\
\partial_t v &= u - v;
\end{aligned}
\tag{6.1}
$$

Corresponding to the experiments above, the fluctuating excitability was introduced through a random distribution of the local values of the parameter $\phi = \phi_0 + \eta(t)$. The pattern consisted of an array of square cells of

a   b
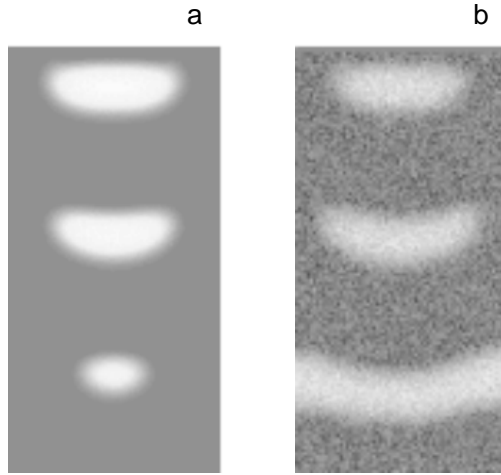
Figure 6.4: Numerical simulation showing a subexcitable / excitable transition (b) compared with the noise-free case (a) for the same $\phi_0 = 0.087$, $\sigma^2 = 1.4 \ 10^{-4}$. This images are built up from a superposition of snapshots. Rest of parameters as in Fig. 6.2.

1×1 pixels (0.2 dimensionless space units), each of them obeying a gaussian statistics around a fixed reference value ϕ_0 in the excitable range. All the cells were independently updated every time step (0.0005 dimensionless time units) to simulate uncorrelated fluctuations (white noise limit) [1] ($\langle \eta_i(t)\eta_j(t') = 2\sigma^2 C_{ij}\delta(t - t')\rangle$). The model equations were integrated in a two-dimensional rectangular grid of 320×320 pixels (unit grid size $\Delta = 0.2$) with no-flux boundary conditions.

Using initial preparations similar to those in the experiments, conditions to observe periodic wave emission were also found for an intermediate range of fluctuation intensities. This periodic emission is shown in Fig. 6.3(b) next to the equivalent homogeneous noise-free system where, after the initial perturbation, no wave activity remains in it. A series of simulations was carried out to determine the dependence of the observed periodicity of the emitted waves on noise intensity. Periods were computed from successive circular waves passing through four square symmetrically distributed points separated 150 pixels from the center position and average was taken over 2 realizations of the initial condition. The results are reproduced in Fig.6.2(b), showing similar trends to those observed in the experiments.
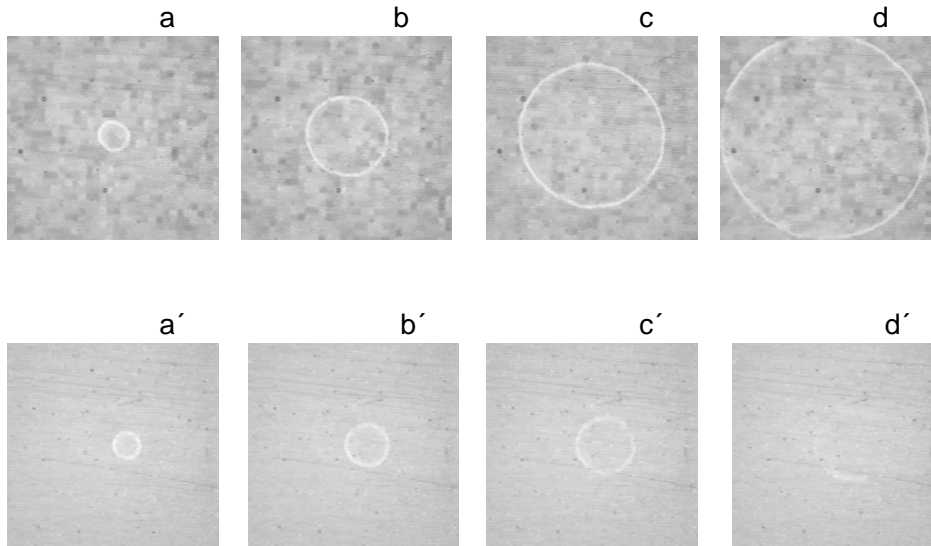
Figure 6.5: Sequence of images (a)-(d) showing a noise- mediated nonexcitable / excitable transition corresponding to a light mean intensity of $I_0 = 1.04 \ mW/cm^2$ and a light fluctuation intensity $\sigma = 0.14 \ mW/cm^2$ and $\ell = 0.44 \ mm$. (a')-(d') shows the evolution in homogeneous for the same I_0. Exposed area, $1.38 \times 1.36 \ cm^2$. Time interval between images (a)-(d), 20 s, and between images (a')-(d'), 10 s.

6.3 1D Noise-Supported Propagation in Nonexcitable Media

Before addressing the theoretical explanation of the phenomena just reported, let us show experimental results for another kind of noise-mediated transition which takes place within the region of low excitabilities, namely, the support of a 1-dimensional wave induced by noise in a nonexcitable medium. A close situation was demonstrated by Kádár et *al.* in [11] where they found noise-supported traveling waves in a subexcitable photosensitive BZ reaction. A numerical picture of that is given in Fig. 6.4. Basically, a broken wave segment (a 2-dimensional wave) propagating in a subexcitable medium shrinks and disappears (Fig. 6.4(a)). When noise is added to the medium, wave propagation is enhanced with increasing noise amplitude, and sustained propagation is obtained for an optimal level of noise (Fig. 6.4(b)) and the segment does not shrink any longer.

1-dimensional waves like circular waves are unable to be sustained in a nonexcitable but propagates in a subexcitable medium like the previous
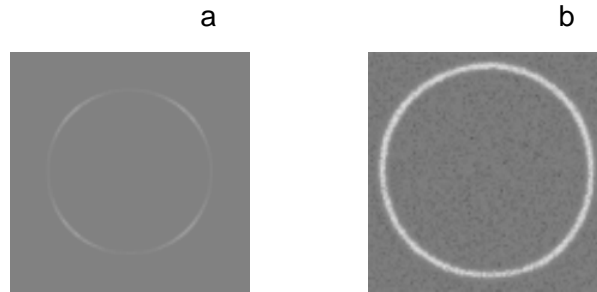
Figure 6.6: Numerical simulation showing a nonexcitable/subexcitable transition (b) compared with the noise-free case (a) for the same $\phi_0 = 0.096$, $\sigma^2 = 1.4\ 10^{-4}$. Rest of parameters as in Fig. 6.2.

one. In the same way, we have found that successful propagation is achieved when a sufficient amount of noise is introduced in the medium. Such situation is pictured experimentally in Fig. 6.5 and numerically in Fig. 6.6.

All this noise-mediated transitions presented so far can be explained within the same analytical framework through an effective deterministic model analytically derived in the next section.

6.4   Common Analytical Framework

The keystone to theoretically interpret the phenomenon just reported consists in realizing that when noise is introduced through the illumination parameter in the model equations (6.1), a random term left from the fluctuating zero mean part, enters multiplicatively into the dynamics of the activator variable (in our case the $HBrO_2$) [183] in the following way:

$$\frac{\partial u}{\partial t} = \delta \nabla^2 u + f(u, v, \phi_0) + g(u)\eta \tag{6.2}$$

being

$$f(u, v, \phi_0) = \frac{1}{\varepsilon}(u - u^2 - (fv + \phi_0)\frac{u - q}{u + q})$$

$$g(u) = -\frac{1}{\varepsilon}\frac{u - q}{u + q}$$

However due to this nonlinear coupling, a systematic genuine nonzero contribution arises when averaging such a noisy term in relation to the

dynamics of the activator variable, even η has zero mean:

$$\langle g(u)\eta \rangle \neq 0 \tag{6.3}$$

This noisy term can be evaluated using the Novikov's theorem [1],

$$\langle g(u)\eta \rangle = C(0)\langle g(u)g'(u) \rangle \tag{6.4}$$

where $C_0 = \frac{\sigma^2}{\Delta^2}$ is the spatial white noise limit.

According to this result, Eq. (6.2) can be rewritten as,

$$\frac{\partial u}{\partial t} = D_u \nabla^2 u + h(u, v, \phi_0) + \xi(u, t) \tag{6.5}$$

where $h(u, v, \phi_0) = f(u, v, \phi_0) + C_0 g'(u)g(u)$ represents a new systematic reaction term and $\xi(u, t) = g(u)\eta(t) - C_0 g'(u)g(u)$ a new (additive) noise term.

Given the finite, although small, time and length scales of the experimental fluctuations and for moderate noise intensities, one can incorporate the dominant noise contributions which correspond to the lowest order term of an expansion on these parameters ($u = u_0 + \sigma^2 u_1$) as a correction to those kinetics terms, discarding additional non systematic fluctuating terms which average to zero [184]:

$$\frac{\partial u_0}{\partial t} = D_u \nabla^2 u_0 + h(u_0) \tag{6.6}$$

$$\frac{\partial u_1}{\partial t} = D_u \nabla^2 u_1 + h'(u_0)u_1 + \xi(u_0, t) \tag{6.7}$$

Now, it can be seen that the resulting dynamics of the variable u_0 is different from that of the deterministic field. As a result we finally end up with an effective totally deterministic two variable Oregonator model whose explicit equations read

$$\partial_t u = D_u \nabla^2 u + \frac{1}{\epsilon}\left(u - u^2 - (fv + \phi_0)\frac{u - q}{u + q} \right)$$
$$+ \frac{1}{\epsilon}\left(\frac{\sigma^2}{\Delta^2} \frac{2q}{\epsilon(u + q)^2} \frac{u - q}{u + q} \right);$$
$$\partial_t v = u - v; \tag{6.8}$$
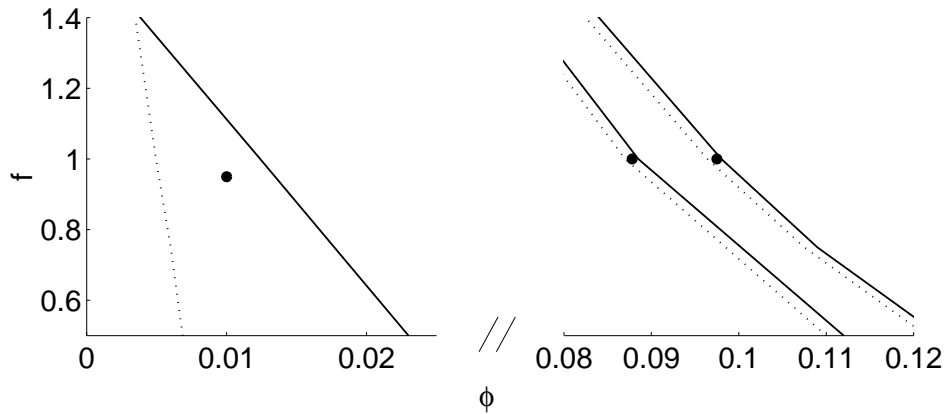
Figure 6.7: Diagram classifying the different dynamical regimes of the two-variable Oregonator model (dashed lines) Eq. (6.1) and the effective two-variable model (solid lines) Eq. (6.8). In the graph on the left the boundaries between oscillatory and excitable regimes are shown. In the graph on the right the boundaries among excitable, subexcitable (shrinking of 2d wave segments) and nonexcitable (collapse of 1d waves) conditions are shown.

in terms of the noise intensity σ^2 and the pixel size Δ. Once in this form, the excitable and oscillatory properties of such a renormalized model are easily computed. This whole procedure enables us, as shown in Fig. 6.7, to predict a noise intensity dependent shift of the boundaries separating the dynamical regimes (oscillatory, excitable, subexcitable and nonexcitable) of such an effective scheme as compared to the noise free Oregonator model. Notice that in fact such a theoretical framework enables us to interpret not only the appearance of noise-induced target patterns, but related scenarios of noise-supported wave propagation, both in subexcitable (Fig. 6.4(b)) [11] and nonexcitable conditions of Fig. 6.6(b). In other words an excitable (resp. subexcitable or nonexcitable) propagating condition in a noise free environment turns into an oscillatory (resp. excitable or subexcitable) situation when external uncorrelated spatiotemporal fluctuations of zero mean and appropriate intensities are superimposed on the illumination parameter. As a final comment, note that the whole argument just presented highlights the delicate coupling between noise and the nonlinearities of the chemical system, which, rather than resulting into new noise-induced periodicities, evoke its intrinsic "eigenvalues", both temporal (emission frequency) and spatial (period of the wave train). In this respect, this theoretical interpretation is essentially

different from those based on barrier crossing dynamics arguments, that are commonly invoked to explain the statistical periodicities observed in related stochastic resonance [107] or coherence resonance [181] phenomena in spatially extended systems[1].

6.5   Conclusions

We have provided experimental and numerical evidence, and also an analytical explanation, of the beneficial influence of spatiotemporal fluctuations, by showing that an excitable chemical system may rectify external fluctuations into regularly organized wave trains. Explicitly, we have shown that the photosensitive BZ reaction, under excitable conditions unable to create autowaves, does maintain a target structure when subjected to a patterned and continuously evolving random illumination.

---

[1]The numerical calculations included in Section 4.1 have been performed by Sergio Alonso, who has collaborated with our group during this PhD thesis.

Chapter 7

Conclusions and Outlook

Throughout this work investigation was focused on the photosensitive Belousov-Zhabotinsky reaction and its model, the Oregonator, which have been externally forced with both deterministic and fluctuating variations of their respective excitability control parameters. Waves in these systems whose kinetics are spatiotemporally modulated have been found to display new interesting phenomena not observed in homogeneous conditions. A summary of the general results of the different situations here addressed is:

A. *Spatial and Temporal Periodical Modulations.*

    A1. Boundary conditions in domains with the form of sinusoidally modulated channels may induce nontrivial longitudinal spatial configurations of a wave train of excitation fronts. These trains of fronts asymptotically accommodate in *stroboscopically frozen* quasiperiodic spatial configurations, incommensurate with the boundaries but periodic in time and synchronized with the stimuli. Both the height and position of fronts exhibit a quasiperiodic behavior that becomes more evident as the amplitude of the forcing increases. These structures were described in terms of spatial return maps which resembles the circle map of temporal forced dynamical systems. This similarity allows one to speculate about the existence of even more complex configurations representing the spatial realizations of the chaotic regimes of these maps. Finally, propagation of a wave train is possible through an undulated channel even when the width at the narrowest part of the channel is below the minimum width necessary for propagation in a straight channel.

A2. Temporal periodical modulation of excitability around a subexcitable state may give rise to sustained wave propagation, depending on the forcing parameters and initial conditions. For critical values of these constraints, the sustained propagation assumes a form where the length of the wave varies periodically with the period of the external modulation. The propagation is further enhanced by adjusting the forcing parameters such that the wave front grows in length. The propagation can be understood in terms of an interplay between the radial expansion of the wave and the motion of its free ends as the excitability varies periodically. A simple kinematic analysis provides insights into the initial conditions and forcing parameters giving rise to sustained wave propagation.

B. *Spatial and Temporal Fluctuations.*

B1. We have studied propagation in a medium whose dichotomic time-independent excitability varies randomly in space. In 1D, the relative variation of the velocity with respect to the velocity v_0 in the corresponding effective homogeneous medium decreases linearly with Δv, as the total time spent in crossing the whole medium becomes larger. In 2D, the propagation-rate $v - v_0$ increases proportionally to the $\frac{4}{3}$ power of the disorder amplitude relative to v_0. This time the front gets distorted and the interplay between curvature (influenced by the length of the inhomogeneity) and the fast and slow motion of the wave parts determine the velocity of the whole front.

B2. When the dichotomic time-independent random distribution consists in a lattice of excitable and non excitable clusters wave propagation percolates when the proportion p of black sites (representing excitable sites) is above the percolation threshold for that lattice. The effective wave front velocity (proportional to the inverse of the transit time) is observed to jump from zero to finite values at a threshold $p = p_c$ (very close to the percolation thresholds expected for a square lattice) when, as predicted by the classical percolation theory, a cluster of sites with the same excitability spans along the medium. These thresholds depend on the number of effective neighbors which have been controlled by adjusting the overall light intensity reaching the reaction.

B3. The introduction of spatiotemporal fluctuations on a wave train

propagating in an unexcitable channel was found to extent the propagation distance of the periodic structure simulated with the Oregonator model. Stochastic resonance in the sense of the number of fronts reaching a control position occurs not only for an optimal intensity of the noise but also for a correlation time that matches the characteristic time of the periodic structure. With respect to the spatial correlation of the noise, the percentage of wave fronts reaching the control position increases as the correlation length increases and it reaches a maximum for higher values of the correlation time. This is in agreement with other studies in noisy overdamped bistable oscillators where the interplay among noise, nonlinearity and forcing gives rise to an enhancement of propagation.

B4. The same spatiotemporal structured noise was investigated on the motion of a spiral wave in the BZ reaction. While in the absence of randomness, the spiral tip rotates quasi-rigidly around its core, with no net translational mobility, Brownian diffusion of the spiral is observed when the noise is switched on. This motion was characterized by a non-monotonous dependence on the parameters of the noise. For pure temporal fluctuations a resonant-like effect on the diffusion coefficient was found when the correlation time matched the intrinsic rotation frequency of the spiral. When structured noise is added to the system, the diffusion coefficient is even more enhanced, this time for correlation times larger. These observations were confirmed numerically using the two-variable Oregonator model and the analysis was completed with a simple theoretical model based on a kinematic approach which captures the basic features observed in experiments.

B5. We have provided experimental and numerical evidence, and also an analytical explanation, of the beneficial influence of white spatiotemporal fluctuations, by showing that an excitable chemical system may rectify external fluctuations into regularly organized wave trains. Explicitly, we have shown that the photosensitive BZ reaction, under excitable conditions unable to create autowaves, does maintain a target structure when subjected to a patterned and continuously evolving random illumination.

Outlook

What needs to be done?. After finishing this thesis, it seems that many open questions need an answer, more than at the beginning.

Concerning the role of fluctuations, an experimental and numerical study of the batch system (without diffusion) should be performed. Right now, there is not any deep analysis of the Oregonator model and the BZ reaction under the effect of any kind of fluctuations. It would be rather interesting to know how the 0-dimensional system behaves under the presence of noise to understand later their effects on the complete system with diffusion. It would be of special interest to focus on the regions where the system presents critical behavior, that is, around the excitable/oscillatory transition and also when the system stops to be excitable. Due to the existence of a characteristic time scale, as it is the period between two consecutive excitations, colored noise may be of relevance in inducing some kind of transition. In this situation, a comparison between different noises can be carried out, controlling for example their bounds and the correlation function. At the same time, differences between deterministic and stochastic forcing should be clarified (if any) since they share the same frequency.

On the other extreme, going back to spatially extended systems, the natural continuation of this thesis is to study the effects of fluctuations in three dimensional structures, which are known with the name of *scroll waves* in the literature. Some work on this respect has been already carried out, analyzing how spatiotemporal fluctuations time correlated influence the mean life time of a ring structure. In this way, the role of the noise intensity could also be investigated with the aim of looking for the classical stochastic resonance but in a spatially extended system.

A key point to develop further are the nontrivial configurations arising from the propagation of a wave train in a sinusoidally modulated channel. As it was said, the similarity between the spatial return maps describing such spatial configurations and the circle map, allows one to speculate about the existence of even more complex configurations representing the spatial realizations of the chaotic regimes of these maps. Exploring first the spatial return map, one could guess which region of the forcing parameters could produce chaotic spatial structures if they would be accessible from the computational point of view.

Appendix A

Curvature-Speed Relation in the Singular Limit. Kinematic Theory of Autowaves

A.1 The Curvature-Speed Relation in the Singular Limit

Singular perturbation theory [141, 185, 186] applied to waves of activity in excitable media, allows us to obtain approximate information of autowave processes from equations that are easier to solve than the full system of nonlinear equations (2.18)-(2.19).

The theory develops within the limit where excitable dynamics present multiple time scales and wave fronts occur as sharp transitions between slowly varying regions. Using these arguments, the wave form consists of two typical regions: the slowly varying region where diffusion has little effect, and the one where the activator variable (Chapter 1) presents spatial discontinuities making diffusion important. So, propagation of chemical waves can be considered mediated by diffusion of the activator and the effect of the slow variable can be neglected, resulting in the following model problem:

$$\frac{\partial u}{\partial t} = f(u) + D\nabla^2 u \tag{A.1}$$
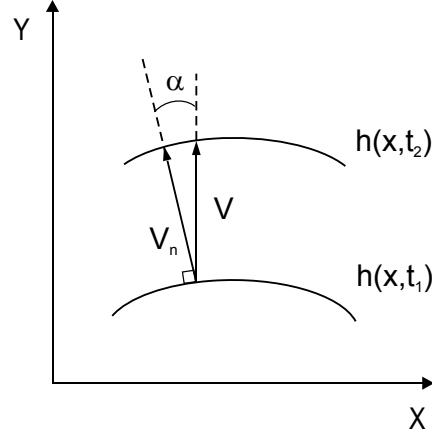
Figure A.1: Normal v_n and planar v velocities in the propagation of a wave contour.

The wave front is confined to a small region of space and moves because the interplay of reaction and diffusion of the propagator species u in the front. We are going to consider this front as a contour line of constant u concentration and seek for translational invariant solutions (of fixed speed and planar form) moving in the reference frame defined by $\xi = y - vt$, such that $u(x, y, t) = u(x, \xi) = u(x, y - vt)$. Therefore, $u(\xi)$ satisfies,

$$-v\frac{du}{d\xi} = f(u) + D\nabla^2 u \tag{A.2}$$

So, the interface $h(x, t) = vt$ moves along the Y-axis with constant velocity v which is determined by the kinetic term $f(u)$. Considering now a circular interface, such that the concentration $u(r)$ is now only a function of the distance from the center of curvature. The interface can be described by $u(r, t) = u_0(r - R(t))$ whenever the radius R is large as compared with the interface thickness. Using the Laplacian in polar coordinates, we find from Eq. (A.1)

$$\frac{\partial u_0}{\partial r} \, \frac{\partial R}{\partial t} = f(u_0) + D \, \frac{1}{r} \, \frac{\partial u_0}{\partial r} + D \, \frac{\partial^2 u_0}{\partial r^2} \tag{A.3}$$

which rearranging terms it adopts the final form,

$$-(\frac{\partial R}{\partial t} + \frac{D}{r}) \, \frac{\partial u_0}{\partial r} = f(u_0) + D \, \frac{\partial^2 u_0}{\partial r^2} \tag{A.4}$$

If we consider an infinitesimal element of the wave contour at position $r = R(t)$, we can assume it to have constant curvature and compare Eq. (A.2) and Eq. (A.4), which yields,

$$\frac{\partial R}{\partial t} = v - \frac{D}{r} \tag{A.5}$$

Equation (A.5) describes the effect of a local curvature on the interface velocity. For an arbitrary interface shape, $\frac{\partial R}{\partial t}$ is nothing but the local normal velocity v_n, and Eq. (A.5) the eikonal equation which gives the normal velocity of a curved wave front. This equation has been applied in other different contexts than the chemical one, like flame front propagation and crystal growth. This is a naive derivation of the eikonal equation and more systematic and rigorous derivation can be found in [141].

Denoting the interface position as $y = h(x, t)$ as shown in Fig. A.1, the following geometrical relations hold:

$$v_n = v \cos \alpha \tag{A.6}$$

$$v = \frac{\partial h}{\partial t} \tag{A.7}$$

$$\cos \alpha = \frac{1}{(1 + h_x^2)^{1/2}} \tag{A.8}$$

$$\sin \alpha = \frac{h_x}{(1 + h_x^2)^{1/2}} \tag{A.9}$$

$$k = \frac{h_{xx}}{(1 + h_x^2)^{3/2}} \tag{A.10}$$

Using these equalities we can rewrite the eikonal equation as a function of the front position as,

$$h_t = v \sqrt{1 + h_x^2} + D \frac{h_{xx}}{1 + h_x^2} \tag{A.11}$$

This effective local equation captures the features of the original field model (as the Oregonator model) with the advantage of a significantly simplification and of a much simpler analytic treatment.

A.2 Kinematic Theory of Autowaves

Kinematics of wave fronts in two-dimensional excitable media has been described by identifying such waves as oriented curves moving in the
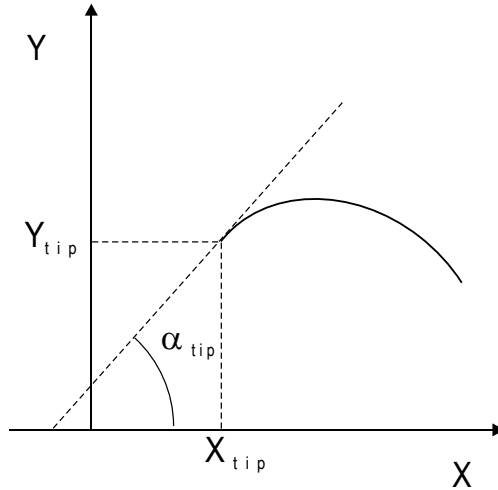
Figure A.2: Schematic representation of the coordinates and angle of the tip to indicate position and orientation of the curve segment.

plane [20]. Within this framework the kinematical description is based on a *natural equation* $k = k(l, t)$ of the curve which gives the temporal dependence of the front curvature k on the length of the curve arc measured from a reference point, usually the end point. The motion of this curve depends on its normal and tangential propagation velocities linearly on the form:

$$V = V_0 - D\,k \qquad (A.12)$$

$$G = \gamma\,(k_c - k) \qquad (A.13)$$

being V the normal velocity of any small segment of the front and G the tangent velocity at its tip (which can be negative if the wave front contracts or positive if sprouts) and V_0, D, γ, and k_c kinematic parameters.

The increment $d\ell$ of the arc length in time dt is given by

$$d\ell = \left(\int_0^l kV ds\right) dt + G dt \qquad (A.14)$$

where the first term describes the elongation of the curve in its normal expansion and the second accounts for the changes in length due to tangential motion of the end point of the curve (contraction or expansion).

If $G > 0$, any initial perturbation of a flat broken front will evolve to a steadily rotating spiral wave. Invoking the so-called quasistatic

approximation, the dynamics of a spiral wave can be reduced to the motion of its tip [20]. If $X(t)$ and $Y(t)$ are the coordinates of the tip of a wave at a time t, and $\alpha(t)$ is the angle between the tangent to the front at the end point and the X-axis as plotted in Fig. A.2, the evolution equations for those coordinates are:

$$\frac{dX}{dt} = -V \sin \alpha - G \cos \alpha \tag{A.15}$$

$$\frac{dY}{dt} = V \cos \alpha - G \sin \alpha \tag{A.16}$$

$$\frac{d\alpha}{dt} = \omega + Gk \tag{A.17}$$

$$\frac{dk}{dt} = -\frac{1}{\tau_G}(k - k_c) \tag{A.18}$$

where V and G are given by the Eqs. (A.12)-(A.13) evaluated at the tip. The third equation defines the evolution of the angle α in terms of rotation and the changes due to the tangent sprouting ($G > 0$). The fourth equation accounts for the relaxation dynamics of the tip curvature to its critical value k_c. In the limit of small curvatures $Dk \ll V_0$, V can be replaced by V_0, the propagation velocity of uncurved waves. The regime of spiral waves rigidly rotating can be obtained by placing $G = 0$, that is, the front neither grows nor contracts at its tip, and $\alpha = \omega_0 t$ which means that the tip moves around a circle at a constant rotation frequency ω_0. The set of kinematic equations for this kind of motion reduces to,

$$\frac{dX}{dt} = -V_0 \sin \omega_0 t$$

$$\frac{dY}{dt} = V_0 \cos \omega_0 t \tag{A.19}$$

So, once the solutions for Eqs. (A.19) and for the *natural equation* $k = k(l, t)$ are known[1], the Cartesian coordinates of the curve points can be found as,

---

[1]For the case of steady circulation, the *natural equation* is of the form $k = (2R\ell)^{-1/2}$ for large ℓ, which approximates an archimedian spiral with a constant step.

$$X(\ell, t) = X_{tip}(t) + \int_0^l \cos(\omega_0 t + \alpha) ds \qquad (A.20)$$

$$Y(\ell, t) = Y_{tip}(t) + \int_0^l \sin(\omega_0 t + \alpha) ds \qquad (A.21)$$

where α is obtained from $k = \frac{d\alpha}{d\ell}$.

Appendix B

Recipes for the Chemistry of the BZ Reaction

The goal of this Appendix is to describe all the stuff necessary to prepare the ruthenium-catalyzed BZ reaction in a Lab where the chemicals involved in can be found. The purpose of doing that is because it is a difficult task since someone buys the chemical products until everything is ready to be used. Unfortunately, all the process is not detailed anywhere. In what follows, it will be described how to prepare the solutions from their commercial distribution, and finally how to perform the BZ reaction in a silica gel system.

Besides, at the end of this Appendix, it is included a brief description of the device used to measure the light intensity in the experiments.

The steps to follow are:

1. Preparation of the Catalyst Solution: $Ru(bpy)_3^{+2}$.

2. Determination of the Concentration of the Photosensitive Catalyst Solution using Spectrophotometrical Techniques.

3. Preparation of the Sodium Silicate Solution (*Waterglass*).

4. Preparation of the Silica Gel.

5. Recipe and BZ Reaction.

B.1 Preparation of the Catalyst Solution: $\mathrm{Ru(bpy)}_3^{+2}$.

The $[\mathrm{Ru(bpy)}_3]\mathrm{SO}_4$ solution is prepared from a commercial salt of ruthenium complex tris(2,2-bipyridine)-ruthenium(II) chloride ($\mathrm{C}_{30}\mathrm{H}_{24}\mathrm{N}_6\mathrm{RuCl}_2$, $P_m = 640.5$) presented in small red crystals. Nowadays, the ALDRICH firm sells a *hexahydrated* salt variant of slightly higher molecular weight ($P_m = 748.63$). To free the commercial salt from the chloride ions the next recipe should be followed:

> Recipe:
> 3 g of $\mathrm{Ru(bpy)}_3\mathrm{Cl}_2\cdot 6\mathrm{H}_2\mathrm{O}$ dissolved in 40 ml of distilled water
> and made up to 100 ml with 5 M $\mathrm{H}_2\mathrm{SO}_4$.

The red solution obtained in this way has to settle two days (preferably in the dark and at room temperature) in order the $[\mathrm{Ru(bpy)}_3]\mathrm{SO}_4$ precipitates. After these two days, the precipitate is filtered using a vacuum pump and a filter paper to gather it. Distilled water should not be used to recover the rests of precipitate from the bottom of the recipient because it will dissolve them again. Instead the solution just filtered can help to remove them from the bottom of the flask. The filter paper with the precipitate is left to get dried (enough at room temperature and protected from the light). After that, the filter and the precipitate are put together in 100 ml of 25 mM $\mathrm{H}_2\mathrm{SO}_4$ (this method allows more concentrated solutions). The salt is dissolved and the filter is removed from the solution. This should be filtered again if small pieces of paper are still inside.

B.2 Determination of the Concentration of the Photosensitive Catalyst Solution using Spectrophotometrical Techniques.

The solution obtained in the previous step has a concentration C_0 that is unknown. To determine such concentration, the use of a spectrophotometer is required. The one employed in our measurements is in the Faculty of Chemistry and is of the double beam type and scans within the visible light frequencies range (our solution has an absorption peak centered around 460 nm).

The method used to determine the concentration C_0 is the *Lambert-Beer law*:

$$C_i = \frac{1}{\varepsilon d} \log \frac{I_0}{I} \tag{B.1}$$
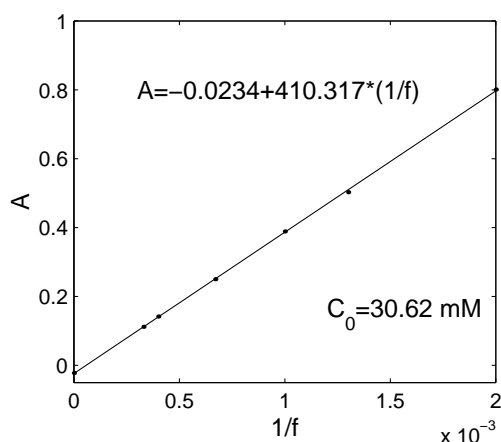
Figure B.1: Example of the fitting of the absorbances of samples of different concentrations. These samples are dilutions of the same primary solution whose concentration C_0 has to be determined from the slope of the linear fitting of the points.

being

C_i= sample concentration molarity

ε=13400(M^{-1} cm^{-1}) extinction constant

d= 1 cm (width of the absorbed light path)

Preparing n different samples by diluting f_i times the primary solution of unknown C_0 concentration, and measuring their absorbances, we obtain n points corresponding to the concentrations C_i and absorbances A_i, where $C_i = C_0/f_i$ and A_i is obtained directly from the spectrophotometer representing the value $\log \frac{I_0}{I}$. Fitting the points $(1/f_i,\ A_i)$ to a straight line, the concentration C_0 can be obtained from the slope $m = C_0 \varepsilon d$ of that fit. An example of one of them is shown in Fig. B.1.

B.3 Preparation of the Sodium Silicate Solution (*waterglass*).

The solution used to make the silica gels is prepared using sodium silicate (powder from Riedel-de-Haën) containing 60% SiO$_2$ and 18% Na$_2$O.

Recipe:

15 g of sodium silicate dissolved in distilled water up to 100 ml

The solution is boiled and constantly stirred to favor the complete mixing, until the solution becomes clear (approximately one day). After cooling down to room temperature, the solution needs to be filtered and it should be added the lost water (both by evaporation and filtering).

B.4 Preparation of the Silica Gel.

The preparation of the silica gel requires everything is ready before mixing the reagents because the gelification time is short. We need a piece of glass placed over two lead bars of a specific diameter (which will determine the thickness of the gel, from 0.3 mm to 1 mm), that in turn are over a methacrylate surface.

The recipe to make the gel is as follows [81]:

Recipe for 2 ml of gel:
1.333 ml 15% NaSiO$_3$
0.176 ml H$_2$O
0.131 ml 30.62 mM Ru(bpy)$_3^{+2}$
0.360 ml 1 M H$_2$SO$_4$

Final concentrations in the gel are 0.18 M H$_2$SO$_4$ and 2 mM Ru(bpy)$_3^{+2}$. The use of a magnetic stirrer is essential to keep the mixture continuously shaken and to prevent it to become gel. In a small glass with a magnetic bar inside the reagents are added in the same order as they were listed above. Care should be taken when adding the sulfuric acid, the last one, because it causes the liquid solution transforms into gel. Before reaching that state and while it is still liquid, the solution is absorbed with the help of a pipette and injected between the glass and the methacrylate. After a while, the solution is gelly and the lead bars can be removed carefully. The gel is stuck to the glass but not to the methacrylate so it can be slid over it.

The ruthenium is now immobilized in a silica gel matrix and the rest of the reagents should be added in order the reaction takes place without hydrodynamic perturbations.

B.5 Recipe and BZ Reaction.

Grade reagents are commercially available both from the SIGMA and ALDRICH firms to prepare with distilled water the stock solutions involved in the BZ reaction, namely: sulfuric acid, sodium bromate, malonic acid and potassium chloride. Once the silica gel system is ready, a mixture with the rest of the reactants is prepared in the following way:

Recipe for the aqueous solution mixture:
0.60 ml 6 M H$_2$SO$_4$
2.85 ml 1 M NaBrO$_3$

  0.65 ml 4 M malonic acid
  2.05 ml H$_2$0
  1.35 ml 1 M KBr

When adding the bromide, the solution turns red colored, and after a while it becomes clear again. The total volume is 7.5 ml and the final concentrations after completion are: 0.48 M H$_2$SO$_4$, 0.38 M NaBrO$_3$, 0.34 M malonic acid, and 0.18 M KBr. The solution is pored onto the gel+glass system which was placed inside a Petri dish. The volume of solution should be enough to cover the gel and to avoid contact with the oxygen. The experiment is ready to run.

B.6 Photometer.

Light intensity reaching the BZ reaction was measured using a silicon photodiode (**RS** stock no. 305-462) with a flat glass window of 3.9 mm diameter. The photodiode was connected to a battery of 15 V, to a I-V converter and to a voltimeter as shown in Fig. B.2. The response of the photodiode is proportional to the light intensity given by the relation:

$$\phi = \frac{V}{R_e R} \tag{B.2}$$

where V is the measured output voltage, R_e is the responsivity and equal to 0.7 μA/mW/cm^2, and R is an internal resistor chosen to give required output.
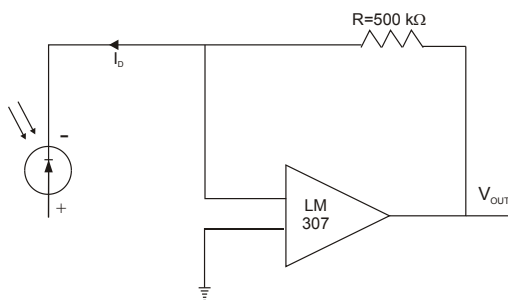
Figure B.2: Photometer circuit consisting in a photodiode, an operational amplifier, and a resistor. The output voltage is equal to $V = RI_D$, being I_D the current through the photodiode, which in turns depend on the incident light.

Appendix C

Analytical Approach of the Return Map for the Front Positions of a Wave Train in a Sausage-Like Channel

In this Appendix an analytical approach to the return map for the positions of a wave train propagating in a sausage-like channel is given. An expansion to order $\mathcal{O}(c_1/c_0)$ of the Eq. (3.17) will lead us to a return map of the sine type, which suggests that our system may support more than quasiperiodic configurations.

From,

$$\frac{2}{k\sqrt{c_0^2 - c_1^2}} \left[\arctan f(x_n)\right]_{x_n(0)}^{x_{n+1}(0)} = T \tag{C.1}$$

where

$$f(x_n) = \sqrt{\frac{c_0 + c_1}{c_0 - c_1}} \tan\left(\frac{kx_n}{2}\right) \tag{C.2}$$

the following relationship between x_{n+1} and x_n holds,

$$A \arctan\left[B \tan\left(\frac{kx_{n+1}}{2}\right)\right] = T + A \arctan\left[B \tan\left(\frac{kx_n}{2}\right)\right] \tag{C.3}$$

with

$$A \;=\; \frac{2}{k\sqrt{c_0^2 - c_1^2}}$$

$$B \;=\; \sqrt{\frac{c_0 + c_1}{c_0 - c_1}}$$

Since $c_0 \gg c_1$ we can expand B up to order $\mathcal{O}(c_1/c_0)$ to obtain:

$$A \arctan\left[B \tan\left(\frac{kx_n}{2}\right)\right] = A \arctan\left[(1 + \frac{c_1}{c_0}) \tan\left(\frac{kx_n}{2}\right)\right] \qquad \text{(C.4)}$$

Now we need to express the argument of the arctan on the right-hand side of Eq. (C.4) as $\tan\beta$, so $\arctan(\tan\beta) = \beta$. In order to do that we call

$$\tan\beta = \tan\left(\frac{kx_n}{2}\right) + \frac{c_1}{c_0} \tan\left(\frac{kx_n}{2}\right) = \tan\beta_0 + b \qquad \text{(C.5)}$$

where $\beta_0 = \frac{kx_n}{2}$ and $b = \frac{c_1}{c_0}\tan\beta_0 \ll 1$.

We suppose that $\beta = \beta_0 + a$ with $a \ll 1$. Developing $\tan\beta = \tan\beta_0 + a\sec^2\beta_0 + ...$, and comparing this expansion with the previous one, it results that $a\sec^2\beta_0 = b$. So, we easily get:

$$\beta = \beta_0 + a = \frac{kx_n}{2} + \frac{c_1}{2c_0}\sin(kx_n) \qquad \text{(C.6)}$$

where $2\sin\beta_0 \cos\beta_0 = \sin(2\beta_0)$ has been used. Evaluating Eq. (C.4) by using Eq. (C.6),

$$A\left(\frac{kx_{n+1}}{2} + \frac{c_1}{2c_0}\sin(kx_{n+1})\right) = T + A\left(\frac{kx_n}{2} + \frac{c_1}{2c_0}\sin(kx_n)\right) \qquad \text{(C.7)}$$

Substituting constants, rearranging terms and also approximating A up to first order in c_1/c_0, we end up with:

$$x_{n+1} = x_n + c_0 T - \frac{c_1}{kc_0}\left[\sin(kx_{n+1}) - \sin(kx_n)\right] \qquad \text{(C.8)}$$

If $c_1 = 0$, that is, a channel of uniform width, it results $x_{n+1} = x_n + c_0 T$ which is the corresponding linear map for such situation. In order to solve the difference of sines in Eq. (C.8), we make the approximation $x_{n+1} = x_n + c_0 T$ so we have,

$$\sin(kx_{n+1}) - \sin(kx_n) = \sin(kc_0 T)\cos(kx_n) - [1 - \cos(kc_0 T)]sin(kx_n) \qquad \text{(C.9)}$$

Making some trigonometrical manipulations,

$$
\begin{aligned}
\sin(kx_{n+1}) - \sin(kx_n) &= 2\sin\varphi\cos\varphi\cos(kx_n) - 2\sin^2\varphi\sin(kx_n) \\
&= 2\sin\varphi\left[\cos\varphi\cos(kx_n) - \sin\varphi\sin(kx_n)\right] \\
&= 2\sin\varphi\cos(kx_n + \varphi) \tag{C.10}
\end{aligned}
$$

being $\varphi = \frac{kc_0 T}{2}$.

So the final expression for the return map of the front positions takes the form,

$$
x_{n+1} = x_n + c_0 T - \rho\cos(kx_n + \varphi) \tag{C.11}
$$

where $\rho = 2\frac{c_1}{kc_0}\sin\varphi$ is the constant of coupling which accounts for the amplitude of the nonlinear perturbation, and φ a phase lag. If $kc_0 T \ll 1$, that is, the wavelength of the train in a straight channel is smaller than the modulation wavelength, the Eq. (C.11) becomes a pure circle map,

$$
x_{n+1} = x_n + c_0 T - c_1 T\cos kx_n \tag{C.12}
$$

If not, the phase lag would explain the observed phase modulation in the return maps for the front position for the case of strong forcing.

Bibliography

[1] J. García Ojalvo and J. M. Sancho, *Noise in Spatially Extended Systems*, Springer-Verlag, New York, 1999.

[2] M. San Miguel and R. Toral, *Stochastic Effects in Physical Systems*, Instabilities and Nonequilibrium Structures VI (E. Tirapegui, J. Martínez, and R. Tiemann, eds.), Kluwer Academic Publishers, 2000, pp. 35–130.

[3] A. Goldbeter, *Biochemical Oscillations and Cellular Rhythms*, Cambridge Univ. Press, Cambridge, 1996.

[4] P. Jung, A. Cornell-Bell, K. S. Madden, and F. Moss, *Noise-Induced Spiral Waves in Astrocyte Syncytia Show Evidence of Self-Organized Criticality*, J. Neurophys. **79**, 1098–1101, 1998.

[5] P. Jung, A. Cornell-Bell, F. Moss, S. Kádár, J. Wang, and K. Showalter, *Noise Sustained Waves in Subexcitable Media: from Chemical Waves to Brain Waves*, Chaos **8** (3), 567–575, 1998.

[6] E. Mihaliuk, *Identification and Control of Dynamical Systems*, Ph.D. thesis, West Virginia University, U.S.A., 1999.

[7] V. Pérez-Muñuzuri and M. N. Lorenzo, *Experimental Improvement of Chaotic Synchronization due to Multiplicative Time-Correlated Gaussian Noise*, Int. J. of Bif. and Chaos **9** (12), 2321–2327, 1999.

[8] M. Löcher, D. Cigna, and E. R. Hunt, *Noise Sustained Propagation of a Signal in Coupled Bistable Electronic Elements*, Phys. Rev. Lett. **80** (23), 5212–5215, 1998.

[9] R. Buizza, M. Miller, and T. N. Palmer, *Stochastic Simulation of Model Uncertanties in the ECMWF Ensemble Prediction System*, Q. J. R. Meteorol. Soc. **125** (560), 2887–2908, 1999.

[10] J. Wang, S. Kádár, P. Jung, and K. Showalter, *Noise Driven Avalanche Behaviour in Subexctiable Media*, Phys. Rev. Lett. **82** (4), 855–858, 1999.

[11] S. Kádár, J. Wang, and K. Showalter, *Noise-Supported Travelling Waves in Sub-Excitable Media*, Nature **391**, 770–772, 1998.

[12] M. S. Spach and J. F. Heidlage, *The Stochastic Nature of Cardiac Propagation at a Microscopic Level. An Electrical Description of Myocardial Architecture and its Application to Conduction*, Circ. Res **76**, 366–380, 1995.

[13] A. N. Zaikin and A. M. Zhabotinsky, *Concentration Wave Propagation in Two-Dimensional Liquid-Phase Self-Oscillating System*, Nature **255**, 535–536, 1970.

[14] A. R. Kerstein and Wm. Ashurst, *Propagation Rate of Growing Interfaces in Stirred Fluids*, Phys. Rev. Lett. **68** (7), 934–937, 1992.

[15] M. Kardar, G. Parisi, and Y.-C. Zhang, *Dynamic Scaling of Growing Interfaces*, Phys. Rev. Lett. **56** (9), 889–892, 1986.

[16] V. Petrov, Q. Ouyang, and H. L. Swinney, *Resonant Pattern Formation in a Chemical System*, Nature **388**, 655–657, 1997.

[17] A. L. Lin, M. Bertram, K. Martinez, and H. L. Swinney, *Resonant Phase Patterns in a Reaction-Diffusion System*, Phys. Rev. Lett. **84** (18), 4240–4243, 2000.

[18] G. Nicolis and I. Prigogine, *Self-Organization in Nonequilibrium Systems, from Dissipative Structures to Order through Fluctuations*, Wiley Interscience, New York, 1977.

[19] H. Haken, *Advanced Synergetics*, Springer-Verlag, Berlin, 1987.

[20] A. S. Mikhailov, *Foundations of Synergetics. I: Distributed Active Systems*, Springer-Verlag, Berlin, 1991.

[21] M. C. Cross and P. C. Hohenberg, *Pattern Formation Outside of Equilibrium*, Rev. Mod. Phys. **65** (3), 851–1112, 1993.

[22] C. Bowman and A. C. Newell, *Natural Patterns and Wavelets*, Rev. Mod. Phys. **70** (1), 289–301, 1998.

[23] C. B. Muratov and V. V. Osipov, *Scenarios of Domain Pattern Formation in a Reaction-Diffusion System*, Phys. Rev. E **54** (5), 4860–4879, 1996.

[24] T. Nozakura and S. Ikeuchi, *Formation of Dissipative Structures in Galaxies*, Astr. J. **279**, 40–52, 1984.

[25] F. J. Niedernostheide (ed.), *Nonlinear Dynamics and Pattern Formation in Semiconductors and Devices*, Springer, Berlin, 1994.

[26] Yu. A. Astrov, I. Müller, E. Ammelt, and H.-G. Purwins, *Zigzag Destabilized Spirals and Targets*, Phys. Rev. Lett. **80** (24), 5341–5344, 1998.

[27] P. Coullet, T. Frisch, J. M. Gilli, and S. Rica, *Excitability in Liquid Crystal*, Chaos **4** (3), 485–489, 1994.

[28] J. V. Moloney and A. C. Newell, *Nonlinear Optics*, Physica D **44**, 1–37, 1990.

[29] J. V. Moloney and A. C. Newell, *Nonlinear Optics*, Addison Wesley, Reading, MA, 1992.

[30] A. M. Turing, *The Chemical Basis of Morphogenesis*, Phil. Trans. R. Soc. London B **237**, 37–72, 1952.

[31] J. D. Murray, *Mathematical Biology*, Springer-Verlag, Berlin, 1989.

[32] P. Manneville, *Dissipative Structures and Weak Turbulence*, Academic, San Diego, CA, 1990.

[33] R. Kapral and K. Showalter (eds.), *Chemical Waves and Patterns*, Kluwer, Dordrecht, 1995.

[34] R. J. Field and M. Burger (eds.), *Oscillations and Travelling Waves in Chemical Systems*, Wiley, New York, 1985.

[35] K. J. Lee, E. C. Cox, and R. E. Goldstein, *Competing Patterns of Signaling Activity in Dictyostelium Discoideum*, Phys. Rev. Lett. **76** (7), 1174–1177, 1996.

[36] R. A. Gray and J. Jalife, *Spiral Waves and the Heart*, Int. J. of Bif. and Chaos **6** (3), 415–435, 1996.

[37] G. R. Mines, *On Dynamic Equilibrium in the Heart*, J. Physiol. **46**, 349–382, 1913.

[38] W. E. Garey, *The Nature of Fibrillary Contraction of the Heart -Its Relation to Tissue Mass and Form*, Am. J. Physiol. **33**, 397–414, 1914.

[39] A. T. Winfree, *Spiral Waves of Chemical Activity*, Science **175**, 634–635, 1972.

[40] A. V. Holden, M. J. Poole, and J. V. Tucker, *An Algorithmic Model of the Mammalian Heart: Propagation, Vulnerability, Re-Entry and Fibrillation*, Int. J. of Bif. and Chaos **6** (9), 1623–1635, 1996.

[41] V. I. Krinsky, *Autowaves: Results, Problems, Outlooks*, Self-Organization Autowaves and Structures Far from Equilibrium (V. I. Krinsky, ed.), 1984, p. 9.

[42] V. A. Vasiliev, Yu. M. Romanovskii, C. S. Chernavskii, and V. G. Yakhno, *Autowave Processes in Kinetic Systems*, Reidel, Dordrecht, 1986.

[43] V. S. Zykov, *Simulation of Wave Processes in Excitable Media*, A. T. Winfree ed., Manchester Universtiy Press, Manchester, 1987.

[44] V. S. Zykov, *Analytical Evaluation of the Dependence of the Speed of Excitation Wave in a Two-Dimensional Excitable Medium on the Curvature of its Front*, Biophysics **25**, 906–911, 1980.

[45] J. P. Keener and J. J. Tyson, *Spiral Waves in the Belousov-Zhabotinksy Reaction*, Physica D **21**, 307–324, 1986.

[46] P. Foerster, S. C. Müller, and B. Hess, *Curvature and Propagation Velocity of Chemical Waves*, Science **241**, 685–687, 1988.

[47] P. Foerster, S. C. Müller, and B. Hess, *Temperature Dependence of Curvature-Velocity Relationship in an Excitable Belousov-Zhabotinsky reaction*, J. of Phys. Chem. **94** (26), 8859–8861, 1990.

[48] V. Pérez-Muñuzuri, C. Souto, M. Gómez-Gesteria, A. P. Muñuzuri, V. A. Davydov, and V. Pérez-Villar, *Use of V-shaped Stable Patterns to Study High Negative Curvature-Velocity Dependence of an Excitable Medium*, Physica D **94**, 148–156, 1996.

[49] J. M. Davidenko, A. V. Pertsov, R. Salomonsz, W. Baxter, and J. Jalife, *Stationary and Drifting Spiral Waves of Excitation in Isolated Cardiac- Muscle*, Nature **355**, 349–351, 1992.

[50] P. K. Brazhnik and J. J. Tyson, *Velocity-Curvature Dependence for Chemical Waves in the Belousov-Zhabotinsky Reaction: Theoretical Explanation of Experimental Observations*, Phys. Rev. E **59** (4), 3920–3925, 1999.

[51] A. Pérez Muñuzuri, *Controlling Spatio-Temporal Structures by means of Externally Imposed Forcings in Active Media*, Ph.D. thesis, University of Santiago de Compostela, Spain, 1996.

[52] R. Gómez Gesteira, *Dinámica de Ondas Espirales en Sistemas no Lineales: Formación de Vórtices en Medios Biofísicos*, Ph.D. thesis, Universtiy of Santiago de Compostela, Spain, 1995.

[53] V. Pérez-Muñuzuri, R. Aliev, B. N. Vasiev, and Krinsky V. I., *Electric Current Control of Spiral Wave Dynamics*, Physica D **56**, 229–234, 1992.

[54] A. V. Panfilov and B. N. Vasiev, *Vortex Initiation in a Heterogeneous Excitable Medium*, Physica D **49**, 107–113, 1991.

[55] M. Gómez-Gesteira, J. L. del Castillo, M. E. Vázquez-Iglesias, V. Pérez Muñuzuri, and V. Pérez-Villar, *Influence of the Critical Curvature on Spiral Initiation in an Excitable Medium*, Phys. Rev. E **50** (6), 4646–4649, 1994.

[56] J. M. Starobin and C. F. Starmer, *Boundary-Layer Analysis of Waves Propagating in an Excitable Medium: Medium Conditions for Wave-Front-Obstacle Separation*, Phys. Rev. E **54** (1), 430–437, 1996.

[57] K. Agladze, J. P. Keener, S. C. Müller, and A. Panfilov, *Rotating Spiral Waves Created by Geometry*, Science **264**, 1746–1748, 1994.

[58] C. F. Starmer, V. N. Biktashev, C. N. Romashko, M. N. Stepanov, O. N. Makarova, and V. I. Krinsky, *Vulnerability in an Excitable Medium: Analytical and Numerical Studies of Initiating Unidirectional Propagation*, Biophys. J. **65**, 1775–1787, 1993.

[59] M. Gómez-Gesteira, G. Fernández-García, A. P. Muñuzuri, V. Pérez-Muñuzuri, V. I. Krinsky, C. F. Starmer, and V. Pérez-Villar,

Vulnerability in an Excitable Belousov-Zhabotinsky Medium: From 1D to 2D, Physica D **76**, 359–368, 1994.

[60] P. C. Fife, *Understanding the Patterns in the BZ Reagent*, J. Stat. Phys. **39** (5–6), 687–703, 1985.

[61] Showalter's Group Web Page, http://control.chem.wvu.edu/.

[62] Center for Nonlinear Dynamics, http://chaos.ph.utexas.edu/.

[63] Univ. of Magdeburg Department of Biophysics, http://www.uni-magdeburg.de/abp/.

[64] Grupo de Física non lineal Web Page, http://chaos.usc.es/.

[65] A. M. Zhabotinsky, *A History of Chemical Oscillations and Waves*, Chaos **1** (4), 379–386, 1991.

[66] R. J. Field, E. Körös, and R. M. Noyes, *Oscillations in Chemical Systems. II. Thorough Analysis of Temporal Oscillations in the Bromate-Cerium-Malonic Acid System*, J. Am. Chem. Soc. **94** (25), 8649–8664, 1972.

[67] V. Petrov, V. Gáspár, J. Masere, and K. Showalter, *Controlling Chaos in the Belousov-Zhabotinsky Reaction*, Nature **361**, 240–243, 1993.

[68] R. H. Simoyi, A. Wolf, and H. L. Swinney, *One-Dimensional Dynamics in a Multicomponent Chemical Reaction*, Phys. Rev. Lett. **49** (4), 245–248, 1982.

[69] V. A. Vavilin, A. M. Zhabotinsky, and A. N. Zaikin, *Effect of Ultraviolet Radiation on the Oscillating Oxidation Reaction of Malonic Acid Derivatives*, Russ. J. Phys. Chem. **42**, 1649–, 1968.

[70] H. Busse and B. Hess, *Information Transmission in a Diffusion-Coupled Oscillatory Chemical System*, Nature **244**, 203–205, 1973.

[71] V. Gáspár, Gy. Bazsa, and M.T. Beck, *The Influence of Visible Light on the Belousov-Zhabotinskii Oscillating Reactions Applying Different Catalysts*, Z. Phys. Chem. **264**, 43–48, 1983.

[72] S. Kádár, T. Amemiya, and K. Showalter, *Reaction Mechanism for Light Sensitivity of the $Ru(bpy)_3^{+2}$ Catalyzed Belousov-Zhabotinsky Reaction*, J. Phys. Chem. A **101** (44), 8200–8206, 1997.

[73] M. K. Ram Reddy, Zs. Nagy Ungvarai, and S. C. Müller, *Effect of Visible light on Wave Propagation in the Ruthenium-Catalyzed Belousov-Zhabotinsky Reaction*, J. Phys. Chem. **98** (47), 12255–12259, 1994.

[74] L. Kuhnert and H. J. Krug, *Kinetics of Chemical Waves in the Acidic Bromate-Malonic Acid-Ru(bpy)$_3^{+2}$ System. Comparison with the Ferroin System*, J. Phys. Chem. **91** (3), 730–733, 1987.

[75] L. Kuhnert, *A New Optical Photochemical Memory Device in a Light-Sensitive Active Medium*, Nature **319**, 393–394, 1986.

[76] L. Kuhnert, K. I. Agladze, and V. I. Krinsky, *Image Processing Using Light-Sensitive Chemical Waves*, Nature **337**, 244–247, 1989.

[77] O. Steinbock, V. S. Zykov, and S. C. Müller, *Wave Propagation in an Excitable Medium along a Line of a Velocity Jump*, Phys. Rev. E **48** (5), 3295–3298, 1993.

[78] A. P. Muñuzuri, V. A. Davydov, M. Gómez-Gesteira, V. Pérez-Muñuzuri, and V. Pérez-Villar, *Frequency-Modulated Autowaves in Excitable Media*, Phys. Rev. E **54** (6), 1–4, 1996.

[79] O. Steinbock, V. S. Zykov, and S. C. Müller, *Control of Spiral-Wave Dynamics in Active media by Periodic Modulation of Excitability*, Nature **366**, 322–324, 1993.

[80] A. P. Muñuzuri and M. Markus, *Simple Optical Feedback Loop: Excitation Waves and their Mirror Image*, Phys. Rev. E **55** (1), R33–R35, 1997.

[81] T. Yamaguchi, L. Kuhnert, Zs. Nagy Ungvaray, S. C. Müller, and B. Hess, *Gel Systems for the Belousov-Zhabotinsky Reaction*, J. Phys. Chem. **95**, 5831–5837, 1991.

[82] I. Sendiña-Nadal, M. Gómez-Gesteira, V. Pérez-Muñuzuri, V. Pérez-Villar, J. Armero, L. Ramírez-Piscina, J. Casademunt, F. Sagués, and J. M. Sancho, *Wave Competition in Excitable Modulated Media*, Phys. Rev. E **56** (6), 6298–6301, 1997.

[83] C. J. Hemming and R. Kapral, *Resonantly Forced Inhomogeneous Reaction-Diffusion Systems*, Chaos **10** (3), 720–730, 2000.

[84] W. H. Press, S. A. Teukolsky, W. T. Vetterling, and B. P. Flannery, *Numerical Recipes in Fortran 77: The Art of Scientific Computing*, 2nd ed., Cambridge University Press, Cambridge, 1992.

[85] R. F. Fox, I. R. Gatland, R. R. Roy, and G. Vemuri, *Fast, Accurate Algorithm for Numerical Simulation of Exponentially Correlated Noise*, Phys. Rev. A **38** (11), 5938–5940, 1998.

[86] R. J. Field and R. M. Noyes, *Oscillations in Chemical Systems IV. Limit Cycle Behaviour in a Model of a Real Chemical Reaction*, J. Chem. Phys. **60**, 1877–1884, 1974.

[87] H.-J. Krug, L. Pohlmann, and L. Kuhnert, *Analysis of the Modified Complete Oregonator Accounting for Oxygen Sensitivity and Photosensitivity of Belousov-Zhabotinsky Systems*, J. Phys. Chem. **94**, 4862–4866, 1990.

[88] J. J. Tyson and P. C. Fife, *Target Patterns in a Realistic Model of the Belousov-Zhabotinsky Reaction*, J. Chem. Phys. **73**, 2224–2237, 1980.

[89] J. M. Sancho, M. San Miguel, S. L. Katz, and J. D. Gunton, *Analytical and Numerical Studies of Multiplicative Noise*, Phys. Rev. A **26** (3), 1589–1609, 1982.

[90] R. Toral and A. Chakrabarti, *Generation of Gaussian Distributed Random Numbers by using a Numerical Inversion Method*, Computer Physics Communication **7**, 327–334, 1993.

[91] K. I. Agladze, V. A. Davydov, and A.S. Mikhailov, *Observation of a Helical-Wave Resonance in an Excitable Distributed Medium*, JETP Lett. **45** (12), 767–770, 1987.

[92] V. S. Zykov, O. Steinbock, and S. C. Müller, *External Forcing of Spiral Waves*, Chaos **4** (3), 509–518, 1994.

[93] M. Markus, Zs. Nagy-Ungvarai, and B. Hess, *Phototaxis of Spiral Waves*, Science **257**, 225–227, 1992.

[94] A. P. Muñuzuri, C. Innocenti, J.-M. Flesselles, J.-M. Gilli, K. I. Agladze, and V. I. Krinsky, *Elastic Excitable Medium*, Phys. Rev. E **50** (2), R667–R670, 1994.

[95] I. Sendiña-Nadal, S. Alonso, V. Pérez-Muñuzuri, M. Gómez-Gesteira, V. Pérez-Villar, L. Ramírez-Piscina, J. Casademunt, J. M. Sancho, and F. Sagués, *Brownian-Motion of Spiral Waves Driven by Spatio-Temporal Structured Noise*, Phys. Rev. Lett. **84** (12), 2734–2737, 2000.

[96] V. Pérez-Muñuzuri, F. Sagués, and J. M. Sancho, *Lifetime Enhancement of Scroll Rings by Spatiotemporal Fluctuations*, Phys. Rev. E **62** (1), 94–99, 2000.

[97] A. Garfinkel, Y.-H. Kim, O. Voroshilovsky, Z. Qu, J. R. Kil, M.-H. Lee, H. S. Karagueuzian, J. N. Weiss, and P.-S. Chen, *Preventing ventricular fibrillation by flattening cardiac restitution*, Proc. Natl. Acad. Sci. **97** (11), 6061–6066, 2000.

[98] M. Gómez-Gesteira, A. P. Muñuzuri, V. Pérez-Muñuzuri, and V. Pérez-Villar, *Boundary-Imposed Spiral Drift*, Phys. Rev. E **53** (5), 5480–5483, 1996.

[99] J. A. Sepulchre and A. Babloyantz, *Motions of Spiral Waves in Oscillatory Media and in the Presence of Obstacles*, Phys. Rev. E **48** (1), 187–195, 1993.

[100] I. Aranson, D. Kessler, and I. Mitkov, *Boundary-Induced Drift of Spirals in Excitable media*, Phys. Rev. E **50** (4), R2395–R2398, 1994.

[101] A. M. Zhabotinsky, M. D. Eager, and I. R. Epstein, *Refraction and Reflection of Chemical Waves*, Phys. Rev. Lett. **71** (10), 1526–1529, 1993.

[102] A. Tóth, V. Gáspár, and K. Showalter, *Signal Transmission in Chemical Systems: Propagation of Chemical Waves through Capillary Tubes*, J. Phys. Chem. **98**, 522–531, 1994.

[103] V. M. Eguíluz, E. Hernández-García, O. Piro, and S. Balle, *Frozen Spatial Chaos Induced by Boundaries*, Phys. Rev. E **60** (6), 6571–6579, 1999.

[104] E. Meron, *Pattern Formation in Excitable Media*, Phys. Rep. **218** (1), 1–66, 1992.

[105] I. Sendiña-Nadal, V. Pérez-Muñuzuri, V. M. Eguíluz, E. Hernández-García, and O. Piro, *Quasiperiodic Patterns in Boundary-Modulated Excitable Waves*, Phys. Rev. E, Accepted in May 2001.

[106] H. Hemple, L. Shimansky-Geier, and J. García-Ojalvo, *Noise-Sustained Pulsating Patterns and Global Oscillations in Subexcitable Media*, Phys. Rev. Lett. **82** (18), 3713–3716, 1999.

[107] J. F. Lindner, S. Chandramouli, A. R. Bulsara, M. Löcher, and W. L. Ditto, *Noise Enhanced Propagation*, Phys. Rev. Lett. **81** (23), 5048–5051, 1998.

[108] I. Sendiña-Nadal, E. Mihaliuk, J. Wang, V. Pérez-Muñuzuri, and K. Showalter, *Wave Propagation in Subexcitable Media with Periodically Modulated Excitability*, Phys. Rev. Lett. **86**, 1646–1649, 2001.

[109] G. R. Mines, *On Circulating Excitations in Heart Muscles and their Possible Relation to Tachycardia and Fibrillation*, Trans. R. Soc. Can. **4**, 43–53, 1914.

[110] M. A. Allesie, F. I. M. Bonke, and F. G. J. Schopman, *Circus Movement in Rabbit Atrial Muscle as a Mechanism in Tachycardia*, Circ. Res. **33**, 54–62, 1973.

[111] M. S. Spach, W. T. Miller III, D. B. Geselowitz, R. C. Barr, J. M. Kootsey, and E. A. Johnson, *The Discontinuous Nature of Propagation in Normal Canine Cardiac Muscle. Evidence for Recurrent Discontinuities of Intracellular Resistance that affect the Membrane Currents*, Circ. Res. **48**, 39–45, 1981.

[112] A. Karma, *Spiral Breakup in Model Equations of Action Potential Propagation in Cardiac Tissue*, Phys. Rev. Lett. **71** (7), 1103–1106, 1993.

[113] P. Jung and G. Mayer-Kress, *Spatiotemporal Stochastic Resonance in Excitable Media*, Phys. Rev. Lett. **74** (11), 2130–2133, 1995.

[114] P. Jung and G. Mayer-Kress, *Noise Controlled Spiral Growth in Excitable Media*, Chaos **5** (2), 458–462, 1995.

[115] P. De Kepper and W. Horsthemke, *Étude d'une Réaction Chimique Périodique. Influence de la Lumière et Transitions Induites par un Bruit Externe*, C. R. Acad. Sc. Paris **287** (7), 20–23, 1978.

[116] J. Maselko and K. Showalter, *Chemical Waves in Inhomogeneous Excitable Media*, Physica D **49**, 21–32, 1991.

[117] A. S. Mikhailov, L. Schimansky-Geier, and W. Ebeling, *Stochastic Motion of the Propagating Front in Bistable Media*, Phys. Lett. A **96**, 453, 1983.

[118] O. T. Valls and L. M. Lust, *Effect of Noise on Front Propagation*, Phys. Rev. B **44** (9), 4326–4331, 1991.

[119] S. Cornell, M. Droz, and B. Chopard, *Role of the Fluctuations for Inhomogeneous Reaction-Diffusion Phenomena*, Phys. Rev. A **44**, 4826–4832, 1991.

[120] A. Lemarchand, H. Lemarchand, E. Sulpice, and M. Mareschal, *Microscopic Simulation of a Wave Front: Fluctuations Effects on Propagation Velocity and Width*, Physica A **188**, 277–283, 1992.

[121] V. Pérez-Muñuzuri, M. Gómez-Gesteira, V. Pérez-Villar, and L. O. Chua, *Traveling Wave Propagation in a One-Dimensional Fluctuating Medium*, Int. J. of Bif. and Chaos **3** (1), 211–215, 1993.

[122] H. P. Breuer, W. Huber, and F. Petruccione, *Fluctuation Effects on Wave Propagation in a Reaction-Diffusion Process*, Physica D **73**, 259–273, 1994.

[123] J. Armero, J. M. Sancho, J. Casademunt, A. M. Lacasta, L. Ramírez-Piscina, and F. Sagués, *External Fluctuations in Front Propagtion*, Phys. Rev. Lett. **76**, 3045–3048, 1996.

[124] J. Zhang, Y.-C. Zhang, P. Alstrøm, and M. T. Levinsen, *Modeling Forest Fire by a Paper-Burning Experiment, a Realization of the Interface Growth Mechanism*, Physica A **189**, 383–389, 1992.

[125] L. A. N. Amaral, A.-L. Barabasi, and H. E. Stanley, *Universality Classes for Interface Growth with Quenched Disorder*, Phys. Rev. Lett. **73** (1), 62–65, 1994.

[126] F. Family and T. Vicsek (eds.), *Dyanmics of Fractal Surfaces*, World Scientific, Singapore, 1991.

[127] A.-L. and H. E. Stanley, *Fractal Concepts in Surface Growth*, Cambridge University Press, Cambridge, England, 1995.

[128] T. Natterman, S. Stepanow, L.-H. Tang, and H. Leschhorn, *Dynamics of Interface Depinning in a Disordered Medium*, J. Phys. (Paris) II **2**, 1483–, 1992.

[129] S. F. Edwards and D. R. Wilkinson, *The Surface Statistics of a Granular Aggregate*, Proc. R. Soc. London A **381**, 17–31, 1982.

[130] I. Sendiña-Nadal, A. P. Muñuzuri, D. Vives, V. Pérez-Villar, J. Casademunt, L. Ramírez-Piscina, J. M. Sancho, and F. Sagués, *Wave Propagation in a Medium with Disordered Excitability*, Phys. Rev. Lett. **80** (24), 5437–5440, 1998.

[131] I. Sendiña-Nadal, V. Pérez-Muñuzuri, M. Gómez-Gesteira, A. P. Muñuzuri, V. Pérez-Villar, D. Vives, F. Sagués, J. Casademunt, J. M. Sancho, and L. Ramírez-Piscina, *Effects of a Quenched Disorder on Wave Propagation in Excitable Media*, Int. J. of Bif. and Chaos **9** (2), 2353–2361, 1999.

[132] D. Stauffer and A. Aharony, *Introduction to Percolation Theory*, Taylor & Francis, London, 1994.

[133] M. Sahami, *Applications of Percolation Theory*, Taylor & Francis, London, 1994.

[134] T. P. Eggarter and M. H. Cohen, *Simple Model for Density of States and Mobility of an Electron in a Gas of Hard-Core Scatterers*, Phys. Rev. Lett. **25** (12), 807–810, 1970.

[135] B. J. Last and D. J. Thouless, *Percolation Theory and Electrical Conductivity*, Phys. Rev. Lett. **27** (25), 1719–1721, 1971.

[136] L. B. Kiss, P. Svedlindh, L. Lundgren, J. Hudner, H. Ohlsén, and L. Stolt, *Spontaneous Conductivity Fluctuations in Y-Ba-Cu-O Thin Films: Scaling of Fluctuations, Experimental Evidence of Percolation at the Superconducting Transition*, Solid State Commun **75** (9), 747–751, 1990.

[137] P. Jensen, P. Melinon, A. Hoareau, J. X. Hu, B. Cabaud, M. Treilleux, E. Bernstein, and D. Guillot, *Experimental Achievement of 2D Percolation and Cluster-Cluster Aggregation Models by Cluster Deposition*, Physica A **185**, 104–110, 1992.

[138] U. Oxaal, M. Murat, F. Boger, A. Aharony, J. Feder, and T. Jøssang, *Viscous Fingering on Percolation Clusters*, Nature **329**, 32–37, 1987.

[139] I. Sendiña-Nadal, D. Roncaglia, D. Vives, V. Pérez-Muñuzuri, M. Gómez-Gesteira, V. Pérez-Villar, J.Echave, J. Casademunt,

L. Ramírez-Piscina, and F. Sagués, *Percolation Thresholds in Chemical Disordered Excitable Media*, Phys. Rev. E **58** (2), R1183–R1186, 1998.

[140] I. Schebesch and H. Engel, *Wave Propagation in Heterogeneous Excitable Media*, Phys. Rev. E **57** (4), 3905–3910, 1998.

[141] J. P. Keener, *A Geometrical Theory for Spiral Waves in Excitable Media*, SIAM J. Appl. Math. **46** (6), 1039–1056, 1986.

[142] P. K. Brazhnik and J. J. Tyson, *Velocity-Curvature Dependence for Chemical Waves in the Belousov-Zhabotinsky Reaction: Theoretical Explanation of Experimental Observations*, Phys. Rev. E **59** (4), 3920–3925, 1999.

[143] A. M. Pertsov, M. Wellner, and J. Jalife, *Eikonal Relation in Highly Dispersive Excitable Media*, Phys. Rev. Lett. **78** (13), 2656–2659, 1997.

[144] M. Wellner and A. M. Pertsov, *Generalized Eikonal Equation in Excitable Media*, Phys. Rev. E **55** (6), 7656–7660, 1997.

[145] V. Petrov, Q. Ouyang, G. Li, and H. L. Swinney, *Light-Induced Frecuency Shift in Chemical Spirals*, J. Phys. Chem. **100** (49), 18992–18996, 1996.

[146] K. Wiesenfeld and F. Moss, *Stochastic Resonance and the Benefits of Noise: from Ice Ages to Crayfish and Squids*, Nature **373**, 33–36, 1995.

[147] F. Moss, D. Pierson, and D. O'Gorman, *Stochastic Resonance: Tutorial and Update*, Int. J. of Bif. and Chaos **4** (6), 1383–1397, 1994.

[148] L. Gammaitoni, P. Hänggi, P. Jung, and F. Marchesoni, *Stochastic Resonance*, Rev. Mod. Phys. **70**, 223–288, 1998.

[149] I. Sendiña-Nadal and V. Pérez-Muñuzuri, *Noise-Enhanced Wave Train Propagation in Unexcitable Media*, Int. J. of Bif. and Chaos **In press**, 2001.

[150] R. Perazzo, L. Romanelli, and R. Deza, *Fault Tolerance in Noise-Enhanced Propagation*, Phys. Rev. E **61** (4), R3287–R3290, 2000.

[151] J. García-Ojalvo, A. M. Lacasta, F. Sagués, and J. M. Sancho, *Noise-Sustained Signal Propagation*, Europhys. Lett. **50**, 427–433, 2000.

[152] A. M. Pertsov, J. M. Davidenko, R. Salomonz, W. Baxter, and J. Jalife, *Spiral Waves of Excitation Underlie Reentrant Activity in Isolated Cardiac Muscle*, Circ. Res. **72**, 631–650, 1993.

[153] I. Aranson, H. Levine, and L. Tsimring, *Spiral Competition in Three-Component Excitable Media*, Phys. Rev. Lett. **76** (7), 1170–1173, 1996.

[154] S. K. Scott, J. Wang, and K. Showalter, *Modelling Studies of Spiral Waves and Target Patterns in Premixed Flames*, J. Chem. Soc. Faraday Trans. **93** (9), 1733–1739, 1997.

[155] Y. Kuramoto, *Chemical Oscillations, Waves and Turbulence*, Springer, 1984.

[156] A. T. Winfree, *Varieties of Spiral Wave Behaviour: An Experimentalist's Approach to the Theory of Excitable Media*, Chaos **1** (3), 303–334, 1991.

[157] A. S. Mikhailov, V. A. Davydov, and V. S. Zykov, *Complex Dynamics of Spiral Waves and Motion of Curves*, Physica D **70**, 1–39, 1994.

[158] E. Meron and P. Pelcé, *Model for Spiral Wave Formation in Excitable Media*, Phys. Rev. Lett. **60** (18), 1880–1883, 1988.

[159] D. Barkley, *Euclidean Symmetry and the Dynamics of Rotating Spiral Waves*, Phys. Rev. Lett. **72** (1), 164–167, 1994.

[160] O. Steinbock, P. Kettunen, and K. Showalter, *Anysotropy and Spiral Organizing Centers in Patterned Excitable Media*, Science **269**, 1857–1859, 1995.

[161] M. Braune and H. Engel, *Compound Rotation of Spiral Waves in Active Media with Periodically Modulated Excitability*, Chem. Phys. Lett. **211** (6), 534–540, 1993.

[162] O. Steinbock, J. Schütze, and S. C. Müller, *Electric-Field-Induced Drift and Deformation of Spiral Waves in an Excitable Medium*, Phys. Rev. Lett. **68** (2), 248–251, 1992.

[163] K. I. Agladze and P. De Kepper, *Influence of Electric Field on Rotating Spiral Waves in the Belousov-Zhabotinsky Reaction*, J. Phys. Chem. **96** (13), 5239–5242, 1992.

[164] A. P. Muñuzuri, M. Gómez-Gesteira, V. Pérez-Muñuzuri, V. I. Krinsky, and V. Pérez-Villar, *Mechanism of the Electric-Field-Induced Vortex Drift in Excitable Media*, Phys. Rev. E **48** (5), R3232–R3235, 1993.

[165] M. Ruiz-Villareal, M. Gómez-Gesteira, and V. Pérez-Villar, *Drift of Interacting Asymmetrical Spiral Waves*, Phys. Rev. Lett. **78** (5), 779–782, 1997.

[166] M. Ruiz-Villareal, M. Gómez-Gesteira, C. Souto, A. P. Muñuzuri, and V. Pérez-Villar, *Long-Term Vortex Interaction in Active Media*, Phys. Rev. E **54** (3), 2999–3002, 1996.

[167] A. P. Muñuzuri, V. Pérez-Muñuzuri, and V. Pérez-Villar, *Attraction and Repulsion of Spiral Waves by Localized Inhomogeneities in Excitable Media*, Phys. Rev. E **58** (3), R2689–R2692, 1998.

[168] X. Zou and H. Levine, *Interaction between a Drifting Spiral and Defects*, Phys. Rev. E **47** (2), R800–R803, 1993.

[169] J. García-Ojalvo and L. Schimansky-Geier, *Noise-Induced Spiral Dynamics in Excitable Media*, Europhys. Lett. **47**, 298–303, 1999.

[170] I. S. Aranson, H. Chaté, and L.-H. Tang, *Spiral Motion in a Noisy Complex Ginzburg-Landau Equation*, Phys. Rev. Lett. **80** (12), 2646–2649, 1998.

[171] W. Jahnke and A. T. Winfree, *A Survey of Spiral-Wave Behaviors in the Oregonator Model*, Int. J. of Bif. and Chaos **1** (2), 445–466, 1991.

[172] S. C. Müller and V. Zykov, *Simple and Complex Spiral Wave Dynamics*, Phil. Trans. R. Soc. Lond. A **347**, 677–685, 1994.

[173] S. Alonso and F. Sagués, *Noise-Induced Brownian Motion of Spiral Waves*, Phys. Rev. E **63** (4), 046205, (12 pag), 2001.

[174] J. Ross, S. C. Müller, and C. Vidal, *Chemical Waves*, Science **240**, 460–465, 1988.

[175] H. L. Swinney and V. I. Krinsky (eds.), *Waves and Patterns in Chemical and Biological Media*, 1 & 2, vol. 49, Physica D, 1991.

[176] A. V. Panfilov and A. V. Holden, *Computational Biology of the Heart*, John Wiley & Sons, Chichester, 1997.

[177] Y. Braiman, J. F. Lindner, and W. L. Ditto, *Taming Spatiotemporal Chaos with Disorder*, Nature **378**, 465–467, 1995.

[178] C. Kurrer and K. Shulten, *Noise-Induced Synchronous Neuronal Oscillations*, Phys. Rev. E **51** (6), 6213–6218, 1995.

[179] P. Jung, *Thermal Waves, Criticality, and Self-Organization in Excitable Media*, Phys. Rev. Lett. **78** (9), 1723–1726, 1997.

[180] S. K. Han, T. G. Yim, D. E. Postnov, and O. V. Sosnovtseva, *Interacting Coherence Resonance Oscillators*, Phys. Rev. Lett. **83** (9), 1771–1774, 1999.

[181] A. Neiman, L. Schimansky-Geier, A. Cornell-Bell, and F. Moss, *Noise-Enhanced Phase Synchronization in Excitable Media*, Phys. Rev. Lett. **83** (23), 4896–4899, 1999.

[182] S. Alonso, I. Sendiña-Nadal, V. Pérez-Muñuzuri, J. M. Sancho, and F. Sagués, *Regular Wave Propagation Out of Noise in Chemical Active Media*, Phys. Rev. Lett., 2001.

[183] A. S. Mikhailov, *Selected Topics in Fluctuational Kinetics of Reactions*, Phys. Rep. **184**, 307–374, 1989.

[184] M. A. Santos and J. M. Sancho, *Fronts Dynamics in the Presence of Spatio-Temporal Structured Noises*, Phys. Rev. E, Accepted in April 2001.

[185] J. Tyson and P. Keener, *Singular Perturbation Theory of Traveling Waves in Excitable Media*, Physica D **32**, 327–361, 1988.

[186] A. S. Mikhailov and V. S. Zykov, *Kinematical Theory of Spiral Waves in Excitable Media: Comparison with Numerical Simulations*, Physica D **52**, 379–397, 1991.

List of Publications

This thesis gave rise to the following related publications:

I. I. Sendiña-Nadal, M. Gómez-Gesteira, V. Pérez-Muñuzuri, V. Pérez-Villar, J. Armero, L. Ramírez-Piscina, J. Casademunt, F. Sagués, and J. M. Sancho, *"Wave Competition in Excitable Modulated Media"* Phys. Rev. E **56**, 6298 (1997).

II. I. Sendiña-Nadal, A. P. Pérez-Muñuzuri, D. Vives, V. Pérez-Muñuzuri, J. Casademunt, L. Ramírez-Piscina, J.M. Sancho, and F. Sagués, *"Wave propagation in a medium with disordered excitability"*, Phys. Rev. Lett. **80**, 5437 (1998).

III. I. Sendiña-Nadal, D. Roncaglia, D. Vives, D. Vives, V. Pérez-Muñuzuri, M. Gómez-Gesteira, V. Pérez-Villar, J. Echave, J. Casademunt, L. Ramírez-Piscina, and F. Sagués, *"Percolation thresholds in chemical disordered excitable media"*, Phys. Rev. E. **58**, R1183 (1998).

IV. I. Sendiña-Nadal, V. Pérez-Muñuzuri, M. Gómez-Gesteira, A. P. Muñuzuri, V. Pérez-Villar, D. Vives, F. Sagués, J. Casademunt, J. M. Sancho, and L. Ramírez-Piscina, *"Effects of a quenched disorder on wave propagation in excitable media"*, Int. J. of Bif. and Chaos **9**, 2353 (1999).

V. I. Sendiña-Nadal, S. Alonso, V. Pérez-Muñuzuri, M. Gómez-Gesteira, V. Pérez-Villar, L. Ramírez-Piscina, J. Casademunt, J.M. Sancho, and F. Sagués, *"Brownian motion of spiral waves driven by spatiotemporal structured noise"*, Phys. Rev. Lett. **84**, 2734 (2000).

VI. I. Sendiña-Nadal and V. Pérez-Muñuzuri, *"Noise-enhanced wave train propagation in unexcitable media"*, Int. J. of Bif. and Chaos, (2001) in press.

VII. I. Sendiña-Nadal, E. Mihaliuk, J. Wang, V. Pérez-Muñuzuri, and K. Showalter, *"Wave propagation in subexcitable media with periodically modulated excitability"*, Phys. Rev. Lett. **86**, 1646 (2001).

VIII. I. Sendiña-Nadal, V. Pérez-Muñuzuri, V. Eguíluz, E. Hernández-García, and O. Piro, *"Quasiperiodic patterns in boundary-modulated excitable waves"*, Phys. Rev. E (2001), in press.

IX. S. Alonso, I. Sendiña-Nadal, V. Pérez-Muñuzuri, J. M. Sancho, and F. Sagués, *"Regular wave propagation out of noise in chemical active media"*, Phys. Rev. Lett., (2001) in press.

Index